Computational fluid dynamics modeling of hemodynamics in the Circle of Willis during vasospasm and in the left ventricle in the presence of a left ventricular assist device

Angela Straccia

A dissertation submitted in partial fulfillment of the
requirements for the degree of

Doctor of Philosophy

University of Washington

2024

Reading Committee:

Alberto Aliseda, Chair

James Riley

Juan Carlos del Alamo

Program Authorized to Offer Degree:
Department of Mechanical Engineering

University of Washington

Abstract

Computational fluid dynamics modeling of hemodynamics in the Circle of Willis during vasospasm and in the left ventricle in the presence of a left ventricular assist device

Angela Straccia

Chair of the Supervisory Committee:
Alberto Aliseda
Mechanical Engineering

Computational fluid dynamics (CFD) simulations can be leveraged to understand clinically relevant problems in cardiovascular flows. This dissertation explores two applications of CFD modeling to physiological flows: intracranial flow in the Circle of Willis (CoW) during vasospasm and intraventricular flow in the presence of a left ventricular assist device (LVAD).

The CoW is a redundant network of blood vessels that perfuses the cerebral tissue. Flow in the collateral pathways that form this ring-like vascular structure can change in the presence of vessel constriction or occlusion. After a bleeding event in the subarachnoid space, vessels in the CoW sometimes involuntarily constrict, in a phenomenon known as vasospasm, which limits blood flow to the tissue, potentially causing infarct. The role of collateral pathways in the response to vasospasm is not well-understood. This dissertation investigates the relationship between changes in flow rate and direction in the collateral pathways, the anatomical variant of the CoW, and localization and severity of vasospasm across the network. Patient-specific CFD simulations were created in a cohort of 25 vasospasm patients, leveraging computed tomographic angiography (CTA) scans to generate models of the vasculature and transcranial Doppler ultrasound (TCD) measurements to apply boundary conditions.

Bayesian analysis accounted for parameter uncertainty introduced by the medical data and was used to optimize the model parameters applied in the final simulation. Diameters, velocities, and flow rates were benchmarked against literature values, and virtual angiography performed by tracking a passive scalar, advected by the fluid velocity computed in the CFD simulations, was compared to clinical angiography, showing good agreement. Two metrics for vasospasm severity – percent changes in resistance and viscous dissipation – correlated closely with angiographic severity and helped identify regions of localization of vasospasm within the CoW and quantify overall severity.

The second application of CFD in this thesis is on intraventricular flows. LVADs are centrifugal pumps implanted in the left ventricle (LV) of advanced heart failure patients. While pump designs have improved significantly over time, the risk of thromboembolic events remains high. Third generation pumps incorporate a pulsatility mode that modulates the rotational speed of the device impeller to promote in-pump washout. The role that this pulsatility mode plays in intraventricular washout is an active area of research. This dissertation studied how the temporal synchronization of the pulsatility mode with the native cardiac cycle affects the degree of intraventricular washout, which can have important implications for platelet activation and aggregation that subsequently can lead to thrombus formation. Lagrangian particle tracking was integrated into CFD simulations to model the hemodynamic environment experienced by platelets moving through the LV. Boundary conditions were defined using the time-varying flow rate from an equivalent particle image velocimetry (PIV) experiment. Regions of stasis were identified from examining velocity fields and calculating the stagnation index, which is an Eulerian quantification of stasis. Eulerian metrics from the CFD simulations agreed closely with PIV results. The optimal timing of the pulsatility mode with the cardiac cycle that maximizes intraventricular washout was

identified.

TABLE OF CONTENTS

Page

List of Figures iii

Chapter 1: Introduction 1
1.1 Contributions in this Thesis 1
1.2 Characteristics of Cardiovascular Flows 2
1.3 Computational Fluid Dynamics Modeling Approach 3
1.4 Computational Modeling of Cardiovascular Fluid Mechanics 6

Chapter 2: Activation of Collateral Pathways in the Circle of Willis during Vasospasm 9
2.1 Introduction and Background 9
2.2 Methodology 28
2.3 Results 58
2.4 Discussion 103
2.5 Conclusions 109
2.6 Future Work 110

Chapter 3: Platelet Activation in the Left Ventricle in the Presence of a Left Ventricular Assist Device with Speed Modulation Synchronized with the Cardiac Cycle 112
3.1 Introduction and Background 112
3.2 Methodology 118
3.3 Results 125
3.4 Discussion 135
3.5 Conclusions 142
3.6 Future Work 143

Chapter 4: Conclusions of the Dissertation 144

Bibliography 147

LIST OF FIGURES

Figure Number		Page
2.1	Anatomy of the Circle of Willis	10
2.2	Structure of the arterial wall	12
2.3	Subarachnoid space surrounding the artery	13
2.4	Ruptured aneurysm introducing blood to the subarachnoid space leading to vasospasm	14
2.5	Transcranial Doppler ultrasound (TCD) transducer insonating a cerebral artery	15
2.6	Velocities returned by the TCD transducer for flow towards the transducer (top) and away from the transducer (bottom)	16
2.7	Computed tomographic angiography (CTA) of the brain	18
2.8	Digital subtraction angiography (DSA) for an internal carotid artery (ICA) injection in the anterior-posterior view (a) and lateral view (b) and a vertebral artery injection in the anterior-posterior view (c) and lateral view (d)	20
2.9	Direction of antegrade flow in the collateral pathways of the Circle of Willis	21
2.10	Three-dimensional reconstruction of the Circle of Willis in Radiant	32
2.11	Transcranial Doppler ultrasound measurement of velocities in the left middle cerebral artery (top) converted to a tile with higher contrast between the measurement and the background used by the automated tracing algorithm (bottom)	34
2.12	A two-dimensional illustration of the prior, likelihood and posterior for the Bayesian analysis	37
2.13	Case 1 prior norm versus secondary norm for the entire set of hyperparameters (top) and for a subset of hyperparameters on axes with equal limits (bottom), with the red data point representing the final hyperparameter selected for the study	40

2.14 Case 1 secondary flow rate after the Bayesian analysis versus the hyperparameter, with the dashed line representing the target flow rate and the red datapoint representing the final hyperparameter selected for this study 41
2.15 Case 2 prior norm versus secondary norm for the entire set of hyperparameters (top) and for a subset of hyperparameters on axes with equal limits (bottom), with the red data point representing the final hyperparameter selected for the study 43
2.16 Case 2 secondary flow rate after the Bayesian analysis versus the hyperparameter, with the dashed line representing the target flow rate and the red datapoint representing the final hyperparameter selected for this study 44
2.17 Centerline velocities over time in the bilateral anterior, middle, posterior, and internal carotid arteries and basilar artery 45
2.18 Pressure slices through a right middle cerebral artery for calculating resistance 50
2.19 Vessel zones used for integrating viscous dissipation in the left-right view (left) and anterior-posterior view (right) 54
2.20 Least squares error between the quantized CFD metrics and angiographic severity given a range of thresholds for resistance (left) and dissipation (right) 56
2.21 Summary of methodology for creating patient-specific CFD simulations in the Circle of Willis during vasospasm 59
2.22 Patient A with a complete circle of Willis with labels of the major cerebral blood vessels (left) and patient B with a missing right PCA P1 segment with labels of the collateral pathways (right) 60
2.23 Patient A collateral flow directions during the baseline (top) and vasospasm (bottom) conditions exhibited with arrows, the primary recruited inlet artery exhibited with large double arrows, and the locations and severity of vasospasm exhibited with valve icons 62
2.24 Patient B collateral flow directions during the baseline (top) and vasospasm (bottom) conditions exhibited with arrows, the primary recruited inlet artery exhibited with large double arrows, and the locations and severity of vasospasm exhibited with valve icons 63
2.25 Patient A vessel diameters, velocities, and flow rates at baseline (dotted black line with black point) and vasospasm (solid black line with black point) overlayed on literature values (shaded Gaussian distributions) . 64

2.26 Patient B vessel diameters, velocities, and flow rates at baseline (dotted black line with black point) and vasospasm (solid black line with black point) overlayed on literature values (shaded Gaussian distributions) . 66

2.27 Patient A clinical (left) and virtual (right) angiograms for baseline (top) and vasospasm (bottom) 69

2.28 Patient B clinical (left) and virtual (right) angiograms for baseline (top) and vasospasm (bottom) 70

2.29 Violin plot for the sensitivity analysis that solves a linear system of equations for different parameter sets for patient A (top) and patient B (bottom) during the baseline (light shade) and vasospasm (dark shade) conditions 72

2.30 Boxplots of percent changes in resistance (top) and dissipation (bottom) associated with each angiographic severity 74

2.31 Bar charts of the percent of vessels in ranges of resistance (top) and dissipation (bottom) metrics with an associated angiographic severity 75

2.32 Percent of vessels across the cohort that agree with the angiographic severity based on the resistance (black) and dissipation (grey) metrics 76

2.33 Patients 1 and 2 with vasospasm localized in one zone of the CoW with the angiographic severity (top), percent change in resistance (middle) and percent change in dissipation (bottom) in each vessel 80

2.34 Patients 3 and 4 with vasospasm localized in two zones of the CoW with the angiographic severity (top), percent change in resistance (middle) and percent change in dissipation (bottom) in each vessel 82

2.35 Patients 5 and 6 with vasospasm balanced across zones in the CoW with the angiographic severity (top), percent change in resistance (middle) and percent change in dissipation (bottom) in each vessel 84

2.36 Patients 7 and 8 with infarct caused by vasospasm (black circles) with the angiographic severity (top), percent change in resistance (middle) and percent change in dissipation (bottom) in each vessel 86

2.37 Patients 9 and 10 with vasospasm localized in one zone of the CoW with the angiographic severity (top), percent change in resistance (middle) and percent change in dissipation (bottom) in each vessel 89

2.38 Patients 11 and 12 with vasospasm localized in one zone of the CoW with the angiographic severity (top), percent change in resistance (middle) and percent change in dissipation (bottom) in each vessel 91

2.39 Patient 13 with vasospasm localized in two zones of the CoW with the angiographic severity (top), percent change in resistance (middle) and percent change in dissipation (bottom) in each vessel 92

2.40 Patients 14 and 15 with vasospasm localized in two zones of the CoW with the angiographic severity (top), percent change in resistance (middle) and percent change in dissipation (bottom) in each vessel 94

2.41 Patients 16 and 17 with vasospasm localized in two zones of the CoW with the angiographic severity (top), percent change in resistance (middle) and percent change in dissipation (bottom) in each vessel 95

2.42 Patients 18 and 19 with vasospasm balanced across zones in the CoW with the angiographic severity (top), percent change in resistance (middle) and percent change in dissipation (bottom) in each vessel 97

2.43 Patient 20 with vasospasm balanced across zones in the CoW with the angiographic severity (top), percent change in resistance (middle) and percent change in dissipation (bottom) in each vessel 98

2.44 Patients 21 and 22 with vasospasm balanced across zones in the CoW with the angiographic severity (top), percent change in resistance (middle) and percent change in dissipation (bottom) in each vessel 100

2.45 Patient 23 with mild vasospasm in the CoW with the angiographic severity (top), percent change in resistance (middle) and percent change in dissipation (bottom) in each vessel 101

2.46 Patients 24 and 25 with mild vasospasm in the CoW with the angiographic severity (top), percent change in resistance (middle) and percent change in dissipation (bottom) in each vessel 102

3.1 Left ventricle with a left ventricular assist device (LVAD) implanted . 114

3.2 Head (mmHg) versus flow rate (L/min) curve for the HeartMate 3 at different rotational speeds (RPM) 115

3.3 Computational domain for a patient-specific ventricle implanted with an inflow cannula with the mitral valve as the inlet and inflow cannula as the outlet in the left-right view (left) and posterior-anterior view (right) 119

3.4 The HeartMate 3 pulsatility mode (a) modulates the pump speed every 2 seconds and is synchronized with the cardiac cycle at peak diastole, peak systole, systole, or diastole (b) resulting in different flow rate profiles over time 121

3.5 Velocity magnitude and in-plane direction for PIV experiments and CFD model at two different times for the speed modulation synchronized with systole. (a) Left-right view (b) Posterior-anterior view . . 126
3.6 Comparison of velocity magnitude for speed modulation synchronized with systole within a rectangular subzone in the posterior-anterior view (a) at peak diastole (b) at peak systole (c) at low RPM and (d) at high RPM in the pulsatility mode 127
3.7 Comparison of velocity magnitude for speed modulation synchronized with systole within a rectangular subzone in the left-right view (a) at peak diastole (b) at peak systole (c) at low RPM and (d) at high RPM in the pulsatility mode 129
3.8 Bland-Altman plots of differences in CFD and PIV velocity magnitude for speed modulation synchronized with systole in the posterior-anterior and left-right views (a) at peak diastole (b) at peak systole (c) at low RPM and (d) at high RPM in the pulsatility mode with the median (labeled in bold face) and 95% confidence intervals (labeled with italics) identified with dashed lines 130
3.9 Stagnation index for the PIV experiment and CFD model in the posterior-anterior and left-right views for speed modulation synchronized with systole 131
3.10 Virtual contrast injected in the CFD model for speed modulation synchronized at systole for 8 seconds followed by a period of washout. (a) 0.6 sec (b) 7.9 sec (c) 10.6 sec (d) 16 sec (e) 21.1 sec. (f) Spherical regions of interest (g) Virtual contrast over time in the LVOT, apex, and near wall region 133
3.11 Virtual contrast integrated over the entire left ventricle versus time (left) and the fraction of particles remaining in the left ventricle versus time (right) for four temporal synchronizations with the corresponding exponential decay time t_d 134
3.12 Representative particle trajectories for platelets that exceed 35 seconds of residence time in the (a) left-right view (b) posterior-anterior view. (c) Distributions of particle shear stress history, (d) residence time, and (e) time-averaged shear stress for speed modulation at peak systole and at systole 136

ACKNOWLEDGMENTS

I would like to express my deepest appreciation for Dr. Alberto Aliseda, who has been an incredibly supportive and patient advisor. Thank you for your mentorship in the technical and social aspects of this journey as well as for creating a positive culture in the lab. I will miss our annual lab camping trip and spirited conversations at the Duchess.

Thank you to the incredible clinical collaborators that made this research possible and enthusiastically answered all my questions: Drs. Michael R. Levitt, David Bass, Guilherme Barros, Florence Sheehan, Deepak Sharma, Daniel Leotta, Claudius Mahr, and Jennifer Beckman. I appreciate my committee members Drs. Jim Riley and Juan Carlos del Alamo for their guidance throughout the PhD.

My family has been my biggest champion throughout this journey. To my Mom, who loves me wholeheartedly, helped me develop the resilience to make it through tough moments, and celebrated the successes on the other side. To my brother Joseph, who always inspired me to be excited about science and gave his unwavering support. To my brother Mark, who invited me on adventures and believed in me. To my sisters-in-law Andrea and Monica, who encouraged me to pursue my career ambitions and modeled what it looks like to be a female leader. To the Townes family, who always welcomed me with open arms into their home and made me feel valued.

I could not have made it through this program without the amazing support from my community. To Ian Good, for believing in me and showing me unconditional love. To Fanette Chassagne, for reminding me that two steps forward and one step back is still progress and for making me feel like being a successful woman engineering

is possible. To Mike Barbour, for all of your support making it past the finish line and for helping me keep the challenges in perspective. To Julia Romero Bhathal, for being an incredible friend and fellow adventurer. To Laurel Miller Marsh, for always bringing a fun and positive light to our lab. To Maria Yang, for our many coffee dates and for your encouragement to keep going. To Amelie Ferran, for your cheeky jokes and for starting goals group to help us stay connected through COVID. To Erin Espeland, for always showing up and bringing brightness. To Sari Barzcay, for feeding my soul with a late night charcuterie and chat. To Kee Onn Fong, for listening and for showing me the world of Magnuson badminton. To Melody Mojib, for caring about DEI and for making me feel less alone in the dark tunnel. To Ava Obenaus, for making me laugh at many an entertaining story and for your commitment to watching the Bachelor. To Elijah Kuska, Sam Hoang, Lynda Brady, and Marissa Miramontes, for all the fun we had with the Mechanical Engineering Graduate Student Association. To Abbie Shew, Abby Alridge, Alan Kaptanoglu, and Bridge Condron, for showing me that all it takes to get through a PhD is chili and cinnamon rolls and a big hug. To Anda Vladoiu, Ryan McGinty, and Abhi Dasari, for letting me vent over post-climbing beers. To Farzanah Ausaluth, for always taking my call with a warm heart. To Meghann Gerber, Wendy Lendrum, Anne Swenson, and Lisa Gray, for believing I deserve to feel by best.

DEDICATION

To my family. You are everything.

Chapter 1

INTRODUCTION

1.1 Contributions in this Thesis

Computational fluid dynamics (CFD) simulations offer unique insights into three-dimensional flow fields across a wide variety of engineering applications. While CFD has been applied extensively to aerodynamics and other industrial applications, cardiovascular flows can also be described by the fundamental equations of fluid dynamics, and thus can benefit from the use of CFD. As the availability of computational power rapidly increased in the last 50 years, CFD has become more accessible and is reaching turn-around times that allow for clinical uses of this analysis methods to support diagnosis and treatment planning.

Two distinct studies of CFD applied to cardiovascular applications are explored in this thesis, with some computational methodologies shared across the applications.

Chapter 2 describes the study of flow in the Circle of Willis (CoW), the redundant network of blood vessels that perfuses the brain, during vasospasm, an involuntary constriction of blood vessels after a bleeding event in the brain. Flow in the collateral pathways that form the ring-like structure of the CoW are known to change in patients with vessel occlusion, but changes in the CoW during vasospasm are not well-documented. A novel methodology that incorporates patient-specific data to create a realistic CFD model was developed and applied to a cohort of 25 patients. The study investigated the relationship between the anatomical variant of the CoW, the locations and severities of vasospasm, and changes in flow in the collateral pathways.

Chapter 3 describes intraventricular flow in a patient with a left ventricular assist device (LVAD), a centrifugal pump implanted in advanced heart failure patients.

LVADs are increasingly used as a bridge-to-transplantation or destination therapy, but the risk of stroke remains high. Third generation pumps incorporate a pulsatility mode to improve in-pump washout. The effects of synchronizing the pulsatility mode of the pump with the native cardiac cycle remains an open question. This study explored how the altered hemodynamics environment in the presence of an LVAD influenced factors that lead to platelet activation, comparing four different timings of the pulsatility mode with the cardiac cycle to determine an optimal timing. Results from an equivalent particle image velocimetry (PIV) experiment were leveraged to create boundary conditions and benchmark the CFD results.

1.2 Characteristics of Cardiovascular Flows

Due to the pumping of the heart, intraventricular and arterial flows are inherently time-dependent. John Womersley developed an expression for the velocity in a straight circular pipe as a function of time based on laminar, axisymmetric flow with a periodic pressure gradient [169]. The Womersley number characterizes the pulsatility of the flow with the ratio of the transient inertial force and the viscous forces, calculated with:

$$Wo = L\sqrt{\frac{\omega}{\nu}} \tag{1.1}$$

where L is the characteristic length scale, ω is the angular frequency, and ν is the kinematic viscosity. The higher the Womersley number, the larger the role transient forces play, resulting in a flatter velocity profile as compared to low numbers that result in an almost parabolic profile. Typical values of the Womersley number are 15 in the left ventricle and 3 in the femoral artery [157].

The flow regime of the hemodynamics can be determined by calculating the Reynolds number, which is the ratio of the inertial to viscous forces, calculated with:

$$Re = \frac{\rho V D}{\mu} \tag{1.2}$$

where ρ is the density, V is the characteristic velocity, D is the characteristic length scale, and μ is the dynamic viscosity.

For internal steady flows, transition to turbulence begins at about 2300. The Reynolds number is dependent on the location in the body, resulting in different flow behavior. Transitional flows are typically observed in the heart and aorta, but flow can become fully turbulent in the presence of a stenotic or artificial heart valve [157].

Blood is composed of plasma, red blood cells, white blood cells, and platelets, and thus can be considered a suspension. At the macroscopic level in the heart and large arteries, blood can be considered a homogeneous medium. Blood is a non-Newtonian fluid, where higher shear rates decrease the viscosity of the blood. In many vessels, the shear rates are consistently high, above the threshold for which blood functionally behaves like a Newtonian fluid [157].

Due to changes in arterial pressure, blood vessel walls will expand and contract passively. The distensibility of the aorta is much higher than that of the downstream vasculature [157], resulting in larger displacements of the vessel wall in the aorta than in smaller arteries like those supplying the cerebral tissue.

1.3 Computational Fluid Dynamics Modeling Approach

When approaching the building of a computational model, the first step is to identify the purpose of the study. In the case of cardiovascular applications, close collaborations with clinicians can help pinpoint the most clinically relevant questions. This thesis benefitted significantly from collaborations with the University of Washington Department of Neurological Surgery, and Divisions of Anesthesiology and Cardiology (Department of Medicine) in the study of vasospasm in the cerebral vasculature discussed in Chapter 2 and University of Washington Division of Cardiology in the study of flow in the left ventricle in the presence of an LVAD discussed in Chapter 3.

The next step is to create the computational domain where the Navier-Stokes equations will be solved with CFD. For cardiovascular applications, the gold standard is to derive the geometry from patient-specific medical imaging data. In the study of vasospasm, computed tomographic angiography (CTA) scans were used to create patient-specific models of the vasculature. In the LVAD study, the model of the left ventricle was derived from magnetic resonance imaging (MRI). In order to solve the fluid dynamics numerically, the flow computational domain must be discretized via mesh generation. The mesh should accurately resolve areas with large gradients in the flow like near the wall. The mesh should be fine enough to properly capture the physical behavior while also balancing the computational expense. A mesh independence study should be performed to ensure that the problem is properly resolved while avoiding unnecessary expense. The mesh resolution is systematically varied and CFD metrics of interest are computed for the different mesh resolutions and compared among the different meshes. The final mesh is selected based on the agreement of the CFD metrics with those of the finest mesh, within a certain tolerance.

The appropriate physics must be incorporated into the model. The physical models chosen for an application should balance complexity and accuracy with computational expense. While blood is technically a suspension of red blood cells, white blood cells, and platelets in plasma, blood can be modeled as an incompressible, homogeneous fluid at the scales of interest in the major cerebral blood vessels and the left ventricle. Blood is modeled as a Newtonian fluid, the assumptions for which are discussed in more detail in the ensuing chapters. The flow regime can be estimated by calculating the Reynolds number, and the appropriate modeling techniques should match the presence of laminar, transitional, or turbulent flow. In addition to modeling fluid dynamics, incorporating a passive scalar in the model using an advection-diffusion equation [29, 128, 131] can allow the CFD model to be benchmarked against clinical angiography, as discussed in sections 2.2.11 and 2.3.3 in the study of cerebral vasospasm, and to identify regions of stasis, as discussed in sections

3.2.6 and 3.3.3 in the study of intraventricular flows in the presence of an LVAD. Lagrangian particle tracking can be leveraged to account for the hemodynamics microenvironment of platelets in a left ventricular flow, described in sections 3.2.8 and 3.3.5.

Boundary conditions must be prescribed at the inlets and outlets of the model, which are often prescribed with values of pressure, velocity profile, or flow rate. In studying cerebral vasospasm, sections 2.2.4 and 2.2.9 will discuss how patient-specific measurements of flow velocities from transcranial Doppler ultrasound (TCD) can be incorporated to define the boundary conditions of the model. In studying intraventricular flow in the presence of an LVAD, section 3.2.3 will demonstrate how experimental flow rates can be used to define the flow rate waveform boundary condition at the outlet.

Solving the Navier-Stokes equations computationally results in spatial fields of the pressure and the three components of velocity. Other metrics can be derived from these variables, such as flow rate, hydraulic resistance, and viscous dissipation. Modeling a passive scalar produces a concentration field, where higher concentrations represent the presence of less diluted contrast. Lagrangian particle tracking provides trajectories of platelets over time, and the residence time and shear stress history along the trajectories can be computed.

Comparing clinical measurements and experimental results to the computational model can validate the CFD results. The study of vasospasm benchmarks key model parameters against clinical literature values demonstrated in sections 2.2.7 and 2.3.2 and compares virtual angiography performed in the CFD model to clinical angiography as demonstrated in section 2.3.3. The LVAD study utilizes results from a PIV experiment to benchmark the velocity profiles, illustrated in section 3.3.1, as well as the stagnation index fields, which is an Eulerian metric for stagnation, illustrated in section 3.3.2.

1.4 Computational Modeling of Cardiovascular Fluid Mechanics

Lumped parameter models reduce arterial networks into a zero-dimensional problem by using a circuit analogy for components of the vascular network [165]. The current is analogous to flow through the artery, and the voltage is analogous to pressure drop across the artery. Resistors characterize the viscous losses in the artery, inductors characterize the inertial effects of the flow, and capacitors model the storage of fluid due to the elastic behavior of the vessel wall. Model parameters must be tuned to match physiologically realistic conditions. Lumped parameter models offer a computationally inexpensive way to model time-varying pressure and flow through the entirety of the vasculature. However, they do not account for varying geometrical properties of specific arteries, such as the change in diameter or the different angles in the bifurcations, which result in different pressure wave transmission and reflection, affecting flow-pressure values and timing.

One-dimensional models characterize the spatial and temporal changes in pressure and flow, assuming that each component of the network can be described with the approximation that the main changes in flow variables are determined by the evolution along only one spatial direction along the artery centerline. This approach assumes that the flow can be characterized with pressures and velocities averaged across the cross-section but varying in the axial direction. The Navier-Stokes and continuity equations that govern fluid flow are reduced to one dimension by assuming incompressible axisymmetric flow [124]. The elasticity and geometric features of the vessels must be defined [159]. One-dimensional models can be coupled with lumped parameter models (0-D) to improve the behavior of the model by taking into account the parts of the vasculature upstream and downstream of the section modeled in 1D [7]. While 1D models do not inherently account for three-dimensional flow behavior, attempts have been made to incorporate losses associated with curvature, bifurcations [124], and stenosis [146]. However, one-dimensional models cannot

capture three-dimensional phenomena like mixing and mass transport.

Using CFD, the three-dimensional pressure and velocity profiles in cardiovascular flows can be studied. The Navier-Stokes and continuity equations are discretized in space and time, then solved numerically. Spatial discretization is achieved by creating a mesh in which cells conform to the shape of the geometry and define where the dependent variables of the simulation are computed. A time-stepping algorithm is applied to advance each model degree of freedom to the next time step using a numerical scheme that approximates the differential equations being solved. CFD simulations can provide spatial fields of quantities like wall shear stress which have been implicated in the development atherosclerosis [109] and rupture of intracranial aneurysms [28]. Other applications of CFD in the vasculature include modeling of the carotid bifurcation [100], coronary lesions [112], aortic aneurysms [55], aortic dissections [33], and stenting [147]. Cardiac flows have been extensively studied using multiphysics simulations [108]. Fluid-structure interaction can capture the ventricular wall motion surrounding the fluid domain [32, 103]. Lagrangian particle tracking models the transport of particles in a velocity field and can be used to evaluate the degree of mixing and the residence time of blood in the heart [103].

Patient-specific modeling is essential for creating physiologically realistic computation simulations, as one of the key characteristics of cardiovascular fluid mechanics is that the transitional Reynolds numbers and the pulsatility of the flow make the flow features critically dependent on the specifics of the geometry of the vessels. To capture the anatomy of a specific patient, the geometry can be derived from CTA [69], MRI [29], 3D rotational angiography [73], or 3D ultrasound [104]. Time-varying waveforms that describe the velocities or flow rates in vessels can be derived from PC-MRI [17, 29, 177] or ultrasound measurements [104] and used to apply boundary conditions to the model. However, clinical data is not always available to incorporate into CFD simulations. Some authors use generic boundary conditions sourced from literature values, typically extracted from measurements on a small cohort of healthy,

young volunteers [9, 73]. Other authors use unrealistic boundary conditions like zero pressure on both branches of a bifurcation [9, 133, 177], which can affect the fidelity of the model [61].

Validation of computational models with clinical data can increase confidence in the results of the CFD simulation. Berg et al used 4D-MRI to set boundary conditions of a cardiovascular model, then compared the CFD velocity profiles inside the flow domain of the cerebral vasculature to the 4D-MRI collected at the same plane inside the flow domain, different from the measurement plane used as a boundary condition [17]. They found that the qualitative shape of the profile, as well as the pointwise comparison of individual values, agreed closely between the CFD and 4D-MRI. Bonfanti et al studied flow in an aortic dissection, which occurs when there is a tear in the aorta that creates a false lumen [20]. They found that direction of motion inside the dissection from 2D cine MRI corresponded to the direction of the pressure gradient across the dissection. Holmgren et al studied stump pressures during the clamping of the carotid artery, finding good agreement with clinically measured stump pressures [68].

As the fidelity of computational models increases, patient-specific interventions can be planned. HeartFlow has developed an FDA-approved computational tool based on CTA in the coronary arteries to calculate the fractional flow reserve, which can differentiate between nonobstructive and hemodynamically significant lesions [16], and indicate the need and optimal location of cardiac interventions.

One of the main challenges in modeling cardiovascular flows arises from the uncertainties in the input parameters to the simulation, including the geometry derived from medical imaging, material properties, and boundary conditions. Steinman and colleagues have investigated the effects of assuming Newtonian flow behavior and fully developed inlet flow on CFD metrics by manually changing input conditions to the simulation [86, 113]. More sophisticated methods can be used to propagate uncertainties from model inputs into uncertainties in hemodynamic quantities [142].

Chapter 2

ACTIVATION OF COLLATERAL PATHWAYS IN THE CIRCLE OF WILLIS DURING VASOSPASM

2.1 Introduction and Background

2.1.1 The Circle of Willis

The Circle of Willis (CoW) is a redundant network of blood vessels that supplies oxygen to the brain. The CoW is supplied by three major arteries – the two internal carotid arteries (ICAs) and basilar artery (BAS) – and perfuses cerebral tissue primarily through six major arteries – two anterior cerebral arteries (ACA), two middle cerebral arteries (MCA), and two posterior cerebral arteries (PCA). Primary collateral pathways – the ACA A1 segments, PCA P1 segments, posterior communicating arteries (Pcom), and anterior communicating artery (Acom) connect these supplying vessels forming the ring-like structure of the CoW. The anatomy of the CoW is represented in Fig. 2.1.

The primary collateral pathways that connect the major blood vessels within the CoW can be recruited to mitigate the negative effects of vessel occlusion by changing the direction or magnitude of flow in the communicating segment. However, only 40% of the population has a complete and balanced CoW, i.e., all vessels are present and of typical sizes [15].

2.1.2 Activation of Collateral Pathways

In response to non-physiological conditions in the CoW, the vasculature will dynamically autoregulate in an effort to restore typical perfusion to the affected areas [34]. Extensive clinical research has been conducted on the response of primary

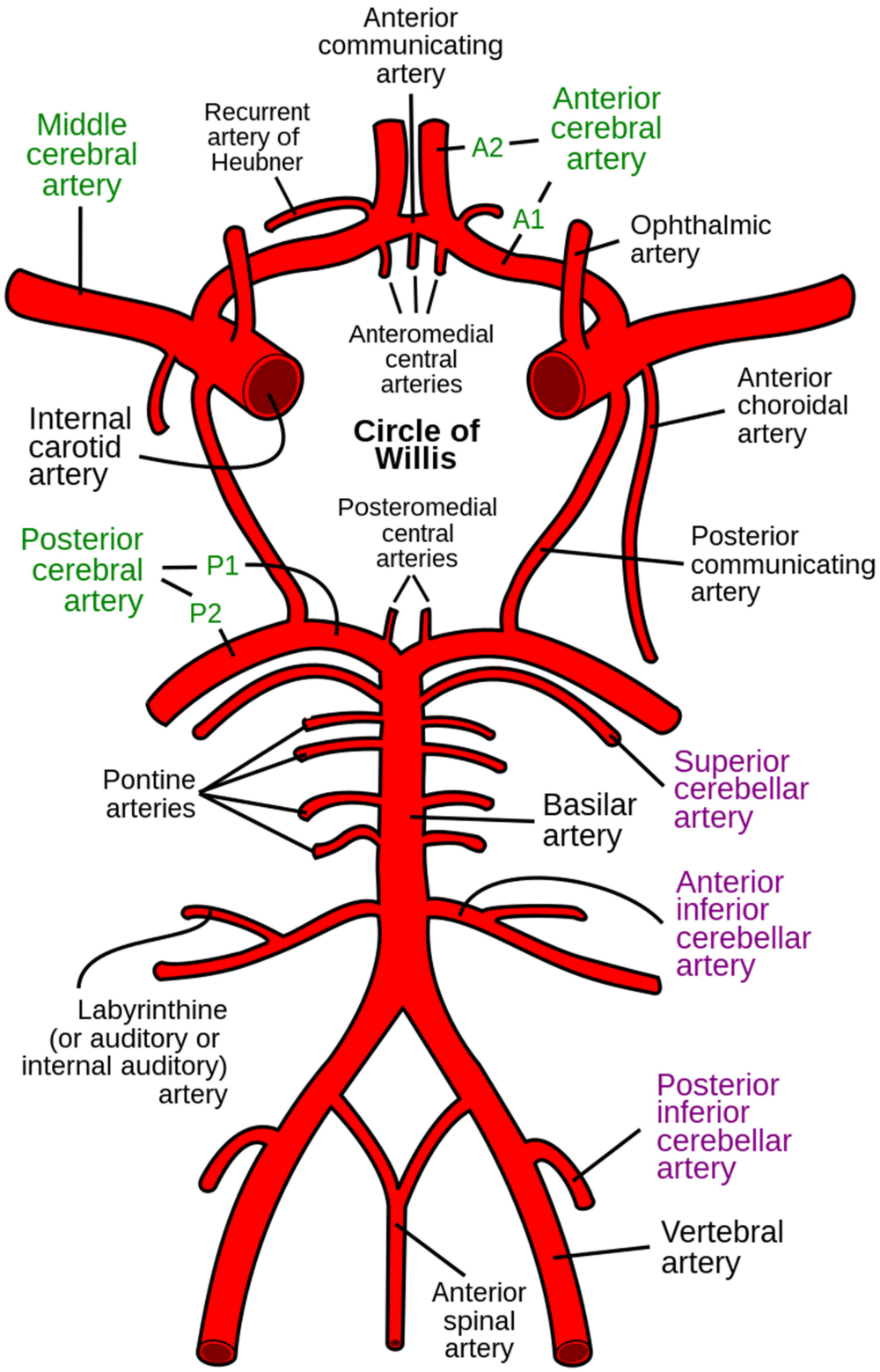

Figure 2.1: Anatomy of the Circle of Willis

collateral pathways in the CoW to stroke [13, 23, 40, 79, 173] and ICA occlusion [19, 46, 65, 81, 91, 116, 132, 137, 140, 144, 163, 168] using transcranial Doppler ultrasound (TCD) [19, 46, 65, 91, 116, 132, 137, 140, 163, 168, 173], transcranial color-coded duplex sonography [81], digital subtraction angiography (DSA) [13, 19, 23, 40, 46, 65, 91, 79, 116, 168], and magnetic resonance angiography [19, 65, 140, 144, 163]. Specifically, researchers attempt to identify which collateral pathways are activated under these conditions and what is their impact on clinical outcomes.

During ICA occlusion, significant changes in flow in the anterior circulation, i.e., the Acom and ACA A1 segment [19, 46, 65, 91, 116, 132, 137, 140, 144, 163, 168], and the posterior circulation, i.e., the Pcoms [65, 81, 91, 116, 132, 137, 140, 144, 163], have been observed. Some authors identify the Acom as the most important collateral pathway for reducing the incidence of infarct [19, 137] and maintaining physiological MCA velocities [46]. Other authors found that the Pcom is most important for reducing the incidence of infarct [144] or equally important for maintaining physiological perfusion and metabolism [163]. In the event of MCA stroke, higher degrees of collateralization have been related to reduced sizes of infarct [13, 23, 40, 79, 173]. In these studies, the activation of collateral pathways was observed as caused by a unilateral obstruction in the CoW. Additional complexity is introduced if multiple areas in the CoW are subjected to unphysiological conditions, such as vasospasm described in the following section.

2.1.3 Arterial Wall Structure

Blood vessels are comprised of three layers of tissue: the tunica externa, tunica media, and tunica intima, as seen in Fig. 2.2. The tunica externa is a sheath of connective tissue composed of collagenous fibers. The tunica media is comprised of smooth muscle cells that relax – vasodilate – and contract – vasoconstrict – as a part of autoregulation to promote healthy arterial pressures. The tunica intima is comprised of a thin elastic layer that supports a mono-layer of endothelial cells that detect

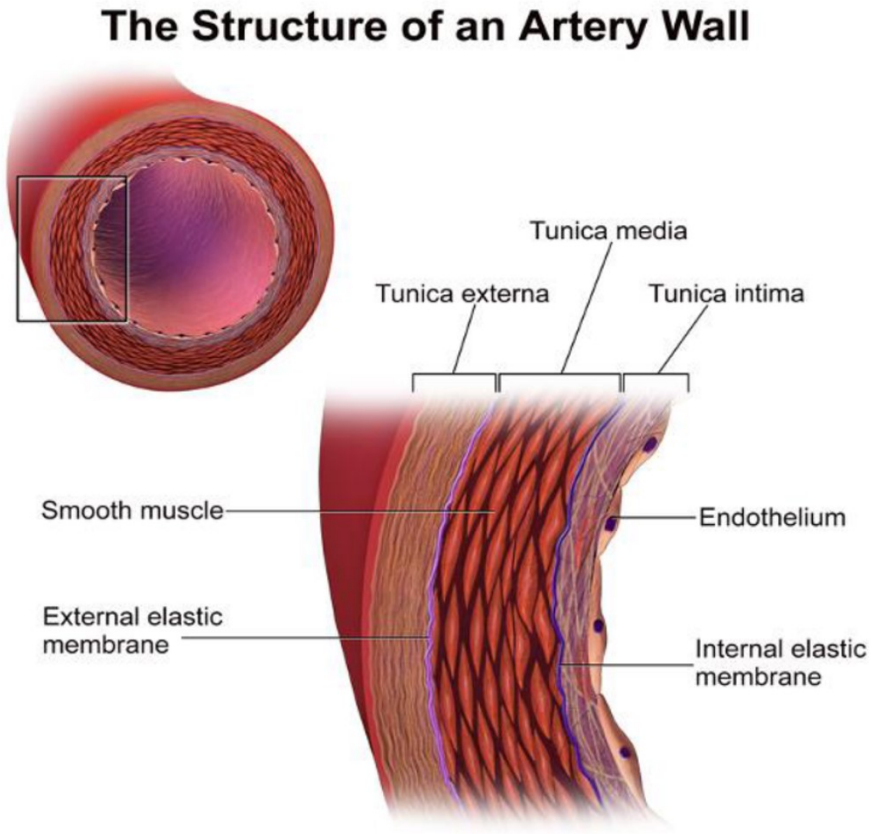

Figure 2.2: Structure of the arterial wall

changes in blood pressure in order to signal the smooth muscle cells in the media to relax or contract.

The blood vessels that comprise the CoW are surrounded by cerebrospinal fluid that occupies the subarachnoid space, as seen in Fig. 2.3. This separation between the blood flowing within the vessel and the cerebrospinal fluid surrounding the cerebral tissue, commonly referred to as the blood brain barrier, is essential to maintaining healthy cerebral tissue.

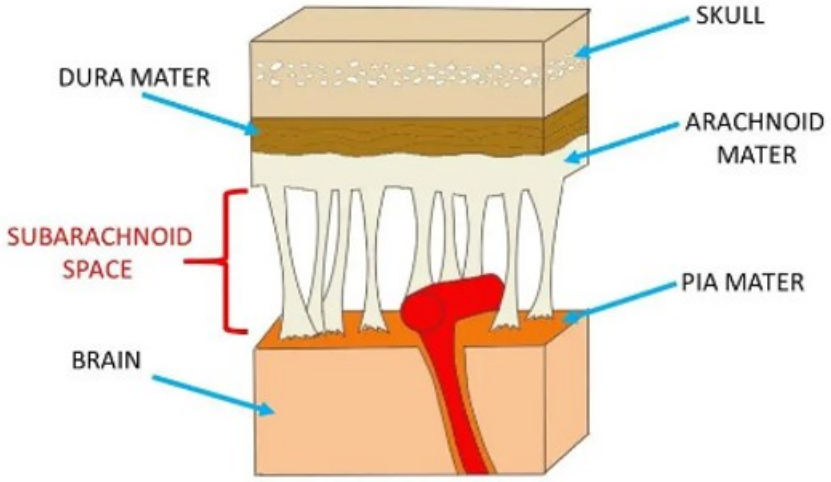

Figure 2.3: Subarachnoid space surrounding the artery

2.1.4 Intracranial Aneurysms and Subarachnoid Hemorrhage

Intracranial aneurysms are abnormal bulges that protrude from the typical vessel wall, developing in about 0.5-6% of the population [18]. When an aneurysm ruptures, it releases blood into the subarachnoid space causing a subarachnoid hemorrhage (SAH). The rate of mortality or incapacitation for SAH is over 50% [80]. For patients who survive the initial rupture, the primary clinical intervention is to manage the aneurysmal bleeding. Clinicians can deploy endovascular treatment to the aneurysm, filling the aneurysm with platinum coils [167]. Alternatively, a surgical clip can be used to isolate the aneurysm from the parent vessel [167].

2.1.5 Vasospasm

The blood introduced to the subarachnoid space breaks down into reactive oxygen species and oxidation blood products that interact with the outer vessel wall [50]. This interaction is thought to cause or contribute to vasospasm— an involuntary constriction of the blood vessel due to the contraction of smooth muscle in the tunica

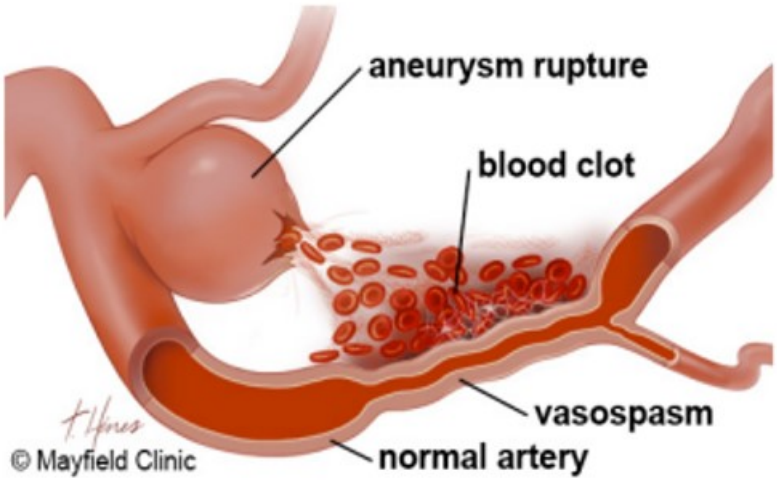

Figure 2.4: Ruptured aneurysm introducing blood to the subarachnoid space leading to vasospasm

media (Fig. 2.4).

Vasospasm can significantly decrease perfusion to the brain, causing neurological deficits and infarct [71]. Blood is introduced into the subarachnoid space primarily at the location of aneurysmal rupture. However, vasospasm can appear in any of the blood vessels comprising the CoW. Vasospasm is detected in 50–90% of patients within two weeks of aneurysmal rupture and peaks in incidence between 3 and 7 days [50]. Clinicians monitor all major cerebral vessels daily for vasospasm.

2.1.6 Transcranial Doppler Ultrasound (TCD)

Transcranial Doppler ultrasound (TCD) is a non-invasive method of detecting changes in blood flow velocities within vasculature [4]. When collecting data in the CoW, a Doppler ultrasound probe is placed in an acoustic window of the skull, which is a location where the cranial bone is thin enough to let the ultrasound transmit without significant attenuation or distortion. The probe is angulated to align the Doppler

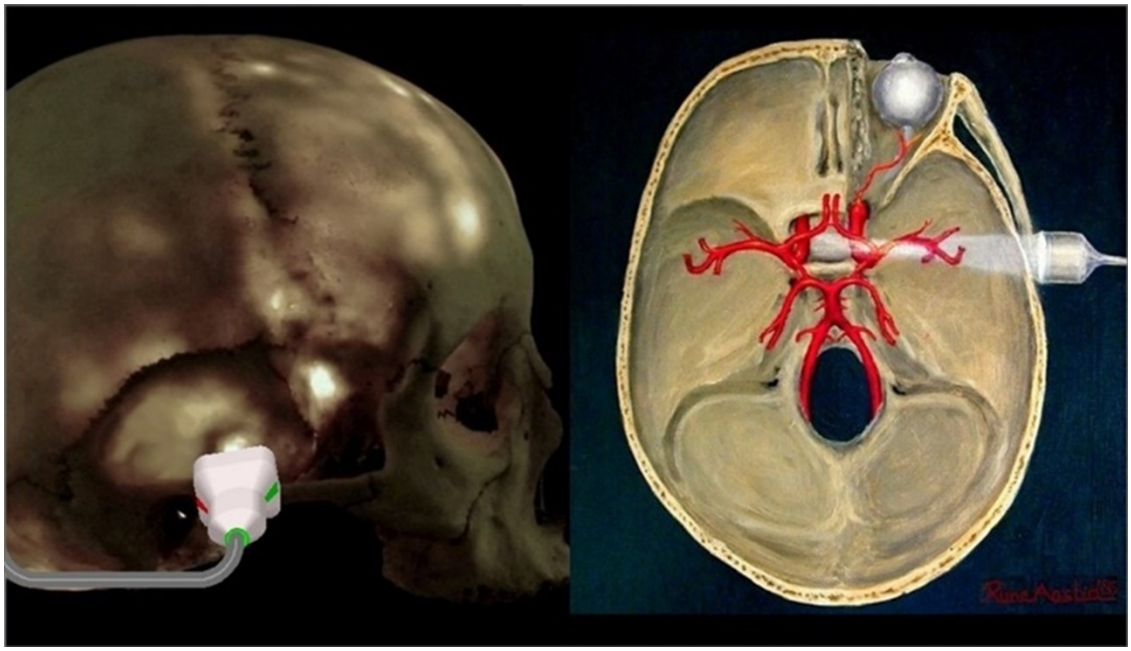

Figure 2.5: Transcranial Doppler ultrasound (TCD) transducer insonating a cerebral artery

beam with the centerline direction of different vessels in the CoW (Fig. 2.5). Once the sample volume—the region of the intracranial cavity insonated by the ultrasound beam—is placed inside the vessel of interest, the velocity signal acquired by the TCD sensor is recorded.

The ultrasound return is catalogued at multiple depths for most of the insonated vessels, where a lower depth indicates that the sample volume is closer to the transducer than to the midline of the brain. The direction of flow can help differentiate between different segments of the CoW, with flow towards the transducer corresponding to the depth set in the red zone and a positive velocity spectrum (Fig. 2.6, top) and flow away from the transducer corresponds to the depth set in the blue zone and a negative velocity spectrum (Fig. 2.6, bottom). TCD readings are recorded in the MCAs, ACAs, PCAs, BAS, vertebral arteries, and in the extracranial, siphon, and terminal locations of the ICAs.

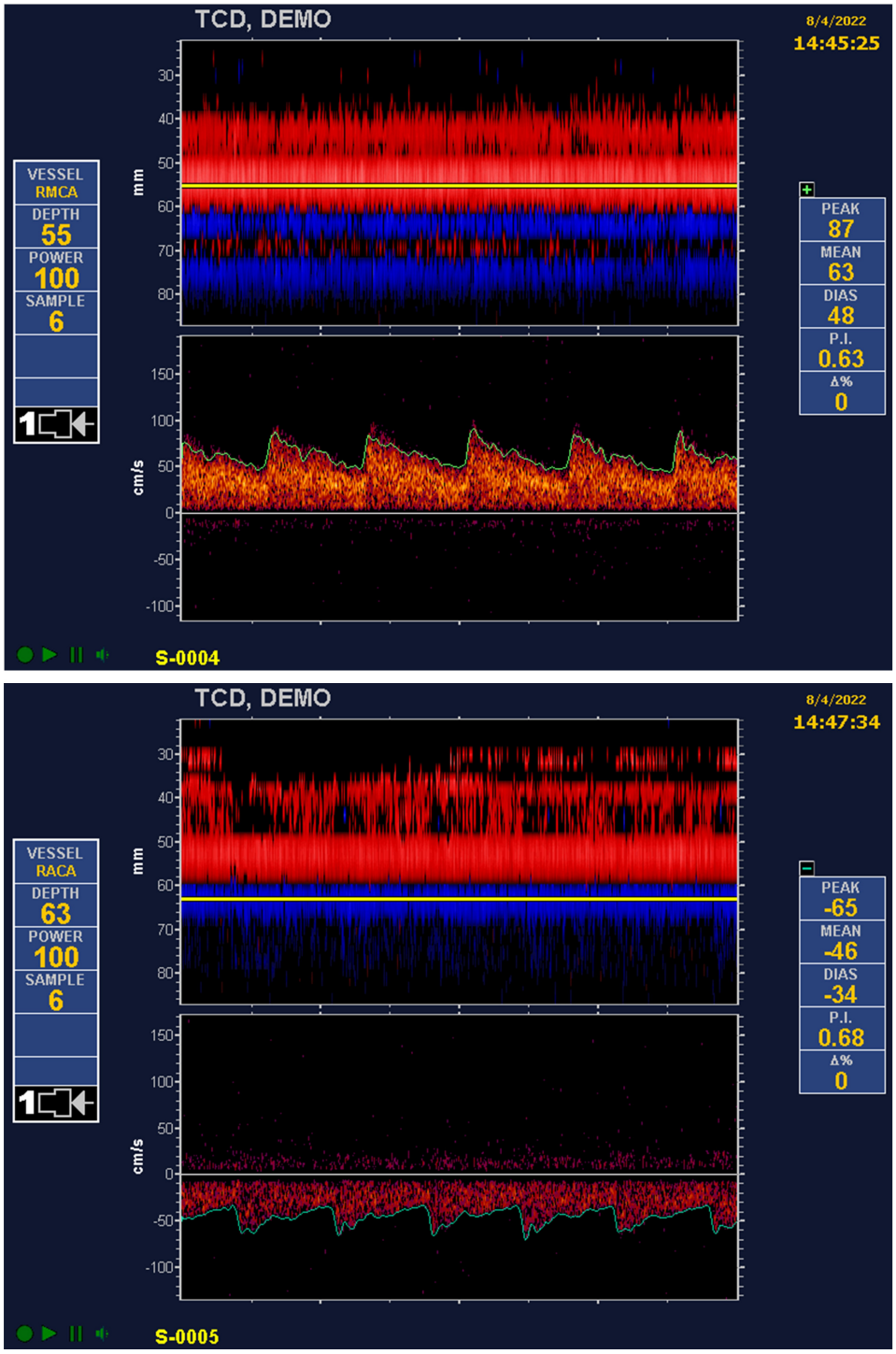

Figure 2.6: Velocities returned by the TCD transducer for flow towards the transducer (top) and away from the transducer (bottom)

In SAH patients, TCD measurements are collected daily to monitor for the onset of vasospasm. Elevated velocities in any of the segments are potential indicators for vasospasm. The Lindegaard ratio is calculated as the ratio of the mean velocities in the MCA and the ipsilateral extracranial ICA, with a ratio of 3-6 reflecting moderate vasospasm and above 6 reflecting severe vasospasm in the MCA. In response to a significantly abnormal TCD exam or a change in neurological condition, a computed tomography scan is performed to verify the presence of vasospasm prior to intra-arterial treatment.

2.1.7 Computed Tomographic Angiography (CTA)

Computed tomographic angiography (CTA) scans are performed on SAH patients upon admission and during a period of suspected vasospasm. CTA collects X-ray measurements from different angles and computes a volumetric reconstruction of the signals that can be visualized as cross-sectional images of the vasculature, called "slices". The resolution of the scan is reflected in the pixel size in each slice, referring to the spatial discretization of the image. The slices are stacked in a three-dimensional representation of the brain vasculature (Fig. 2.7). The lumen of the blood vessels can be identified by a difference in pixel intensity between the blood (higher intensity due to the presence of contrast) and surrounding tissue (lower intensity).

Once the presence of vasospasm has been confirmed in the CTA, digital subtraction angiography is performed.

2.1.8 Digital Subtraction Angiography (DSA)

Digital subtraction angiography (DSA) is collected upon admission and after the confirmation of vasospasm in SAH patients. Radio-opaque contrast is injected into the vessels supplying the CoW, i.e., the vertebral arteries and ICAs, and X-rays images are collected at different snapshots in time. In the admission scan, clinicians can measure the dimensions of the aneurysm to be treated and determine the variation

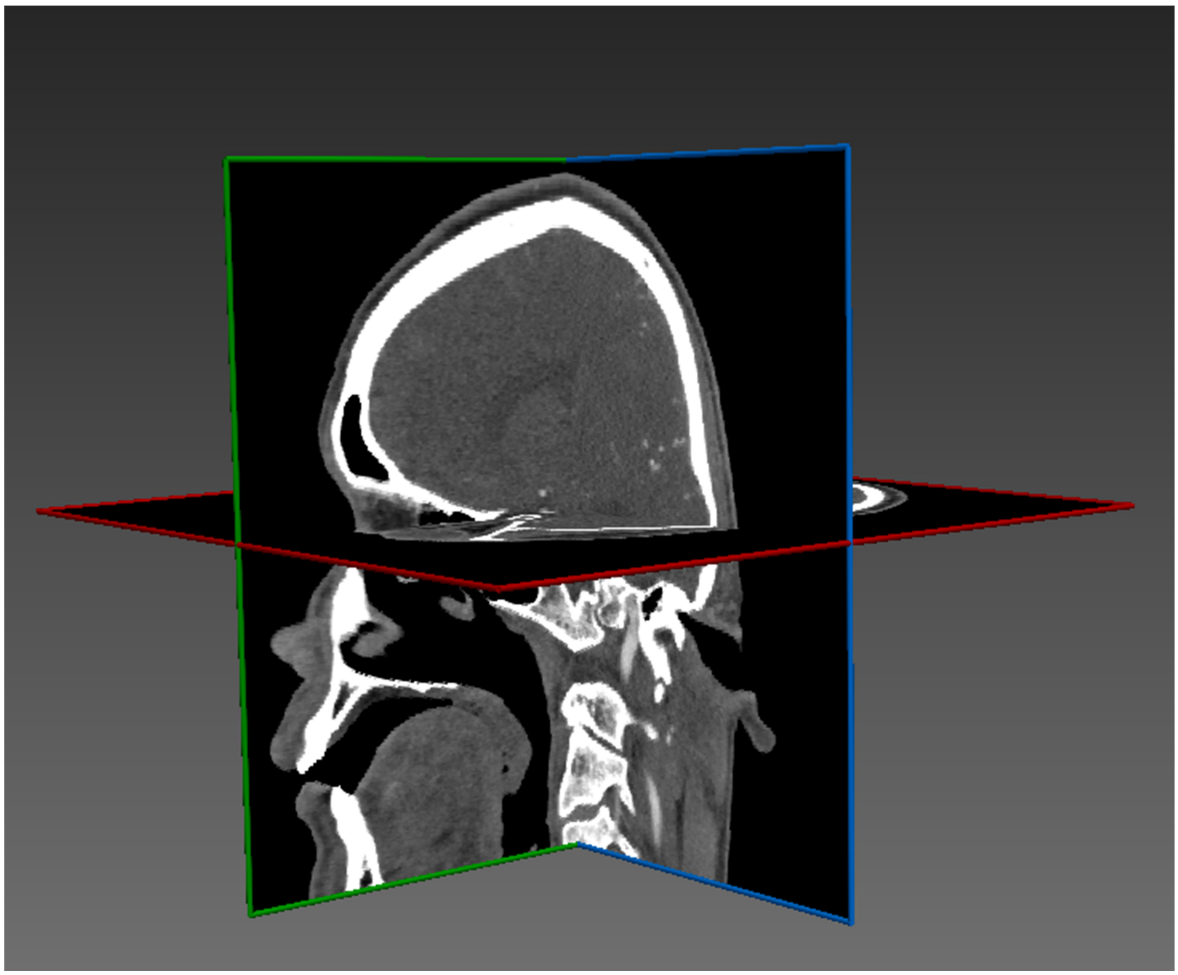

Figure 2.7: Computed tomographic angiography (CTA) of the brain

of the CoW. In the vasospasm scan, clinicians can diagnose the severity of vasospasm by examining the caliber of the vessels in the CoW and by observing the time it takes for contrast to fill the downstream vasculature.

In vasospasm patients, flow in the anterior circulation can be visualized during left and right ICA injections in two views: anterior-posterior (AP) and lateral. Flow in the posterior circulation is visualized with a vertebral injection in the AP and lateral views.

Figure 2.8 provides examples of the ICA injections (Fig. 2.8a,b) and vertebral injections (Fig. 2.8c,d) in the AP (Fig. 2.8a,c) and lateral views (Fig. 2.8b,d). In the ICA injection in the AP view (Fig. 2.8a), the contrast is visualized in the MCA and ACA. The direction of flow in the Acom can be determined by detecting contrast in the contralateral side of the distal ACA circulation. Retrograde flow through the contralateral ACA A1 segment can be determined. Reverse flow in the ipsilateral PCA P1 segment can be visualized with contrast filling the contralateral posterior circulation. The calibers of the TICA, MCA, and ACA are evaluated from this view. In the ICA injection in the lateral view (Fig. 2.8b), the presence of a Pcom can be determined by identifying a communicating vessel between the supraclinoid ICA and the posterior circulation. This view enables the caliber of the TICA and Pcom to be determined. The vertebral injection in the AP view (Fig. 2.8c) shows the filling of the bilateral PCAs, and the caliber of the BAS and bilateral PCAs can be assessed. The lateral view of the vertebral injection (Fig. 2.8d) can detect retrograde flow in the Pcom, i.e., flow towards the anterior circulation.

Once the locations of vasospasm have been identified, neurosurgeons can employ two types of intravascular interventions: the injection of intraarterial vasopressors and balloon angioplasty [50]. Intraarterial vasopressors promote vasodilation in the constricted vessels and can reach the smaller vessels of the downstream vasculature. Balloon angioplasty increases the caliber of larger vessels comprising the CoW through the inflation of an intraarterial balloon.

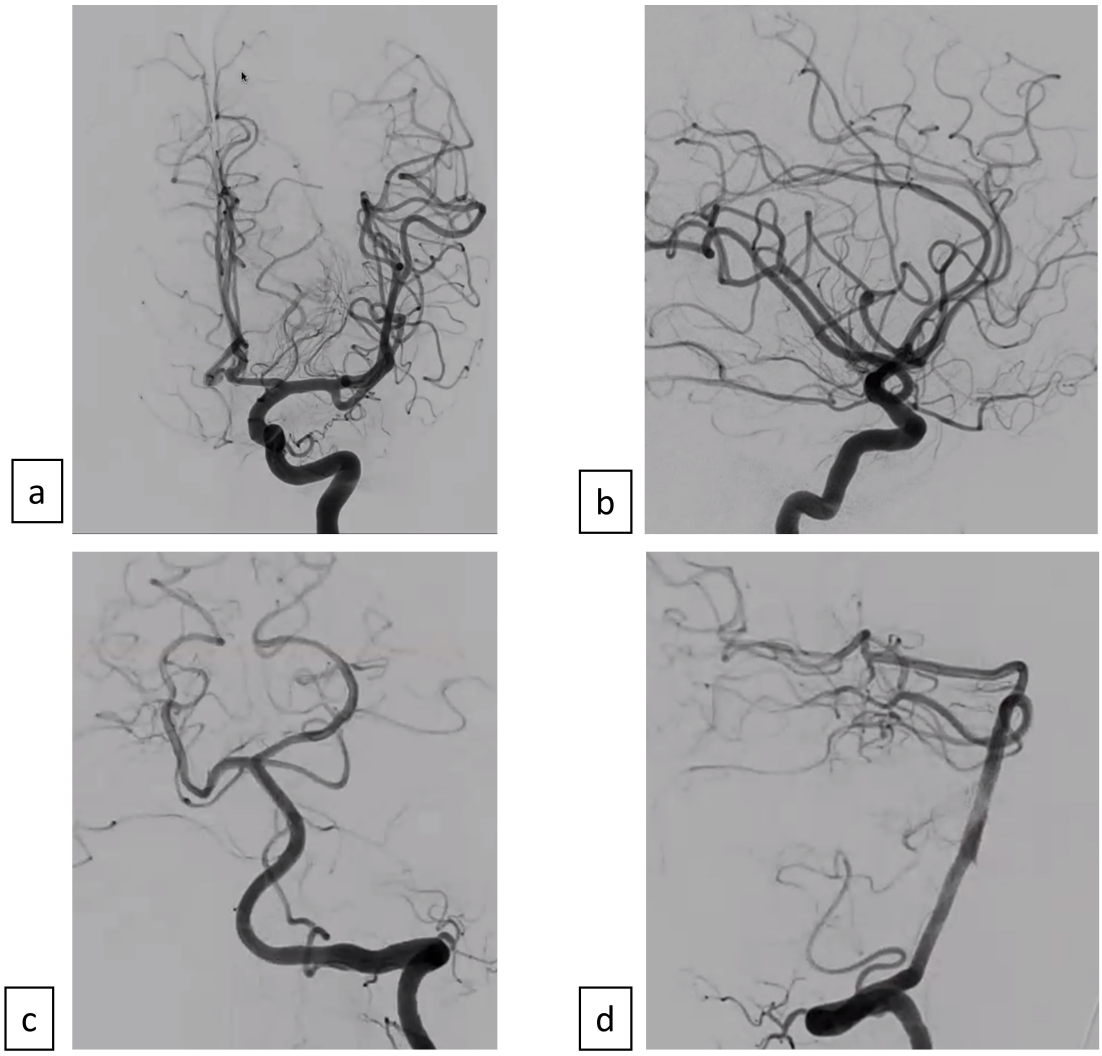

Figure 2.8: Digital subtraction angiography (DSA) for an internal carotid artery (ICA) injection in the anterior-posterior view (a) and lateral view (b) and a vertebral artery injection in the anterior-posterior view (c) and lateral view (d)

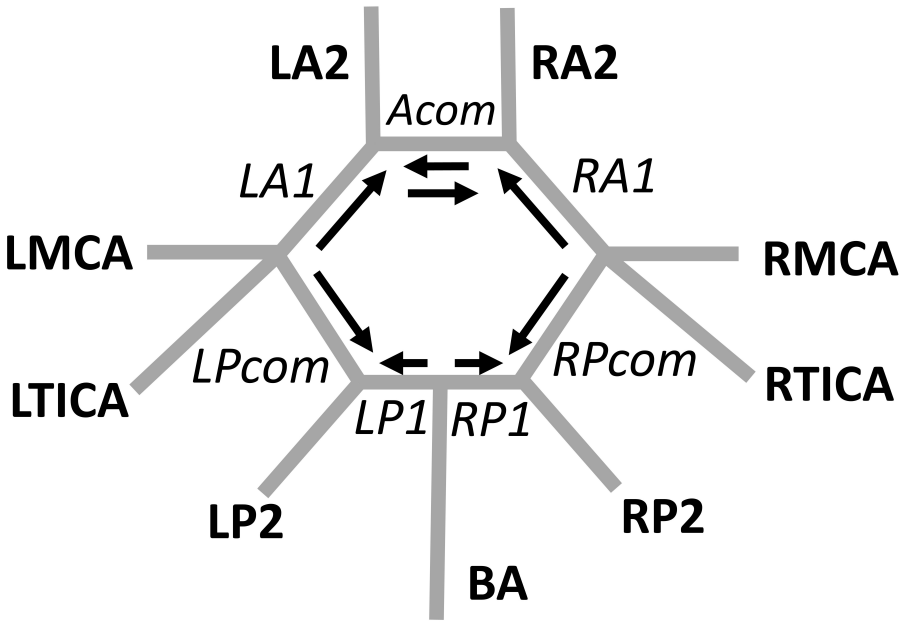

Figure 2.9: Direction of antegrade flow in the collateral pathways of the Circle of Willis

2.1.9 Changes in Flow in Collateral Pathways

Flow in the collateral pathways was considered antegrade if the flows in the ACA A1 segments were towards the ACA A2 segments, flows in the PCA P1 segments were towards the PCA P2 segments, and flows in the Pcom segments were from the anterior circulation to the posterior circulation, as shown in Fig. 2.9. Retrograde flow was defined as the direction opposite to antegrade flow, and biphasic flow was defined as flow alternating between antegrade and retrograde over the cardiac cycle. Flow in the Acom was identified as left to right, right to left, biphasic, or no net flow.

The collateral flow directions were compared between the baseline and vasospasm conditions. This work studies changes in direction or magnitude of the flow in collateral pathways, in relation to the changes in the dynamics of the CoW during vasospasm. Increased flow magnitude was identified by increased robustness of filling

of the distal vasculature or a noticeable increase in the size of a collateral pathway. Decreased flow magnitude was identified by weaker filling of the distal vasculature. In the bilateral ACA A1 segments, PCA P1 segments, and Pcoms, a change in direction was defined as antegrade to biphasic flow and vice versa, retrograde flow to biphasic flow and vice versa, antegrade to retrograde flow and vice versa, or no net flow to directional flow and vice versa. In the Acom, a change in direction was defined as left-to-right transitioning to right-to-left and vice versa, or no net flow to directional flow and vice versa.

This study examines changes in flow direction but does not label these changes as "recruitment". The changes in flow can be a result of recruitment of collateral pathways to supply an area in vasospasm, but they can also appear due to vasospasm in the segment, e.g., weakening flow due to severe vasospasm.

2.1.10 Clinical Studies of Collateralization in Vasospasm Patients

Studies of the activation of collateral pathways are well-represented in the literature for ICA occlusion and MCA stroke, as described in section 2.1.2. In contrast, few authors have systematically investigated the activation of collateral pathways during vasospasm [6, 110, 134, 161].

Moftakhar et al. studied 17 pediatric patients presenting with vasospasm after aneurysmal rupture SAH [110]. They used a 5-grade scoring system developed for studying ischemic stroke for which the degree of collateralization is determined based on the filling of the vasculature downstream of the narrowing [40]. Three patients were symptomatic for vasospasm, all exhibiting poor collateralization. Of the 14 asymptomatic patients, 10 showed some degree of collateralization. This study suggests that the degree of collateralization influences the likelihood of presenting with symptoms during vasospasm. However, the sample size was small, and pediatric vasospasm is not representative of the broader population.

Al-Mufti et al. investigated 64 adults with vasospasm after aneurysmal SAH [6]

The American Society of Interventional and Therapeutic Neuroradiology/Society of Interventional Radiology (ASITN/SIR) Collateral Flow Grading System, which is a 5-grade score based on the speed and extent of flow to the ischemic site through collaterals, was used to categorize patients' degree of collateralization [149]. The severity of vasospasm was assigned based on the percent luminal narrowing as mild ($< 30\%$), moderate, ($30-50\%$), or severe ($> 50\%$) in the DSA. Long-term neurological functional status and the incidence of infarct were assigned as patient outcomes. They found that patients with poor collateral grades were significantly more likely to have mild vasospasm than those with good collateral grades. However, they did not find a statistically significant relationship between the degree of collateralization and patient outcomes.

Topcu et al. analyzed a cohort of 59 adult SAH patients with vasospasm [161], using ASITN/SIR to grade the degree of collateralization [149]. The degree of vasospasm was assigned with a 5-grade angiographic scale for evaluating cerebral vasospasm across multiple vascular axes, e.g., ICA, MCA, etc. [121]. Patients with new neurological deficit or impaired consciousness for more than 1 hour, or who showed new cerebral infarcts on CT/MRI, were diagnosed as having delayed cerebral ischemia (DCI). This study found that patients with DCI were more likely to have severe vasospasm or poor collateral status. No statistically significant difference in vasospasm severity was found between patients with good and poor collateral status.

Richter et al. studied the activation of leptomeningeal and ophthalmic collaterals in 43 adults with vasospasm [134]. The authors found no statistically significant correlation between the angiographically visible leptomeningeal collaterals and mRS or infarct caused by vasospasm.

The role of primary collateral pathways in the CoW during vasospasm, and its impact on brain perfusion, the occurrence of stroke and patient outcomes, remains an open question.

2.1.11 Computational Fluid Dynamics Studies of the Circle of Willis

Previous CFD studies of the CoW served as proof-of-concepts [29, 54, 61, 127] and investigated different pathologies: aneurysm formation and dynamics [17, 73, 177], the transport of emboli to the CoW [115], cerebrovascular occlusive disease [143], pressure changes due to intracranial stenosis [92], and changes in collateral flow rates [77, 111] and pressure [68, 69] in response to carotid stenosis or occlusion. Methodologies across the literature vary with respect to selecting realistic boundary conditions, incorporating autoregulation, deciding on constitutive relations for blood and the vessel walls, and validating the model.

The physiologically most realistic way to prescribe inlet conditions is to apply a patient-specific pulsatile waveform for the velocity or the flow rate. If the peak velocity or flow rate is known, the waveform can be converted into a Womersley profile – a pulsatile axisymmetric velocity profile created from Fourier coefficients of the modes in the original waveform. Cebral et al. integrated phase-contrast magnetic resonance imaging (PC-MRI) measurements of velocity across the voxels associated with the ICAs and BAS to calculate the total flow rates, then converted them into Womersley velocity profiles prescribed at the inlets [29]. Berg et al. applied the PC-MR flow rates to a round inlet, with an entrance length of six diameters, to create a fully developed velocity profile [17], while Zuleger et al. prescribed the measured velocities from PC-MR data directly to the inlets [177]. In the absence of patient-specific measurements, some authors used generic published waveforms [9, 73]. The most simplified analyses prescribed a constant pressure at the inlets [93, 133], which loses information about the significant pulsatility in the flow as well as asymmetries that can occur between the left and right sides of the intracranial vasculature.

The best formulation for outlet conditions also relies on patient-specific data. Cebral et al. applied the PC-MR derived Womersley profiles to some outlets - the anterior and middle cerebral arteries - as well as the inlets, and used a no traction

condition to the posterior cerebral arteries to avoid overconstraining the problem [29]. This technique provided an innovative way to incorporate as much patient-specific data as possible into the boundary conditions. Berg et al. used PC-MR measurements to prescribe the appropriate flow splits between the major cerebral arteries [17]. To address a lack of patient-specific data, some authors [73] will use literature values for the appropriate flow splits [158]. As demonstrated by Grinberg et al. [60], the flow splits can also be defined using resistance values, oftentimes in conjunction with a capacitance to account for the compliance in the downstream vasculature via RC or RCR conditions. The most unrealistic boundary condition is the constant pressure outlet condition, which assumes that the downstream resistance for all outlets is identical. As shown by Grinberg et al. in their work on outflow boundary conditions, using constant pressure conditions instead of the more realistic RC boundary conditions can create a 300% difference in the flow rates [61]. Despite this inaccuracy, it is not uncommon to see a constant pressure boundary condition being applied [9, 133, 177].

Autoregulation occurs when blood vessels vasodilate or vasoconstrict to regulate the amount of flow through the branches of the CoW. While autoregulation is commonly included in reduced order models, only a handful of CFD studies have incorporated it. Moore et al. included porous blocks at each outlet to model the resistance of the downstream vascular beds, using a feedback loop to change the permeability until the expected flow rate was reached [111]. Kim modeled the downstream vascular bed with a network of resistors and updated the flow resistance ratio until the reference flow rate was attained [77]. Sutalo et al. coupled a 1D branching tree model to the outlets and varied the diameters in the branching tree based on changes in wall shear stress [156]. Incorporating an autoregulation model allowed the authors to capture the dynamical response to changes in the upstream [77, 111] or downstream [156] vasculature.

Blood is an inhomogeneous fluid, comprised of cells and plasma, that exhibits

non-Newtonian behavior. On a macroscopic level, blood is usually modeled as a homogeneous material with a constant density. Most of the reviewed studies considered blood as a Newtonian fluid [9, 54, 73, 93, 115, 133, 143, 177], while some of the studies applied the Carreau-Yasuda model to incorporate shear-thinning behavior [77, 111, 127]. Other authors compared the results between Newtonian and non-Newtonian models and found that the wall shear stress and velocity profiles were only slightly different between the two cases [17, 29]. A simulation of the carotid bifurcation suggested that the error introduced by assuming Newtonian behavior is well below the error introduced by the inaccuracies in the segmentation [86], suggesting that including a non-Newtonian model increases computational complexity with little improvement in model accuracy.

Blood vessels are inherently compliant, passively expanding early in the cardiac cycle and relaxing later in the cardiac cycle. These changes are especially pronounced in the larger vessels, with smaller changes occurring in the downstream vasculature. To fully model this behavior, fluid-structure interactions would need to be incorporated into the model. The vast majority of the existing CFD literature for the CoW models the vessels as rigid, with one exception which incorporated a thin-walled, linear elastic model for the vessel walls [78]. Fluid-structure interactions are computationally expensive, and the lack of available data for the material properties of tissues compounds this challenge [12].

CFD simulations can be validated or improved by using clinical data. Berg et al. compared 4D PC-MRI velocity profiles to CFD, finding good qualitative agreement of the velocity profiles at the ICA, BAS, and ACA, as well as pointwise agreement in the magnitude and direction of velocities at hundreds of locations [17]. Similarly, Perinajova et al. performed a voxel-to-voxel comparison at 10 slices of the MRI velocity magnitude against the CFD velocity magnitude, finding good agreement [127]. Liu et al. computed the fractional pressure ratio in patients with intravascular stenosis and compared it clinical measurements from a pressure guidewire, finding good agreement

between the CFD results and clinical measurements [92]. Holmgren et al. compared clinically measured stump pressures in 28 patients during carotid endarterectomy to CFD values, finding statistically significant agreement [68]. Gaidzik et al. explored a novel technique for integrating PC-MR results with CFD using data assimilation, that reduced uncertainty in flow rates and wall shear stress while improving agreement of the CFD velocity magnitudes with the PC-MR measurements [54]. Schollengberger et al. calibrated and validated their CFD models of two patients with cerebrovascular occlusive disease and one healthy patient using arterial spin labeling MRI [143].

High fidelity CFD simulations can be created when patient-specific boundary conditions are incorporated into the model. Benchmarking the CFD model against clinical data improves the validity of the results.

2.1.12 Computational Fluid Dynamics Studies of Vasospasm

Reports of CFD simulations of intracranial vasospasm in the literature are rare. Chittiboina et al. simulated flow through an idealized stenotic MCA M1 segment with different amounts of hematocrit to understand the implications of hemodilution on oxygen transport [35]. Robinson et al. created an idealized model containing the ICA, MCA, and ACA to determine the role of hemodilution on flow through MCA stenosis [138]. Shiba et al. created CFD simulations in patient-specific models of subsections of the CoW, with no clear metrics extracted from the CFD [150].

2.1.13 Study Overview

This study investigates interactions between localization of vasospasm in the CoW, the overall severity, and the anatomical variation on changes in flow in primary collateral pathways. Patient-specific CFD simulations were created for 25 vasospasm patients. CTA scans were segmented capturing the anatomical variation and vessel narrowing due to vasospasm. TCD measurements were used to define boundary conditions. DSA indicated the directions and magnitudes of flow in the collateral pathways, as well

as vasospasm severity in each vessel. Bayesian analysis optimized model parameters based on quantification of uncertainties in the clinical data and the principle of mass conservation. Diameters, velocities, and flow rates at the inlets and outlets were benchmarked against literature values. Virtual angiograms modeled using passive scalar transport were compared to clinical angiography. A sensitivity analysis was performed to quantify the changes in collateral flow rates with respect to changes in the inlet and outlet flow rates. Percent changes in resistance and viscous dissipation from before to during vasospasm quantified vasospasm severity and were compared to angiographic determinations of severity. The degree of localization and overall severity of vasospasm were defined based on percent changes in resistance and viscous dissipation.

Section 2.2 outlines the methodology for creating the patient-specific simulations, and the results from two representative patients from the cohort are presented in detail to illustrate the methodology in sections 2.3.2-2.3.4. Section 2.3.5 compares the CFD metrics based on changes in resistance and dissipation to the evaluation of vasospasm severity from angiography. To explore the relationship between vasospasm, localization and overall severity of vasospasm with changes in flow in the primary collateral pathways, eight patients are discussed in detail in sections 2.3.7-2.3.9. CFD results for the remainder of the cohort are provided in sections 2.3.11-2.3.14. Section 2.4 analyzes the results in further detail and present limitations to the study.

2.2 Methodology

2.2.1 Patient Population and Data Collection

Patients presenting with SAH due to aneurysmal rupture were admitted to Harborview Medical Center in Seattle, WA for treatment. Clinical data was collected retrospectively for the patient cohort following guidelines of the Institutional Review Board. Upon admission for presentation of SAH, a CTA scan was collected to identify

the source of the rupture. DSA was performed within 0-2 days of admission by injecting radiopaque contrast into the supplying arteries and tracking the transport of the contrast to the downstream vasculature. TCD measurements of the blood flow velocities in the major cerebral vessels were collected daily to monitor for vasospasm. When elevated velocities on the TCD exam or a change in neurological condition is detected, the patient received a second CTA scan to confirm the presence of vasospasm. After confirmation of vasospasm, a second DSA was performed to guide interventions such as intraarterial vasopressors and balloon angioplasty treat the vasospastic vessels.

This study aims to compare the hemodynamic changes that occur in the CoW during vasospasm. To form this comparison, data were collected for the "baseline" condition, which is defined as the data collected before the presence of vasospasm, and for the "vasospasm" condition, which is defined as the data collected once the presence of vasospasm was confirmed. Patients were included in the cohort if the following conditions were met:

- Complete data sets of CTA images, TCD measurements, and DSA images were available at both baseline and vasospasm

- Artifacts from surgical clips or coils in CTA scans did not significantly obscure the patient's CoW anatomy

- Baseline TCD measurements were collected no later than two days after the baseline CTA scan

- Baseline DSA was performed no later than two days after the baseline CTA scan

- Vasospasm TCD measurements were collected no earlier than one day before and no later than one day after the vasospasm CTA scan

- Vasospasm DSA was performed no later than one day after the vasospasm CTA scan

- No more than one vessel was missing in the CoW anatomy

DSA images were reviewed with collaborators from the University of Washington Department of Neurological Surgery. For the baseline and vasospasm angiography, the collateral flow directions and magnitudes were determined by observing which territories were supplied by each injection into a supplying vessel, as described in section 2.1.8. In the baseline scan, vessels were identified as present or absent, and present vessels were denoted to be of a typical size, hypoplastic, or of a larger caliber. In the vasospasm scan, vessel narrowing was identified in the MCAs, ACAs, PCAs, BAS and terminal ICA. The clinician identified the severity as absent, mild, moderate, or severe for each segment.

The final cohort consisted of 25 patients representing 5 major anatomical variations: complete (15 patients), missing PCA P1 segment (5 patients), missing ACA A1 segment (3 patients), missing Pcom (1 patient), and missing Acom (1 patient). Within each group of an anatomical variation, patients could additionally present with collateral segments that are hypoplastic or of a larger caliber than typically observed. Therefore, significant anatomical variability was represented across the 25 patients. Two patients had three ACA A2 segments. Because TCD measurements are only available for the left and right ACAs, these patients were modeled with two ACAs where the total perfusion would match that of three segments.

2.2.2 Determination of Infarct

Vasospasm can result in decreased perfusion to certain territories of the cerebral tissue, which can lead to the development of infarct. Infarct can be detected via MRI after presentation of vasospasm. MRI scans taken 7 days after the treatment of vasospasm during angiography were available for two patients in the cohort. Three

neurosurgeons reviewed the scans, agreeing on both the locations of infarct and the origin of the infarct, i.e., due to vasospasm and not the original hemorrhage event or surgical intervention. These two patients are discussed in section 2.3.9.

2.2.3 Patient-Specific Segmentation

CTA scans upon admission and for the detection of vasospasm were acquired as DICOM images. The pixel size within each slice was between 0.39-0.55 mm. To facilitate better reconstruction of the CoW anatomy, the images were interpolated by a factor of 4 using a B-spline method in the open-source tool 3D-Slicer (www.slicer.org). The three-dimensional anatomy was visualized in Radiant (https://www.radiantviewer.com/) to identify key anatomical features that could aid in the segmentation of the anatomy. Figure 2.10 represents the anatomy of a patient with a complete variation.

The interpolated DICOMs were imported into the open-source tool SimVascular (simvascular.github.io) in order to reconstruct the anatomy in a patient-specific segmentation. The segmented vasculature included the ICAs, BAS, MCA M1 segments, ACA A1 and A2 segments, PCA P1 and P2 segments, Acom, Pcoms, OAs, and SCAs. The centerlines of each vessel were identified, and circular contours were applied to represent the vessel wall. Vessel diameters were measured at the circular contours closest to where the TCD measurements were recorded. The diameters identified by clinicians as vasospastic on the vasospasm CTA scan were expected to decrease in size compared with the baseline CTA scan.

2.2.4 TCD Waveform Processing

The TCD readings used in the study were collected at the bilateral MCAs, ACAs, PCAs, extracranial ICAs, and BAS. The maximum velocity detected from the ultrasound return was determined to correspond most closely to the centerline velocity in the vessel. During the TCD exam, measurements for some vessels were recorded at

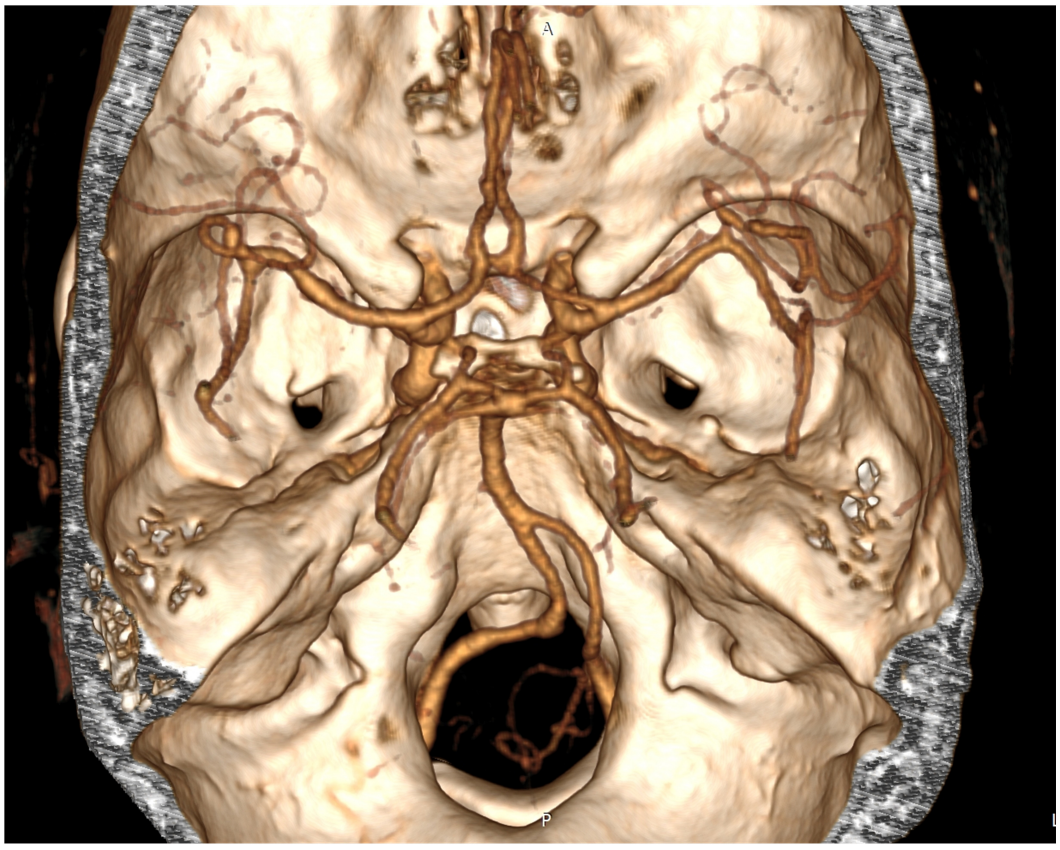

Figure 2.10: Three-dimensional reconstruction of the Circle of Willis in Radiant

multiple depths, where a lower depth indicated that the sample volume was closer to the transducer than to the midline of the brain.

For each segment, the appropriate waveform was selected based on the depth, the magnitude of the mean velocity, and the quality of the measurement. For the ICAs and PCA P2 segments, there was only one available measurement. For the ACA A2 segment, the deepest measurement was selected as closest to the A2 location. For the BAS and MCAs, the highest quality waveforms with the highest mean velocity were typically selected, corresponding to the most favorable angle of insonation. For vessels with diffuse vasospasm, the velocities were higher than the baseline measurement along the entire segment due to the consistently smaller diameter. In vessels with focal vasospasm, the diameter was significantly smaller more proximal to the CoW than the diameter at the outlet, resulting in lower velocities near the outlet. In this case, the lower velocity measurements were selected for the model boundary conditions since they corresponded more closely with the outlet location. The velocities at the area of focal vasospasm were higher in the CFD due to the constriction and matched the higher TCD velocities at this location.

TCD measurements were converted from PDF format to JPEG images, and each vessel measurement was extracted into a single gray-scale tile. An in-house automated boundary-detection algorithm in MATLAB based on pixel intensity thresholding converted the tile into a time-dependent waveform for the centerline velocity (Fig. 2.11). The resulting data were downsampled to smooth the waveform. Separate cardiac cycles were averaged together, and the standard deviation between the cycles was calculated to represent the intercycle variability. A Fourier transform with 15 modes reconstructed the waveform to ensure periodicity of the cycle. The waveforms were synchronized in time by matching the end diastolic velocities corresponding to the minima between the waveforms.

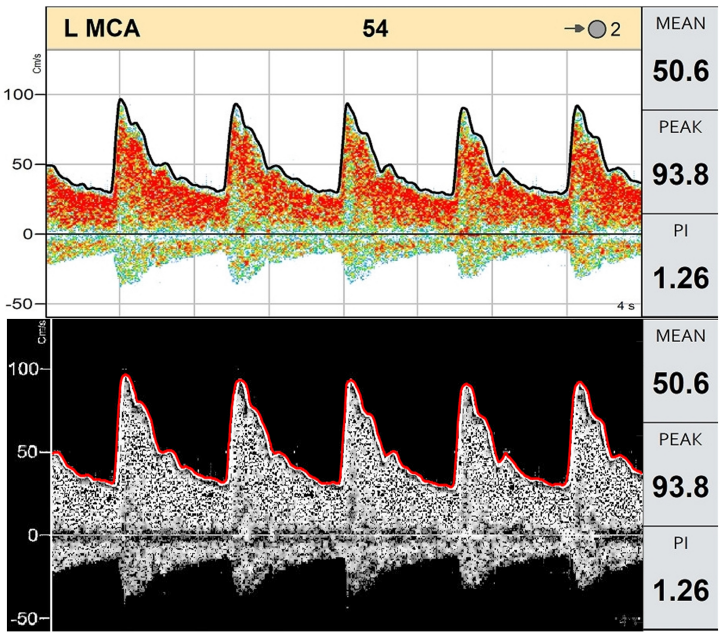

Figure 2.11: Transcranial Doppler ultrasound measurement of velocities in the left middle cerebral artery (top) converted to a tile with higher contrast between the measurement and the background used by the automated tracing algorithm (bottom)

2.2.5 Bayesian Analysis

Due to the pixelation of the CTA scans and the intercycle variability in the TCD waveforms, a degree of uncertainty was associated with the diameters and average velocities that defined the boundary conditions in the model. In total, there were 18 model parameters: nine diameters measured from the CTA scan and nine average velocities associated with TCD measurements of the BAS, ICAs, MCAs, ACAs, and PCAs. Using Bayesian analysis, this study combined the knowledge of uncertainties in the clinical measurements with the application of mass conservation to find an optimized set of parameters for the CFD simulation. Performing the Bayesian analysis involved three steps: defining the priors, determining the likelihood, and maximizing the posterior.

Priors accounted for the uncertainty in the original set of parameters. The prior for each parameter was defined with a Gaussian distribution of probability, where the mean value was the initial parameter measurement and the standard deviation was the uncertainty in the parameter. The uncertainties for the diameters and velocities were defined as half of the CTA pixel size and the intercycle variability in the TCD waveform, respectively. The priors for the nine diameters and nine average velocities were multiplied together. The likelihood was the probability that a given parameter set generated a realistic outcome. In this model, mass conservation must be satisfied for a given set of diameters and velocities. The sum of the flow rates through the inlets (the ICAs and BAS) should match exactly the sum of flow rates through the outlets (the MCAs, ACAs, PCAs, OAs, and SCAs), as seen in Eqn. 2.1.

$$\sum Q_{ICAs} + Q_{BAS} - Q_{MCAs} - Q_{ACAs} - Q_{PCAs} = Q_{OAs} + Q_{SCAs} \tag{2.1}$$

Given the low Womersley number of about two for most boundaries, the velocity profile was approximated with the parabolic Poiseuille solution. Assuming a circular blood vessel, the flow rates through the ICAs, BAS, MCAs, ACAs, and PCAs were

calculated from their diameters and average velocities with Eqn. 2.2, where Q is the volumetric flow rate, A is the area of the blood vessel, V_{ave} is the spatially and temporally averaged velocity, d is the diameter of the blood vessel, and $V_{centerline}$ is the temporally averaged centerline velocity.

$$Q = AV_{ave} = \pi\left(\frac{d}{2}\right)^2\left(\frac{V_{centerline}}{2}\right) \tag{2.2}$$

The flow rates of one OA and one SCA should be about 10 mL/ min [10] and 20 mL/min [119] respectively. Therefore, the right side of Eqn. 2.2 should evaluate to about 60 mL/min. An additional requirement of the secondary flow rates is that they remain positive over the cardiac cycle, representing antegrade flow. The likelihood function was prescribed with a Gaussian distribution where the mean value was the target flow rate, and the standard deviation was 10 mL/min; the selection of the standard deviation is described in more detail in section 2.2.6.

The posterior was obtained by multiplying the priors and the likelihood together. Figure 2.12 shows an example of a two-dimensional Bayesian analysis, which is a simplified version of the 18-parameter model used in this study. Maximizing the posterior identifies the parameter set that is both similar to the initial set and that satisfies mass conservation.

An in-house script coded in MATLAB (Mathworks, Natick, MA) applied an iterative method that maximized the posterior. At the first iteration, each of the parameters can either increase or decrease by 10% of the standard deviation (the measurement uncertainty) from the initial measurement of the diameter or velocity. Given two possibilities across 18 parameters, a subspace of 324 parameter combinations can be explored. The corresponding values of each prior given the increase or decrease in parameter value are calculated. The product of the priors and the likelihood for each of these parameter combinations are calculated. The posterior is calculated by multiplying the product of the priors and likelihood for the subspace. The maximum value is obtained, and the associated parameter combination for this

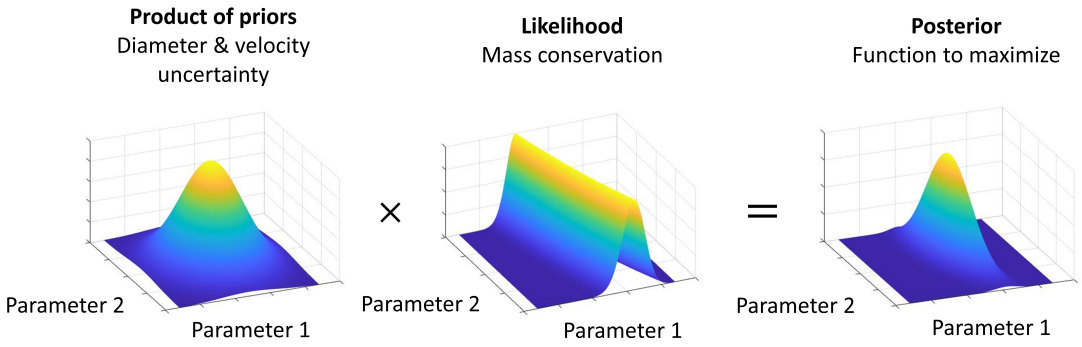

Figure 2.12: A two-dimensional illustration of the prior, likelihood and posterior for the Bayesian analysis

maximum is identified.

At the second iteration, the parameter values increase or decrease by 10% of the standard deviation from the optimal parameter combination identified in the first iteration. This process of creating subspaces and maximizing the posterior is continued until the percent change in the posterior between iterations is 5%. At this point, to ensure convergence to a single parameter combination, the subspaces are created using a 0.1% increase or decrease of the standard deviation from the previous parameter combination. The method is considered converged when the percent change in the posterior between sequential iterations is below 0.1%.

Once the optimal parameter combination was obtained, the centerline velocities from the TCD waveforms were scaled to match the optimized average velocities, and the optimized diameters were applied in the final segmentation.

2.2.6 Hyperparameter Study

The standard deviations to the priors and likelihood had to be defined to perform Bayesian analysis to optimize the input parameters. The initial measurements of the diameters and velocities at the three inlets and six primary outlets defined the mean

values of the Gaussian distributions for the priors. The mean value of the likelihood distribution was the target secondary flow rate. The standard deviations of the prior distributions for diameters and velocities were clearly quantifiable as half of the pixel size in the CTA, i.e., about 0.2 mm, and the intercycle variability in the TCD velocity measurements, respectively. However, the choice of the standard deviation for the likelihood distribution was less easily quantified based on the model parameters. The standard deviation for the likelihood can be considered a hyperparameter in this study. To justify the selection of 10 mL/min for the standard deviation of the likelihood, a hyperparameter study was performed.

Defining the Gaussian distributions for the priors required defining the mean values and standard deviations. The mean values of the priors represent the initial measurements of the nine diameters in the CTA and nine velocities from the TCD: $\mu_1, \mu_2, ..., \mu_{18}$. The Bayesian analysis identifies nine optimized diameters and nine optimized velocities: $p_1, p_2, ..., p_{18}$. To define the magnitude of the changes in the diameters and velocities from their original values due to the Bayesian analysis, the "prior norm" is defined with Eqn. 2.3.

$$prior\ norm = \sqrt{\sum_{i=1}^{18} \left(\frac{p_i - \mu_i}{\mu_i} \right)^2} \tag{2.3}$$

The target value of the secondary flow rate represents the mean value of the likelihood distribution: Q_{target}. After the Bayesian analysis is performed, the final secondary flow rate is identified: Q_{final}. To define the magnitude of the difference between the target flow rate and the final secondary flow rate, the "likelihood norm" is defined with Eqn.2.4:

$$likelihood\ norm = \left| \frac{Q_{final} - Q_{target}}{Q_{target}} \right| \tag{2.4}$$

The hyperparameter – the standard deviation of the likelihood – was varied from 1 to 100 mL/min. With a low value for the hyperparameter, the Gaussian distribution

for the likelihood is narrower, which favors matching the final secondary flow rate more closely to the target flow rate (a smaller secondary flow norm) at the expense of large changes in the diameters and velocities from their initial measurements (a larger prior norm). With a high value for the hyperparameter, the Gaussian distribution for the likelihood is wider, which favors smaller deviations of the optimized diameters and velocities from their initial measurements (a smaller prior norm) at the expense of larger deviations of the final secondary flow rate compared to the target secondary flow rate (a larger secondary flow norm).

The hyperparameter study was performed for two cases:

- Case 1: The secondary flow rate before the Bayesian analysis is lower than the target flow rate (large negative value).

- Case 2: The secondary flow rate before the Bayesian analysis exceeds the target flow rate (large positive value).

Figure 2.13 plots the prior norm versus the likelihood norm for all values of the hyperparameter for case 1, with the red datapoint representing the final hyperparameter selected for the study. By increasing the hyperparameter, the prior norm decreases and the likelihood norm increases (Fig. 2.13, top), which corresponds to the diameters and velocities undergoing smaller changes from their original values and the secondary flow rate deviating further from the target value. Plotting a subset of the data with the same x- and y-limits (Fig. 2.13, bottom), it becomes apparent that increasing the hyperparameter causes larger increases in the likelihood norm than decreases in the prior norm, suggesting that using a large hyperparameter is not beneficial for reducing changes imposed by the Bayesian analysis on the diameters and velocities. The datapoint that does not fall on the curve represents a hyperparameter that caused the iterative algorithm not to converge properly.

Figure 2.14 plots the secondary flow rate after the Bayesian analysis versus the hyperparameter for case 1, with the dashed line representing the target flow rate

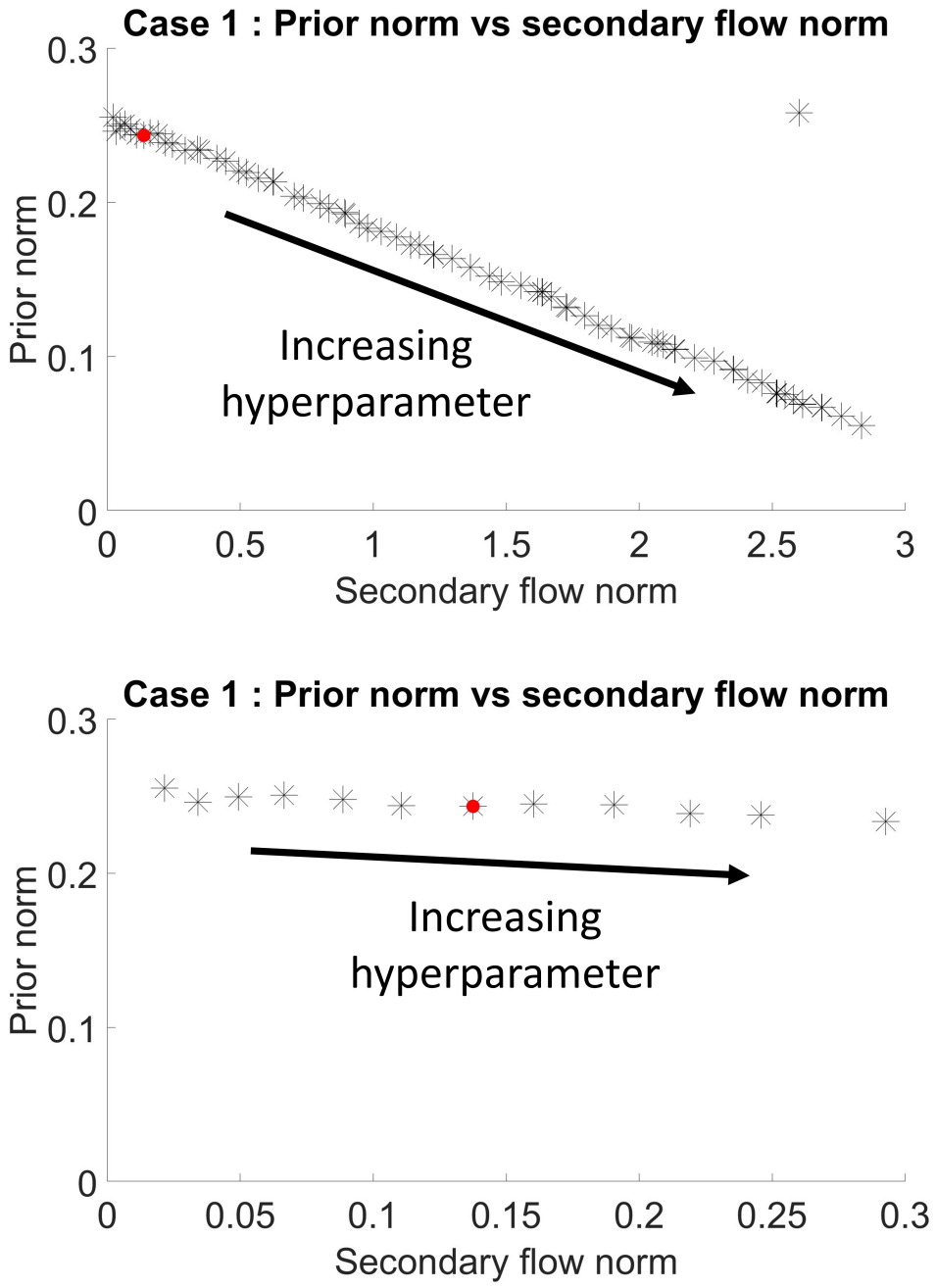

Figure 2.13: Case 1 prior norm versus secondary norm for the entire set of hyperparameters (top) and for a subset of hyperparameters on axes with equal limits (bottom), with the red data point representing the final hyperparameter selected for the study

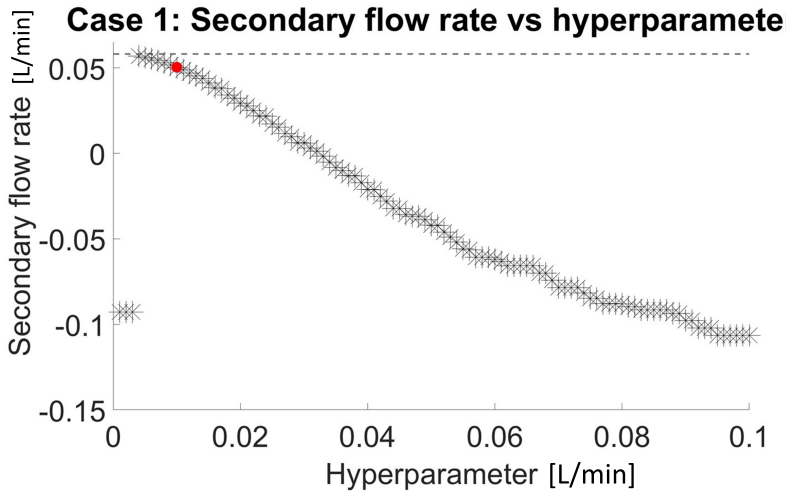

Figure 2.14: Case 1 secondary flow rate after the Bayesian analysis versus the hyperparameter, with the dashed line representing the target flow rate and the red datapoint representing the final hyperparameter selected for this study

and the red datapoint representing the final hyperparameter selected for this study. For very low values of the hyperparameter, the iterative algorithm fails and returns errant values of the final secondary flow rate. As the hyperparameter increases, the final secondary flow rate decreases, eventually approaching negative values. Negative values of secondary flow rate represent reverse flow in the OAs and SCAs, which is unphysiological. Therefore, the average secondary flow rate should be positive. Additionally, the secondary flow rate changes over time, so the minimum flow rate can be much lower than the average flow rate. The hyperparameter of 10 mL/min ensures that the flow is antegrade at all times while avoiding divergence of the iterative algorithm.

Figure 2.15 plots the prior norm versus the likelihood norm for all values of the hyperparameter for case 2, with the red datapoint representing the final hyperparameter selected for the study. The same trends seen in case 1 apply to case 2; increasing

the hyperparameter increases the likelihood norm more significantly than decreasing the prior norm (Fig. 2.15, bottom).

Figure 2.16 plots the secondary flow rate after the Bayesian analysis versus the hyperparameter for case 2, with the dashed line representing the target flow rate and the red datapoint representing the final hyperparameter selected for this study. Similar to case 1, the lowest values of the hyperparameter result in errant values of secondary flow rate due to the failure of the iterative algorithm. Increasing the hyperparameter increases the final secondary flow rate. Large values of secondary flow rate result in unphysiologically high velocities in the SCAs and OAs, so the chosen hyperparameter of 10 mL/min ensures that the iterative algorithm is successful while avoiding unrealistically high velocities.

2.2.7 Benchmarking Diameters, Velocities, and Flow Rates

The diameters [47, 53, 59, 74, 75, 83, 95, 117, 129, 155], velocities [3, 62, 67, 101], and flow rates [11, 25, 51, 66, 96, 118, 136, 145, 158, 171, 174, 175] from studies of healthy patients were compared with the simulation values. Literature measurements of flow rate in the smaller vessels, such as the ACAs, are likely less accurate than those in larger vessels, such as the ICAs, due to the relatively large voxel size in the phase-contrast magnetic resonance imaging measurements compared with the small vessel diameters [171]. For patients with a fetal PCA, the flow rates corresponding to this variation for the ICA and BAS were plotted [66, 158, 174].

2.2.8 Finalized Geometry and Mesh

In SimVascular, the final optimized diameters from the Bayesian analysis were applied at the inlets and outlets. A three-dimensional surface representation was created by lofting circular contours along centerlines. Flow extensions were added to the ICAs (8 mm), BAS (4 mm), MCAs (4 mm), ACAs (4 mm), PCAs (4 mm), OAs

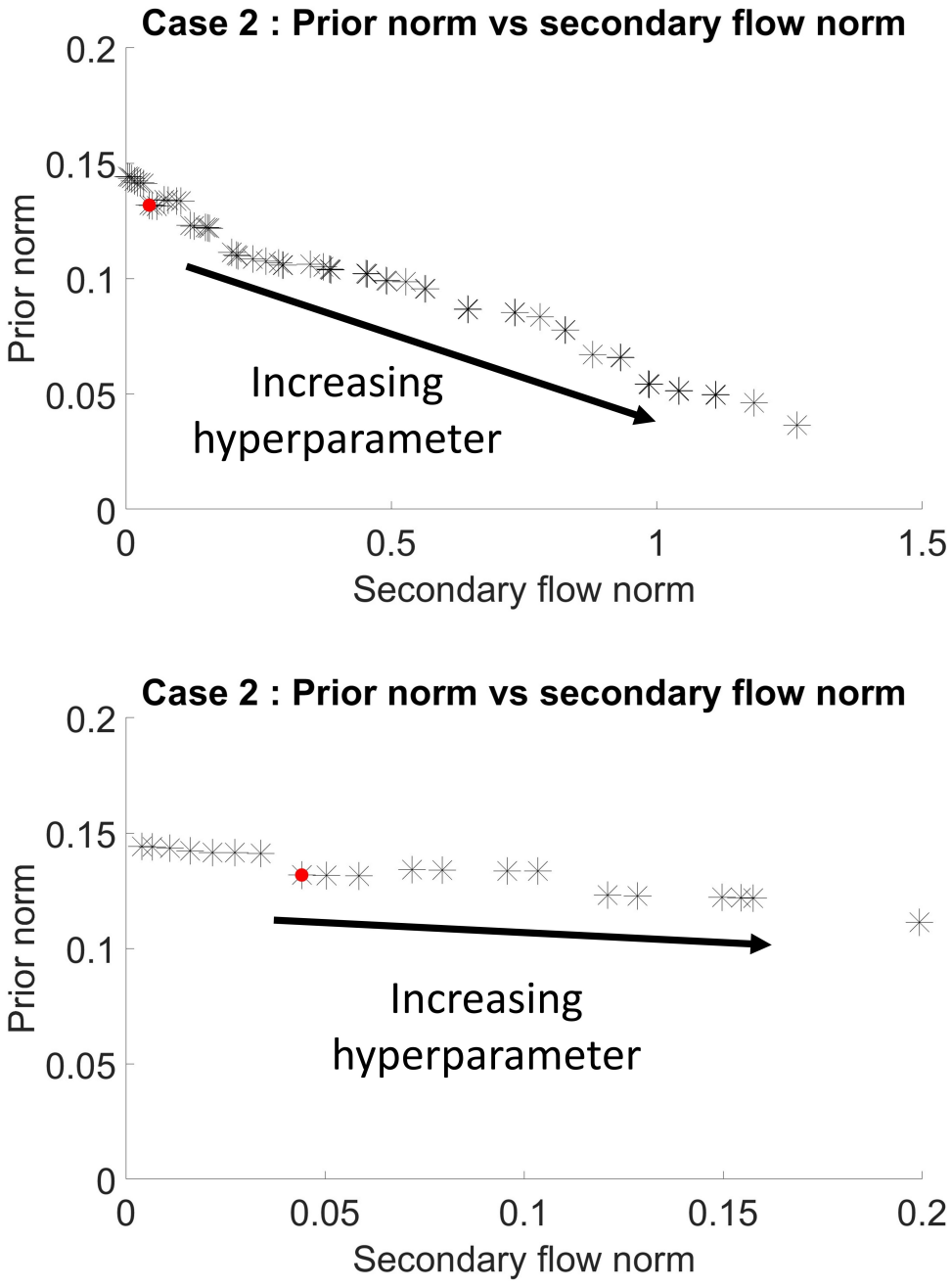

Figure 2.15: Case 2 prior norm versus secondary norm for the entire set of hyperparameters (top) and for a subset of hyperparameters on axes with equal limits (bottom), with the red data point representing the final hyperparameter selected for the study

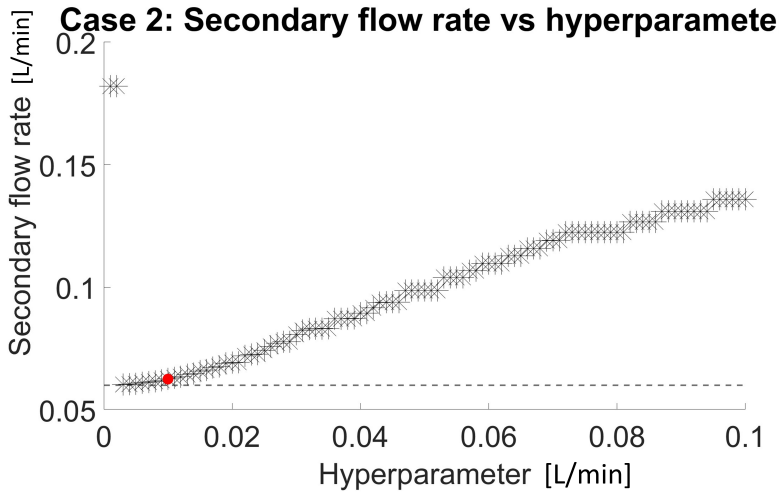

Figure 2.16: Case 2 secondary flow rate after the Bayesian analysis versus the hyperparameter, with the dashed line representing the target flow rate and the red datapoint representing the final hyperparameter selected for this study

(1 mm), SCAs (1 mm) and, if present, the duplicate PCA (1 mm) using the open-source tool Vascular Modeling ToolKit (www.vmtk.org). The finalized surface mesh was converted to a volumetric mesh in STARCCM+ version 12.06 (Siemens, Munich, Germany) consisting of tetrahedral elements (base size = 0.55 mm, surface size = 0.44 mm) and four boundary layer elements. The final meshes consisted of about 4 million elements. A grid resolution study was performed by comparing the average flow rates and maximum velocities in the collateral vessels between the meshes. These metrics for the final mesh exhibited less than a 5% error with the finest mesh comprising about 22 million elements. The mesh study based on the hemodynamic metrics of resistance and viscous dissipation is described in section 2.2.16.

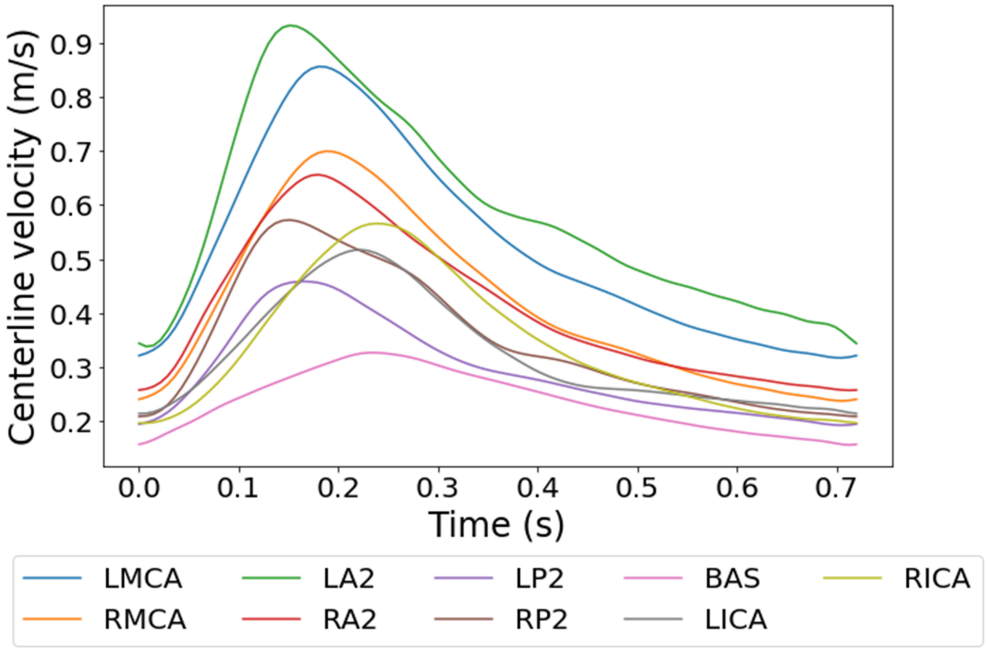

Figure 2.17: Centerline velocities over time in the bilateral anterior, middle, posterior, and internal carotid arteries and basilar artery

2.2.9 Patient-Specific, Image-Based Boundary Conditions for CFD

TCD measurements of the centerline velocity were scaled by the factors determined in the Bayesian analysis. The time-varying centerline velocity profiles at the three inlets (the ICAs and BAS) and six outlets (MCAs, ACAs, and PCAs), as seen in Fig. 2.17, can be represented with a Fourier expansion in Eqn. 2.5, where A are the Fourier modes and ω is the frequency.

$$U_{centerline} = A(\omega)e^{i\omega t} \tag{2.5}$$

A time-varying velocity profile in a straight tube can be represented analytically using a Womersley profile [169], calculated with Eqn. 2.6, where $\tilde{A}_n$ are the scaled Fourier coefficients, r is the radial location on the inlet or outlet surface, R is the

vessel radius, and J_0 is the 0th-order Bessel function of the first kind.

$$w(r,t) = A_0\left(1 - \left(\frac{r}{R}\right)^2\right) + \sum_{n=1}^{N} \tilde{A}_n \left[1 - \frac{J_0(\frac{r}{R} \cdot i^{3/2} \cdot Wo_n)}{J_0(i^{3/2})}\right] e^{i\omega_n t} \tag{2.6}$$

The Womersley number for the n^{th} mode is calculated with Eqn. 2.7, where T is the period of the cardiac cycle, R is the vessel radius, and ν is the kinematic viscosity.

$$Wo_n = R\sqrt{\frac{2\pi n}{T\nu}} \tag{2.7}$$

The scaled Fourier coefficients $\tilde{A}_n$ are defined with Eqn. 2.8.

$$\tilde{A}_n = 2A_n / \left[1 - \frac{1}{J_0(i^{3/2} Wo_n)}\right] \tag{2.8}$$

The OAs were prescribed with a Womersley profile that generated a net flow rate between 10 and 15 mL/ min. The SCAs were prescribed with resistance boundary conditions. The flow should be evenly split between the left and right sides in the SCAs (about 20–25 mL/min per side). A CFD simulation was computed with initial estimates of resistance that result in the target flow rates. If the flow rate was higher than the expected value in a vessel, the resistance was increased. The CFD simulations were rerun until all resistances were tuned to generate the target flow rates.

2.2.10 Computational Fluid Dynamics Simulations

The incompressible Navier–Stokes and continuity equations were solved using ANSYS FLUENT 18.0 (Ansys, Canonsburg, PA), a finite volume pressure-based solver. With a Reynolds number of about 600, the flow is the laminar regime.

Blood was modeled as a Newtonian fluid with a density of 1050 kg/m^3 and a viscosity of 0.0035 $Pa \cdot s$. The vessel walls were modeled as rigid.

The time-step selected was 0.001 seconds with cardiac cycles varying between 0.51-1.1 seconds across the cohort. These periods were calculated by averaging the periods of the nine TCD waveforms for each patient and clinical condition. The residuals were

set to $1x10^{-4}$ for mass conservation and $1x10^{-6}$ for the three components of velocity. The pressure-implicit with splitting of operators pressure–velocity coupling scheme, with second-order pressure and momentum spatial discretization and second-order implicit time discretization, was employed.

The CFD simulations were computed on four nodes of Hyak— the University of Washington distributed memory massively parallel computing platform—with 28 processor dual Intel Xeon CPUs – for simulation times of about 10 h. The simulations were run for two cardiac cycles to eliminate transient behavior associated with initialization, and the results were analyzed for the third cardiac cycle.

The collateral flow rates were measured over time by creating cross-sectional planes in the bilateral A1s, P1s, Pcoms, and Acom.

2.2.11 Virtual Angiography

Cebral et al. demonstrated that a virtual angiogram can be performed by solving the advection-diffusion equation [29], which allows the CFD model to be compared to DSA. Virtual angiograms were performed by injecting a passive scalar into the BAS and the ICAs. An advection–diffusion equation was solved to model the transport of radiopaque contrast as seen in Eqn. 2.9.

$$\frac{\partial c}{\partial t} + \vec{u} \cdot \nabla c = D\nabla^2 c \tag{2.9}$$

This equation was represented in Fluent with the temperature/chemical species analogy in the energy equation. Typical values for the diffusivity of a high molecular weight soluble species in a liquid are on the order of 10^{-8} - 10^{-10}. The Peclet number represents the relative importance the advective vs diffusive terms and is calculated with Eqn. 2.10 where U is the characteristic velocity, L is the characteristic length scale, and D is the diffusivity.

$$Pe = \frac{UL}{D} \tag{2.10}$$

Due to the low diffusivity and relatively high velocities, the Peclet number was 10^5-10^7, and the contrast agent transport was dominated by advection. The simulations were run with an equivalent thermal diffusivity corresponding to a Peclet number of 100, thus capturing the dominance of convection over diffusion in the transport, without relying on inconsistent numerical discretizations for the very high Peclet number flow. The inlet and outlet temperatures were defined by arbitrary values (350 K and 300 K), corresponding to 100% and 0% concentration of radio-opaque contrast agent, respectively. The boundary condition for the vessel walls was no flux of contrast through them.

The intensity of the contrast indicated the magnitude of the flow through the vessel, with lighter regions indicating limited flow.

2.2.12 Sensitivity Analysis

Some uncertainties in the measurements of the diameters and velocities in the primary inlets and outlets are easily quantified, such as the CTA pixel size and intercycle variability in the TCD measurement. However, other uncertainties in the input parameters, such as a nonzero Doppler angle in the collection of the TCD velocities and the determination of the correct measurement location of the vessel diameter during segmentation, cannot be easily quantified. A sensitivity analysis can determine how all types of uncertainty simultaneously propagate into uncertainties in the collateral flow rates.

The collateral flow rates were estimated by solving a linear system of equations representing mass conservation at each bifurcation in the CoW. For a complete CoW anatomy, there are seven bifurcations and seven unknown collateral flow rates. However, the solution is not unique. Therefore, a Moore–Penrose pseudo-inverse was

used to solve the system of equations. For patients missing a segment in the CoW, the number of equations exceeded the number of unknowns, creating an overdefined system solved with a least-squares approximation.

One thousand different combinations of initial diameters and mean velocities that could vary up to 10% from their optimal values were introduced into the network. Bayesian analysis was performed on each initial parameter set to generate a final parameter set that satisfies mass conservation. The collateral flow rates associated with the final parameter set were computed by solving the linear system of equations. The resulting changes in the collateral flow rates were represented using violin plots. The collateral flow rates corresponding to the optimized parameter set were associated with the maximum width of the violin. Positive values of collateral flow rate corresponded to the following directions: left to right in the Acom, A1 to A2 in the ACA, anterior to posterior in the Pcom, and P1 to P2 in the PCA.

2.2.13 Hemodynamic Metrics of Vasospasm Severity

The determination of severity of vasospasm from angiography is relatively qualitative, often with the degree of stenosis representing the severity. To understand mechanistically and in a quantitative sense the degree of severity, two metrics are proposed: resistance and viscous dissipation.

2.2.14 Resistance

The resistance of a vessel segment represents the pressure drop required to pump a certain flow rate through the segment, calculated with:

$$R = \frac{p_1 - p_2}{Q} \tag{2.11}$$

where R is the resistance, $p_1 - p_2$ is the pressure difference between the beginning and end of the vessel segment, and Q is the instantaneous flow rate (Fig. 2.18).

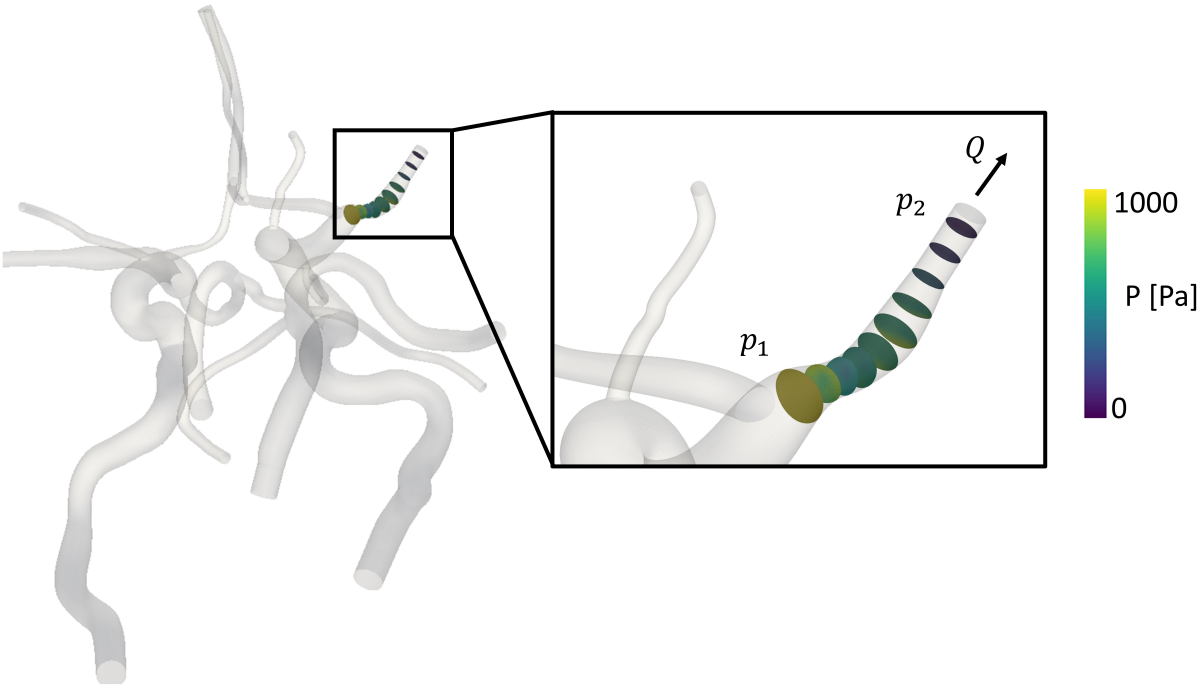

Figure 2.18: Pressure slices through a right middle cerebral artery for calculating resistance

The pressure drop in a vessel is expected to increase with decreasing diameter. Given similar flow rates in a vessel segment between baseline and vasospasm, higher pressure drop in a vasospastic vessel is expected to result in higher resistance.

The resistance was calculated in the bilateral terminal ICA (TICA), MCA, ACA A1, ACA A2, PCA P1, and PCA P2 segments. The terminal ICA was defined as the segment between the intersection of the ICA with the OA and the bifurcation into the MCA and ACA A1.

The centerlines of the vasculature were extracted from the final segmented vasculature in SimVascular and exported in PolyData format. Centerlines for each individual segment were isolated using an in-house Python code, with the beginning and ending points avoiding bifurcations in the CoW and vessel tips. Using the PyTec link between Python and Tecplot (Tecplot, Inc. Bellevue, WA), slices at the beginning and end of the vessel were created, and the pressure was averaged across the slice. The pressure drop was determined in each vessel segment from the fields computed at different times during the cardiac cycle and divided by the instantaneous flow rate to calculate the resistance. The time-averaged resistance was calculated by averaging the instantaneous resistances over the entire cardiac cycle.

When the flow rate approaches zero, as in a vessel with biphasic flow, the instantaneous resistance can be arbitrarily large and skew the value of the mean resistance. If the instantaneous resistance was five times the median instantaneous resistance, this resistance was excluded in the calculation of the mean instantaneous resistance.

The percent change in resistance ($R_{\%change}$) between baseline and vasospasm was calculated with

$$R_{\%change} = \left(\frac{R_{vasospasm} - R_{baseline}}{R_{baseline}} \right) 100\% \tag{2.12}$$

where $R_{baseline}$ and $R_{vasospasm}$ are the average resistances in a vessel segment during baseline and vasospasm, respectively. An increase in resistance was expected in vasospastic vessels.

2.2.15 Viscous Dissipation

Viscous dissipation quantifies the energy to overcome viscous forces in a fluid in motion. The amount of energy lost in a vasospastic vessel is expected to be higher than in a normal vessel due to restriction of the vessel caliber and increased velocity gradients.

Viscous dissipation quantifies the energy required to overcome viscous forces in a fluid in motion. The amount of energy lost in a vasospastic vessel is expected to be higher than in a normal vessel due to restriction of the vessel caliber and increased velocity gradients.

The velocity gradient tensor $\nabla\vec{u}$, which represents spatial gradients in velocity, is defined using the three components of velocity (u, v, w) and three spatial dimensions (x, y, z) with:

$$\nabla\vec{u} = \begin{bmatrix} \frac{\partial u}{\partial x} & \frac{\partial v}{\partial x} & \frac{\partial w}{\partial x} \\ \frac{\partial u}{\partial y} & \frac{\partial v}{\partial y} & \frac{\partial w}{\partial y} \\ \frac{\partial u}{\partial z} & \frac{\partial v}{\partial z} & \frac{\partial w}{\partial z} \end{bmatrix} \tag{2.13}$$

The viscous stress tensor τ can be written in terms of the velocity gradient in a fluid element as:

$$\tau = \mu(\nabla\vec{u} + \nabla\vec{u}^T) \tag{2.14}$$

where μ is the dynamic viscosity of blood.

The viscous dissipation at each point within a vessel segment Φ_{local} is evaluated with:

$$\Phi_{local} = \tau : \vec{u} \tag{2.15}$$

Pointwise viscous dissipation was evaluated in Tecplot at each cell in the CoW and exported in ASCII format. The CoW was divided into subdomains for each segment

in Python (Fig. 2.19). The pointwise viscous dissipation was integrated within each segment and normalized by the segment volume:

$$\Phi = \frac{\int_{dV} \Phi_{local} dV}{\int_{dV} dV} \tag{2.16}$$

The time-averaged dissipation was calculated by averaging instantaneous viscous dissipation over the cardiac cycle.

The percent change in time-averaged viscous dissipation $\Phi_{\%change}$ was calculated with:

$$\Phi_{\%change} = \left(\frac{\Phi_{vasospasm} - \Phi_{baseline}}{\Phi_{baseline}} \right) 100 \tag{2.17}$$

where $\Phi_{baseline}$ and $\Phi_{vasospasm}$ are the viscous dissipation during baseline and vasospasm, respectively. The term "dissipation" is used henceforth to describe changes in viscous dissipation.

2.2.16 Mesh Independence Study

The mesh independence study was performed by comparing the percent changes in resistance and dissipation between the baseline and vasospasm conditions across four mesh resolutions: a base size of 0.6 mm (3.5 million elements during baseline and 2.8 million elements during vasospasm), 0.35 mm (4.4 million elements during baseline and vasospasm), 0.2 mm (13 million elements during baseline and 10.5 million elements during vasospasm), and 0.15 mm (33 million elements during baseline and 22 million elements during vasospasm). The percent changes in resistance and dissipation were compared between each of the meshes. The differences in percent change in resistance between the coarsest and finest meshes were below 15 in vessels exhibiting an absolute change below 1000%, below 100 in vessels with an absolute change between 1000% and 1200%, and below 500 for one vessel with greater than 3000% absolute change. The differences in percent change in dissipation between the coars-

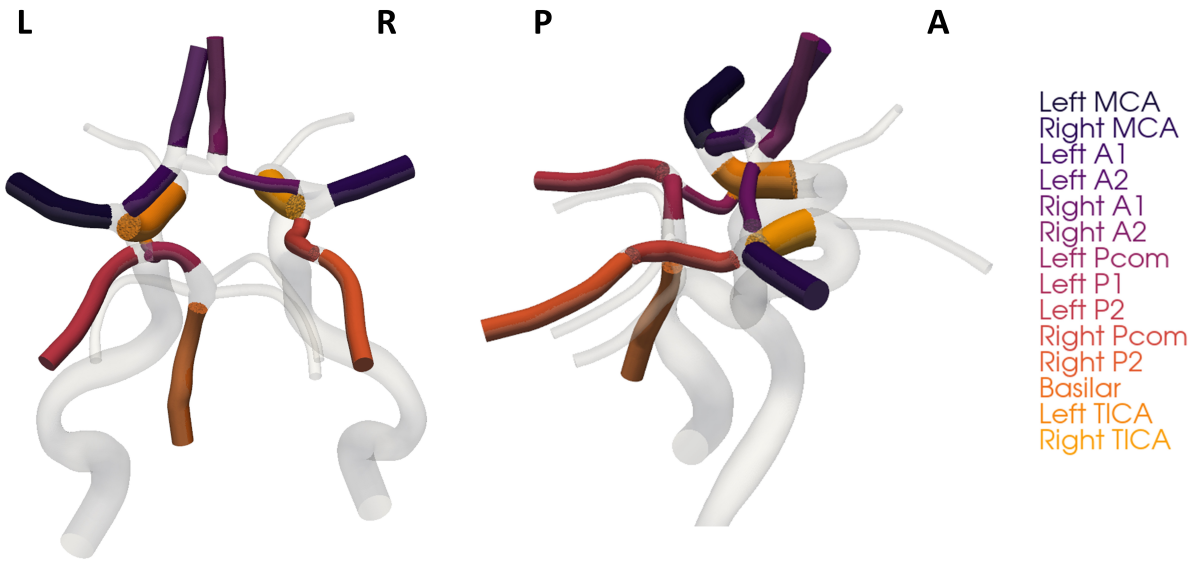

Figure 2.19: Vessel zones used for integrating viscous dissipation in the left-right view (left) and anterior-posterior view (right)

est and finest meshes were below 50 in vessels exhibiting an absolute change below 800%, below 100 in vessels with an absolute change between 800% and 2000%, and below 100 for vessels with greater than 2000% absolute change. Given the relatively small differences between the percent changes in resistance and dissipation compared to their absolute values, the CFD results were considered to be insensitive to mesh resolution in the range of base sizes between 0.6 mm and 0.15 mm.

The base size of 0.55 mm was selected because the previous mesh study described in section 2.2.16 showed that the collateral flow rates were consistent between this sizing and the finer meshes.

2.2.17 Discretizing CFD Metrics to Compare with Angiographic Severity

In order to compare the CFD results to the angiographic severity, the continuum of values for percent changes in resistance and dissipation were discretized into four categories. A threshold value was selected to define the four categories, e.g., a threshold value of 2000% change would result in the categories 0-500% associated with none, 500-1000% associated with mild, 1000-1500% associated with moderate, and over 1500% associated with severe. The threshold values were varied from 100 to 5000, and the associated CFD severity was assigned as 0, 1, 2, or 3 given the categories of none, mild, moderate, or severe vasospasm, respectively. The angiographic severity was also assigned with 0, 1, 2, and 3 for the respective severities. The error ϵ between the CFD categorizations and angiographic categorizations of vasospasm was evaluated as the root-mean square of the differences between the angiography severity $s_{angiography}$ and CFD severity, quantized from the percent changes in resistance or dissipation $s_{CFDmetric}$:

$$\epsilon = \sqrt{\sum (s_{angiography} - s_{CFDmetric})^2} \tag{2.18}$$

where the sum is performed on all vessels with angiographic severity assigned to

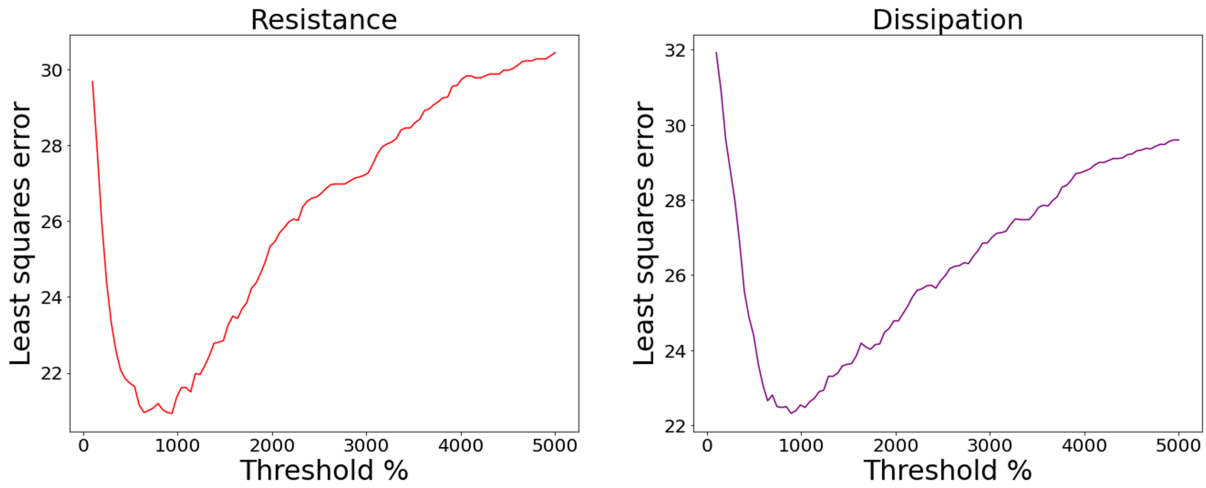

Figure 2.20: Least squares error between the quantized CFD metrics and angiographic severity given a range of thresholds for resistance (left) and dissipation (right)

them across the entire cohort of 25 patients.

In the following sections, all results are presented for a threshold of 1000% which minimized error for both the resistance and dissipation metrics in comparison with the angiographic severity (Fig. 2.20). This threshold results in four categories: 0-250% change as "none", 250-500% change as "mild", 500-750% change as "moderate", over 750% change as "severe".

2.2.18 Identifying Localization and Overall Severity of Vasospasm

This study aimed to identify patients with vasospasm localized in a certain part of the CoW to understand if changes in collateral flow directions or development of infarct could relate to localization of vasospasm. Three zones within the CoW were defined:

left anterior, right anterior, and posterior, which are associated with major arterial inflows from the left ICA, right ICA, and BA, respectively. The percent changes in resistance or dissipation were summed across the left MCA, left ACA A1 segment, and left ACA A2 segment for the left anterior zone, and the right MCA, right ACA A1 segment, and right ACA A2 segment for the right anterior zone. The posterior zone was defined by summing the percent changes in the left and right PCA P2 segments as well as the average of the left and right PCA P1 segments to create a comparison equivalent to the anterior zones consisting of three vessels. The percent changes across the three zones were summed, and each zone was divided by the sum to identify the smallest and largest contributors of each zone to the overall severity of the vasospasm across the CoW. Vessels with over 2500% change in resistance or viscous dissipation were set to a value of 2500% to eliminate outlying values that would distort summations.

If the vasospasm was localized in one of the three zones, its percent contribution to the overall severity could be as high as 80%. If the vasospasm was balanced across all zones, the maximum contribution of a single zone would be 33% of the total severity. To identify vasospasm localized in two zones, the two zones with the highest contributions to the total severity were summed. If there were a high degree of localization in two zones, their percent contribution to the total severity could be as high as 99%. For balanced vasospasm, the sum of the two highest contributors would be 66%. The patients were sorted from high degree of localization to low degree of localization based on both the percent changes in resistance and dissipation, and representative patients were identified based on agreement in localization across both CFD metrics.

The overall severity of the vasospasm in the CoW was evaluated by summing the percent changes in resistance or dissipation across the TICAs, BAS, MCAs, ACA A1 and A2 segments, and PCA P1 and P2 segments.

Two patients with high degrees of localization in one zone and two patients with

high degrees of localization in two zones are discussed in depth in section 2.3.7. Two patients with balanced vasospasm across the three zones are discussed in depth in section 2.3.8. The remainder of the cohort is briefly presented in sections 2.3.11-2.3.14.

2.2.19 Summary of Computational Methodology

Figure 2.21 summarizes each stage of the workflow used to create the computational model: taking initial measurements of vessel diameters and velocities, leveraging Bayesian analysis and benchmarking to determine the final model parameters, applying the final parameters in the simulation, generating virtual angiograms, representing the sensitivity of collateral flow rates to uncertainties with violin plots, and measuring the percent changes in resistance and viscous dissipation.

2.3 Results

2.3.1 Representative Patients to Illustrate the Methodology

In order to illustrate hemodynamic behavior captured by the computational fluid dynamics simulations, two patients of interest will be represented in sections 2.3.2-2.3.4. Patient A has a complete CoW with two patent Pcoms (Fig. 2.22, top), and patient B is missing a right P1 segment and has a hypoplastic right A1 segment (Fig. 2.22, bottom). Patient B also has a redundant right PCA in which about 15 mL/min of flow was directed.

For both patients, the locations and severity of vasospasm as well as the direction and magnitude of the collateral flows were determined by reviewing clinical DSA with experienced neurosurgeons. Change in flow direction was defined in section 2.1.9. A supplying artery to the CoW — an ICA or BAS — was considered to be recruited if the flow rate notably increased during vasospasm compared to baseline.

Figure 2.23 is a schematic of the clinically determined collateral flow directions and

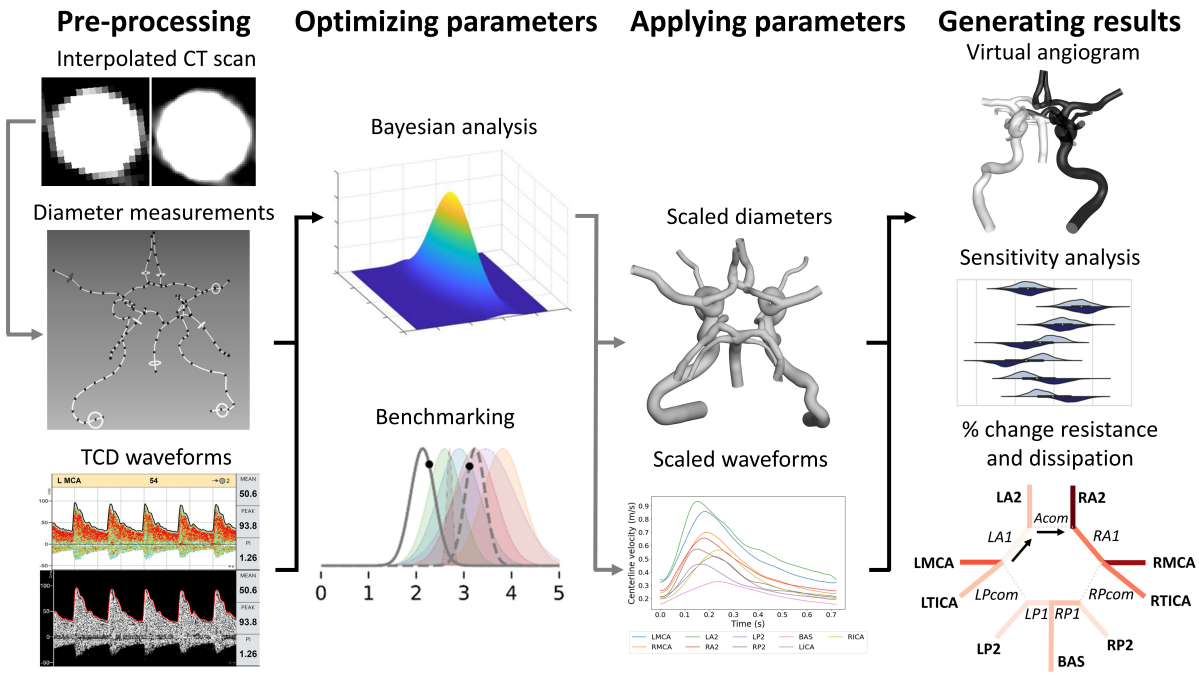

Figure 2.21: Summary of methodology for creating patient-specific CFD simulations in the Circle of Willis during vasospasm

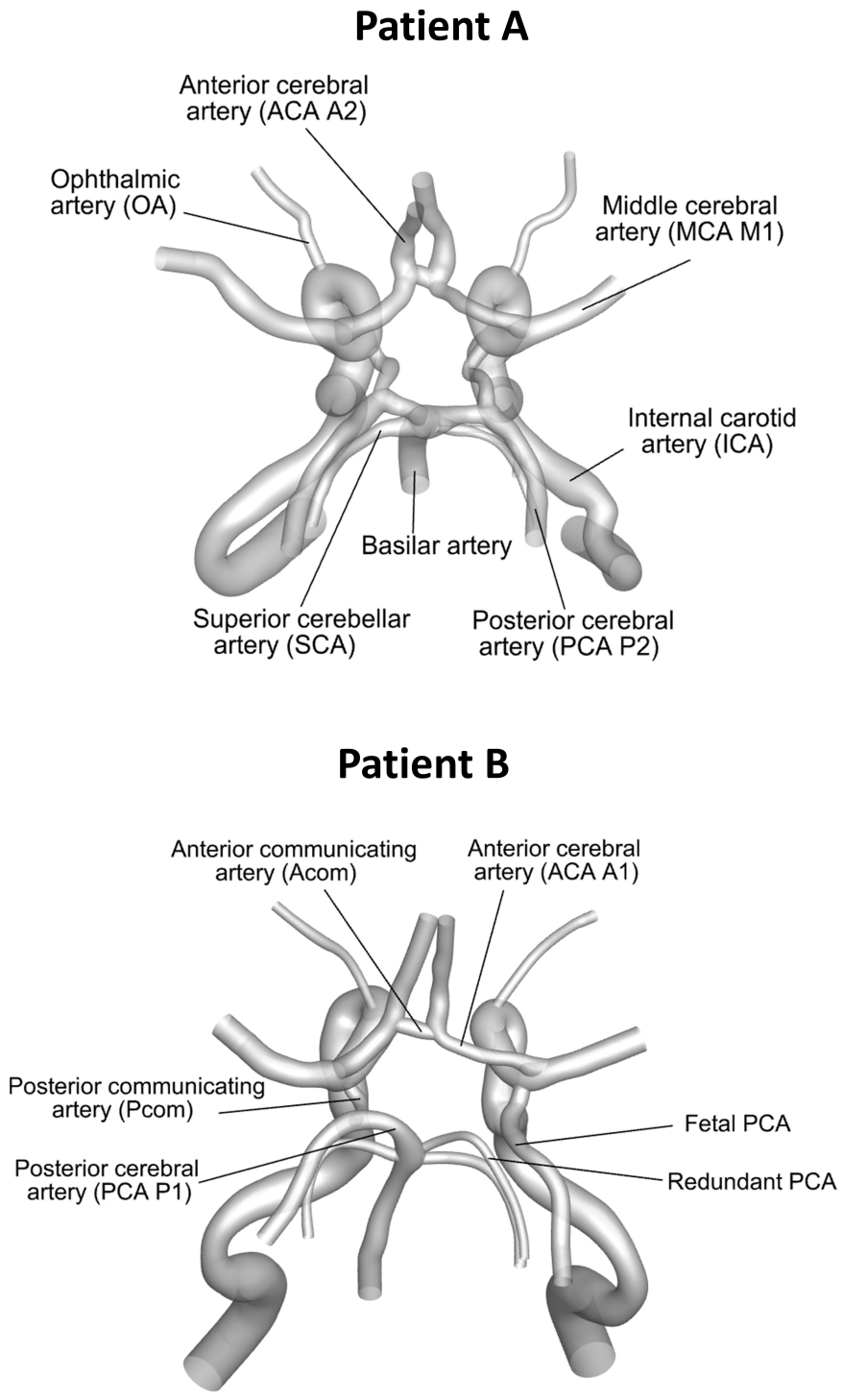

Figure 2.22: Patient A with a complete circle of Willis with labels of the major cerebral blood vessels (left) and patient B with a missing right PCA P1 segment with labels of the collateral pathways (right)

locations of vasospasm for patient A. In patient A, at baseline, the anterior circulation strongly supplied the posterior territory via the bilateral Pcoms, and there was some reverse flow in the left PCA P1 segment, i.e., flow from left to right (Fig. 2.23, top). The locations of vasospasm were localized in the anterior circulation, as shown by the valve icons (Fig. 2.23, bottom), where the lightest valve represents mild vasospasm and the darkest valve represents severe vasospasm. During vasospasm, the BAS was recruited to help supply the anterior circulation through reverse flow in both Pcoms, as shown by the large double arrows (Fig. 2.23, bottom). Additionally, the reverse flow was no longer present in the left P1 segment due to the strengthening of the flow from the BAS.

Figure 2.24 is a schematic of the clinically determined collateral flow directions and locations of vasospasm for patient B. Patient B had a fetal-type PCA on the right side. At baseline, most of the collateral pathways exhibited typical directions of flow with the exception of weak reverse flow in the left Pcom (Fig. 2.24, top). The locations of vasospasm were centralized in the MCA and ACA territories with more severe vasospasm in the right supraclinoid ICA than the left one (Fig. 2.24, bottom). During vasospasm, the left ICA was recruited, as shown by the large double arrows, to help supply the right side via bidirectional flow in the right ACA A1 segment.

2.3.2 Diameter, Velocity, and Flow Rate Benchmarking

Figures 2.25 and 2.26 plot the diameters, velocities, and flow rates for patients A and B, respectively, as described in section 2.2.7. The shaded Gaussian distributions represent the literature values, the dashed black line and solid black line represent the Bayesian priors for baseline and vasospasm, respectively, and the black point represents the optimal value used to define the CFD boundary conditions. The standard deviations of the priors were half of the CTA pixel size for the diameter and the intercycle variability for the velocity. The valve icons indicate which vessels were in vasospasm, and the bold arrow represents the main inlet artery that was recruited

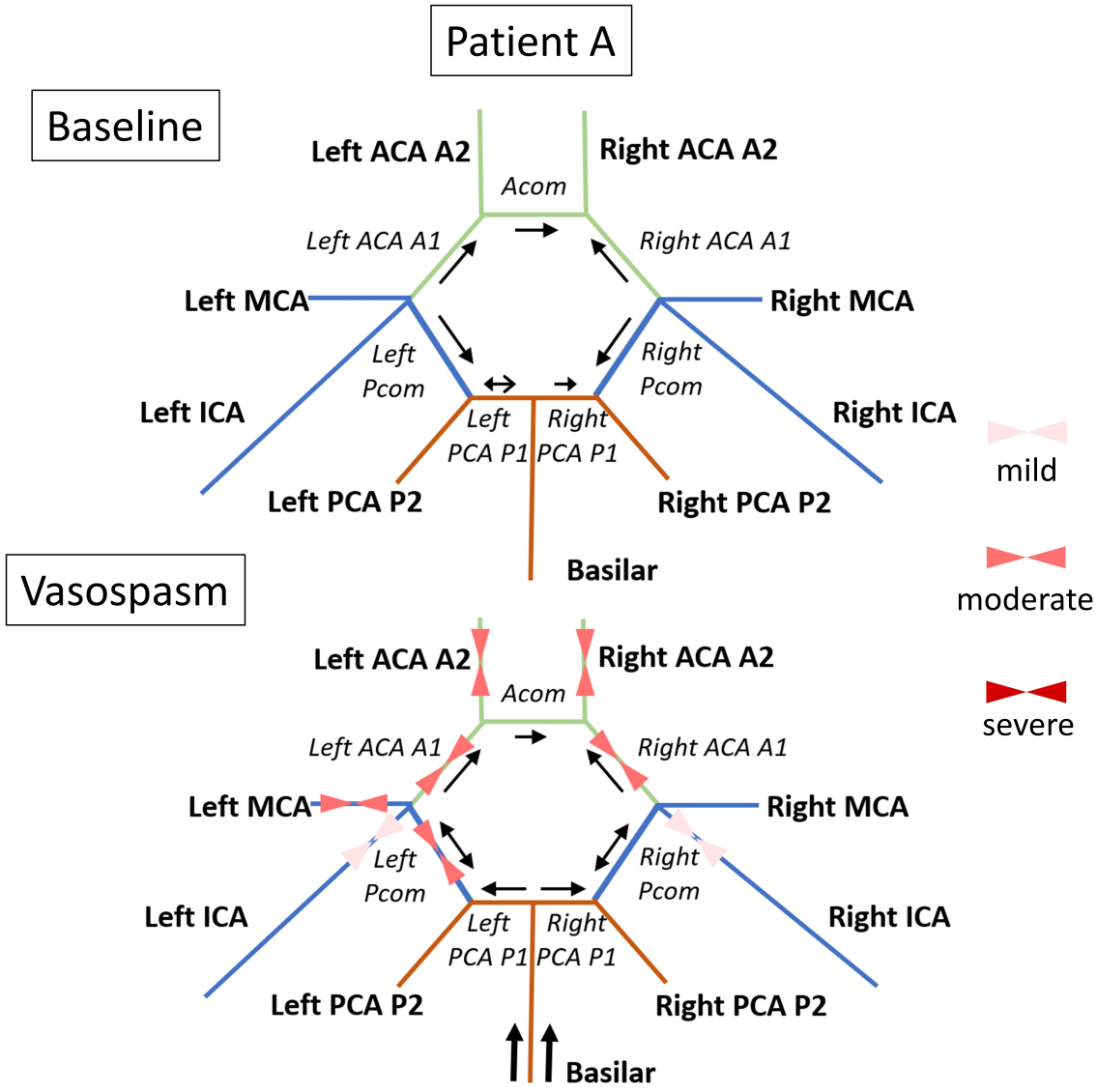

Figure 2.23: Patient A collateral flow directions during the baseline (top) and vasospasm (bottom) conditions exhibited with arrows, the primary recruited inlet artery exhibited with large double arrows, and the locations and severity of vasospasm exhibited with valve icons

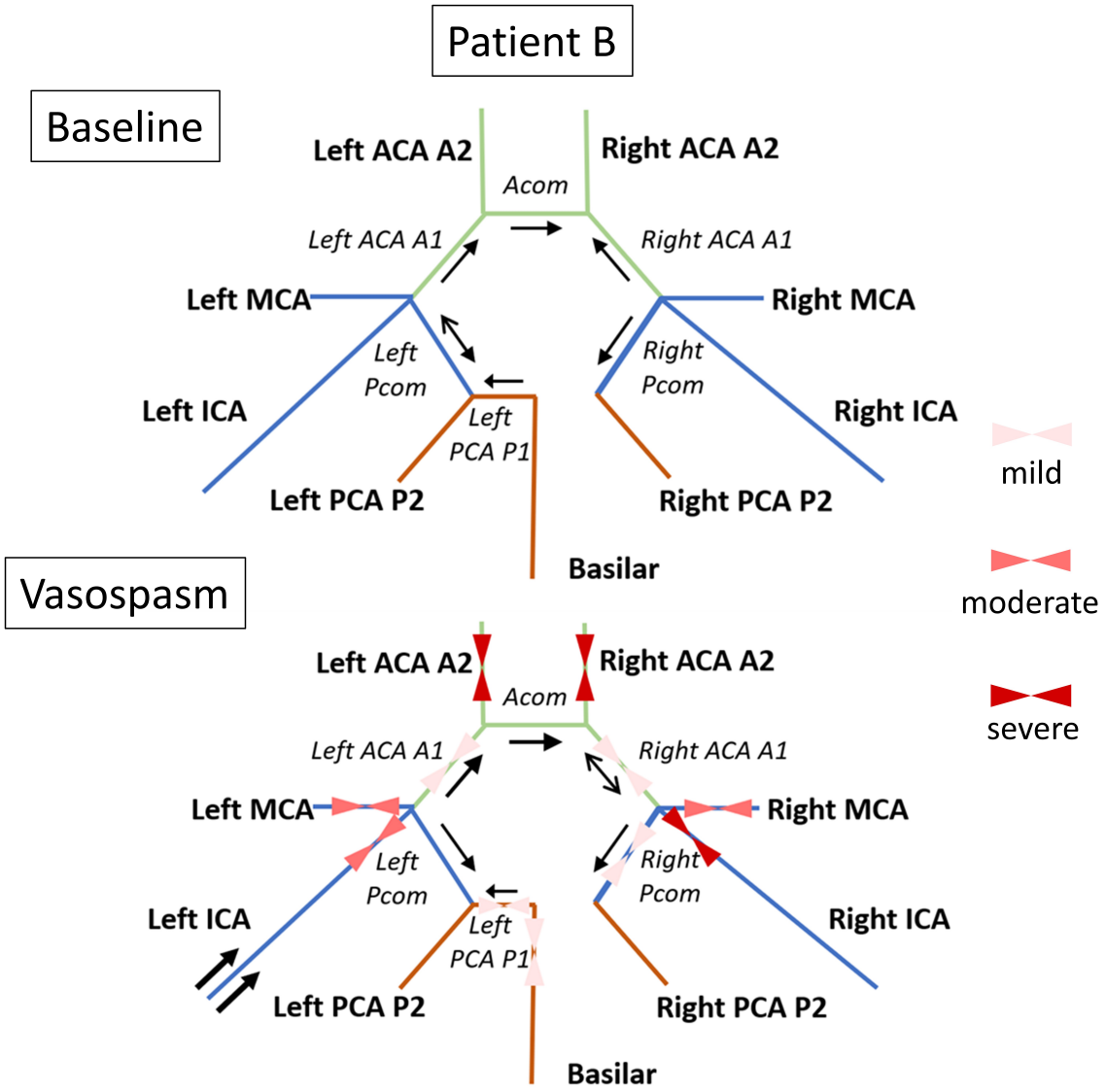

Figure 2.24: Patient B collateral flow directions during the baseline (top) and vasospasm (bottom) conditions exhibited with arrows, the primary recruited inlet artery exhibited with large double arrows, and the locations and severity of vasospasm exhibited with valve icons

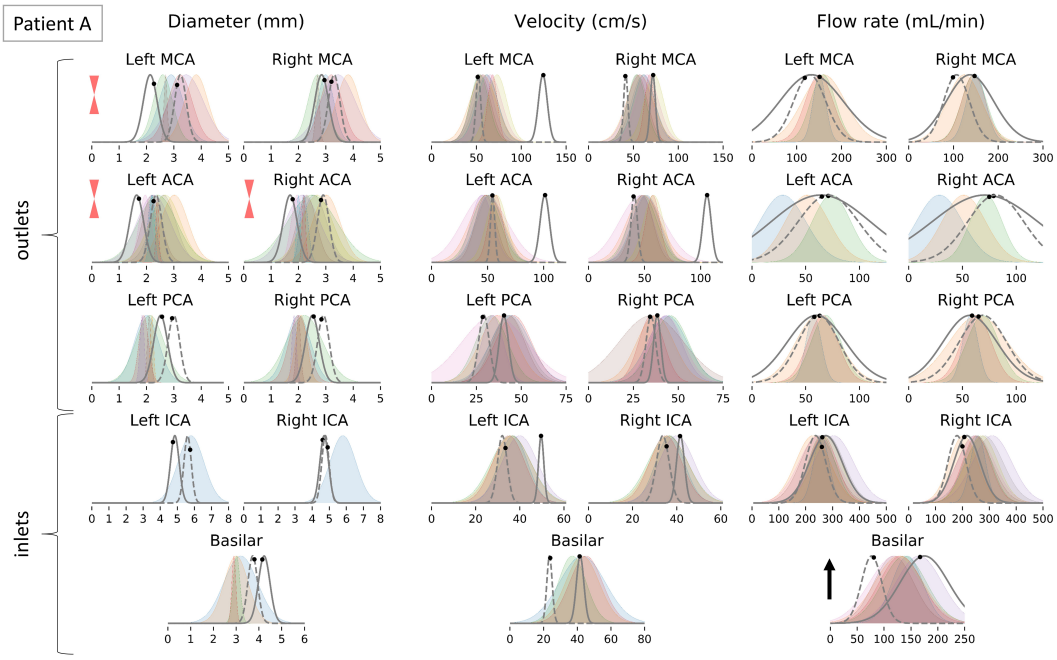

Figure 2.25: Patient A vessel diameters, velocities, and flow rates at baseline (dotted black line with black point) and vasospasm (solid black line with black point) overlayed on literature values (shaded Gaussian distributions)

during vasospasm (Figs. 2.23 and 2.24). The standard deviation for the flow rate reflects how high or low the flow rate could be given an increase or decrease in the diameter by half of the CTA pixel size. The flow rates scaled linearly with the velocity and with the square of the diameter (Eqn. 2.2), making them more sensitive to changes in diameter than velocity. The Gaussian distributions for flow rates were wider than the distributions for the diameter and velocity priors due to this square relationship between changes in diameter and the resulting flow rate. The Gaussian distributions for the vasospasm flow rates (solid black line) were wider than the baseline distributions (dashed black line); changes in flow rate due to the change in diameter were then multiplied by the higher vasospasm velocity, resulting in a wider distribution.

For patient A at baseline, most of the diameters, velocities, and flow rates from the

simulation (Fig. 2.25, dashed lines with a black point) fell within typical literature ranges (Fig. 2.25, shaded Gaussian distributions). While the diameters of the PCAs were larger than the typical literature values, their corresponding velocities were lower, resulting in physiologically realistic flow rates. The velocity in the BAS was especially low, resulting in a flow rate significantly below typical literature values. The Bayesian analysis resulted in smaller outlet diameters and larger inlet diameters as well as higher velocities in the ICAs (Fig. 2.25, black points on dashed lines). The remaining velocities were relatively unchanged due to their low intercycle variabilities. During vasospasm for patient A, the diameters decreased in the left MCA and in both ACAs compared to the baseline condition (Fig. 2.25, distributions with valve icons). The decrease in cross-sectional area of these vessels caused their velocities to increase. This combination of the decreases in diameter and increases in velocity resulted in similar flow rates to baseline. The Bayesian analysis increased the MCA and ACA diameters and decreased the ICA diameters, with other parameters remaining unchanged. In the left ICA, the velocity increased significantly but was accompanied by a decrease in the diameter, resulting in a flow rate similar to baseline. In the BA, both the diameter and velocity increased, resulting in a significantly higher flow rate than baseline (Fig. 2.25, black arrow at bottom right). The basilar flow rate increased from supplying 8% of the total perfusion before vasospasm to 22% during vasospasm due to the recruitment of the posterior circulation to help supply the anterior circulation in vasospasm via reverse flow in both Pcoms (Fig. 2.23).

In patient B at baseline, most of the diameters (Fig. 2.26, dashed lines with a black point) were higher than the literature values, which was balanced by lower velocities, resulting in similar flow rates to those reported in the literature. The availability of literature values for the ICAs and basilar arteries for fetal PCA anatomy is limited, but the simulation values agreed with at least one of the referenced studies [66, 158, 174]. The Bayesian analysis did not noticeably change the parameter values. Vasospasm in both ACAs and MCAs in patient B (Fig. 2.26, distributions with valve icons) was

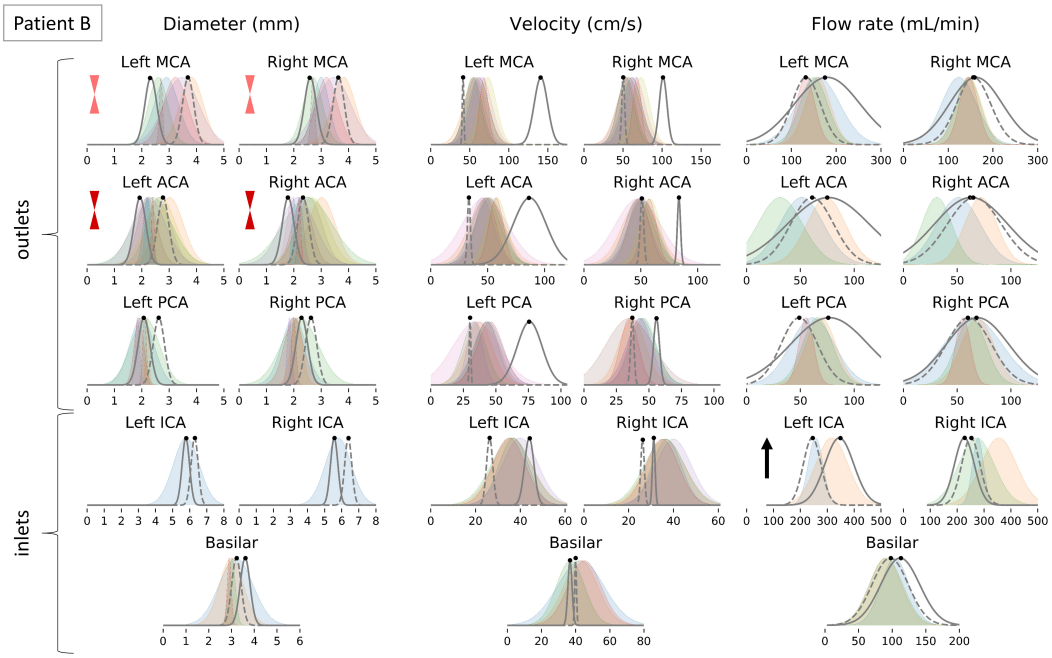

Figure 2.26: Patient B vessel diameters, velocities, and flow rates at baseline (dotted black line with black point) and vasospasm (solid black line with black point) overlayed on literature values (shaded Gaussian distributions)

characterized by smaller diameters and higher velocities. The velocity in the left PCA was higher than literature values, which could be explained by vasospasm near the P1-P2 bifurcation or by the change in flow direction in the left Pcom as a collateral pathway. Both the diameter and velocity in the left ICA increased, resulting in a significantly higher flow rate (Fig. 2.26, bottom right). The flow rate in the left ICA increased from supplying 45% of the total perfusion before vasospasm to 55% during vasospasm, helping supply the right side of the CoW through reverse flow in the right ACA A1 segment (Fig. 2.24).

2.3.3 Virtual Angiography

Figure 2.27 compares the clinical (left column) and virtual (right column) angiograms for patient A at baseline (top row) and vasospasm (bottom row). At baseline, the left ICA was injected with contrast with an angiographic view from front to back, i.e., the right side of the CoW appears on the left side of the figure. In both the clinical and virtual angiograms, the presence of contrast in both ACA A2 segments indicated that the flow in the Acom was from left to right (Fig. 2.27, top row). In the posterior circulation, the reversal of flow in the left PCA P1 segment in the clinical angiogram was inferred from the presence of contrast in the right PCA and right SCA (Fig. 2.27, top left). The virtual angiogram exhibited the same result, with reverse flow in the left PCA P1 filling the right PCA (Fig. 2.27, top right).

For the vasospasm condition in patient A, the BAS was injected with contrast with an angiographic view from the side, i.e., the posterior circulation appears on the left side of the figure (Fig. 2.27, bottom row). Due to the presence of vasospasm in the anterior circulation, the BAS was recruited to help maintain physiological perfusion; blood flowed from the posterior circulation to the anterior circulation via both Pcoms for part of the cardiac cycle. Reverse flow in the right Pcom was stronger than in the left, likely due to vasospasm present in the left Pcom. The strong reverse flow in the right Pcom resulted in a small amount of contrast filling the right MCA, seen in both

the clinical and virtual angiograms (Fig. 2.27, bottom row).

Figure 2.28 shows the left ICA injection in patient B during baseline (top) and vasospasm (bottom), with an angiographic view of front to back, i.e., the right side of the CoW appears on the left side of the figure. At baseline, contrast was present in both ACA A2 segments, corresponding to flow in the Acom from left to right (Fig. 2.28, top row). No reverse flow was present in the right ACA A1 segment. During vasospasm, blood continued to flow strongly from left to right in the Acom. Unlike at baseline, the flow in the right ACA A1 reversed direction, as evidenced by the presence of contrast in the vessel connected to the Acom (Fig. 2.28, bottom left). Some flow from the right ICA injection (not presented here) was antegrade, i.e., toward the ACA A2 segments, indicating bidirectional flow in the right ACA A1 segment. The left ICA was recruited to help supply the right side of the CoW due to the severe vasospasm in the right supraclinoid ICA compared to the moderate vasospasm in the left supraclinoid ICA. Due to the fetal PCA, the BAS and right-sided anterior circulation were not connected, preventing the BAS from being recruited to help supply the vasospastic right MCA (Fig. 2.24).

2.3.4 Sensitivity Analysis

Figure 2.29 shows the results of the sensitivity analysis quantifying the changes in collateral flow rates caused by changes in both the vessel diameters and velocities, as described in section 2.2.12. The widest part of the violin, seen at the centerline with a white point, represents the median value in the distribution and corresponds to the optimal parameter value used in the CFD simulation. The black bar at the centerline of the violin shows the interquartile range. A violin with a wide range of values indicates that the collateral flow rate is more sensitive to variations in diameter and velocity than a violin with a smaller range.

In patient A at baseline (Fig. 2.29, top), the flow was weakly from left to right in the Acom, strongly from A1 to A2 in both ACAs, strongly from anterior to posterior

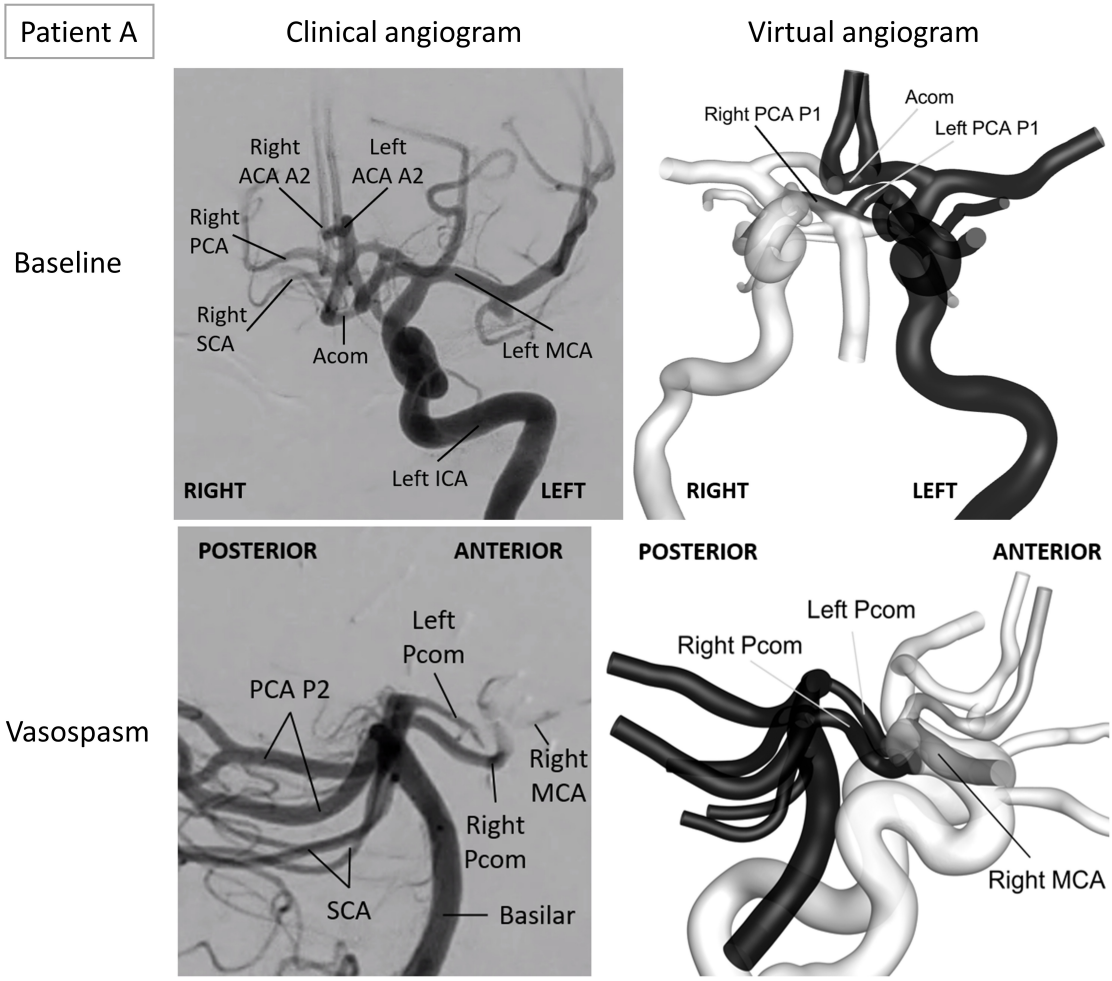

Figure 2.27: Patient A clinical (left) and virtual (right) angiograms for baseline (top) and vasospasm (bottom)

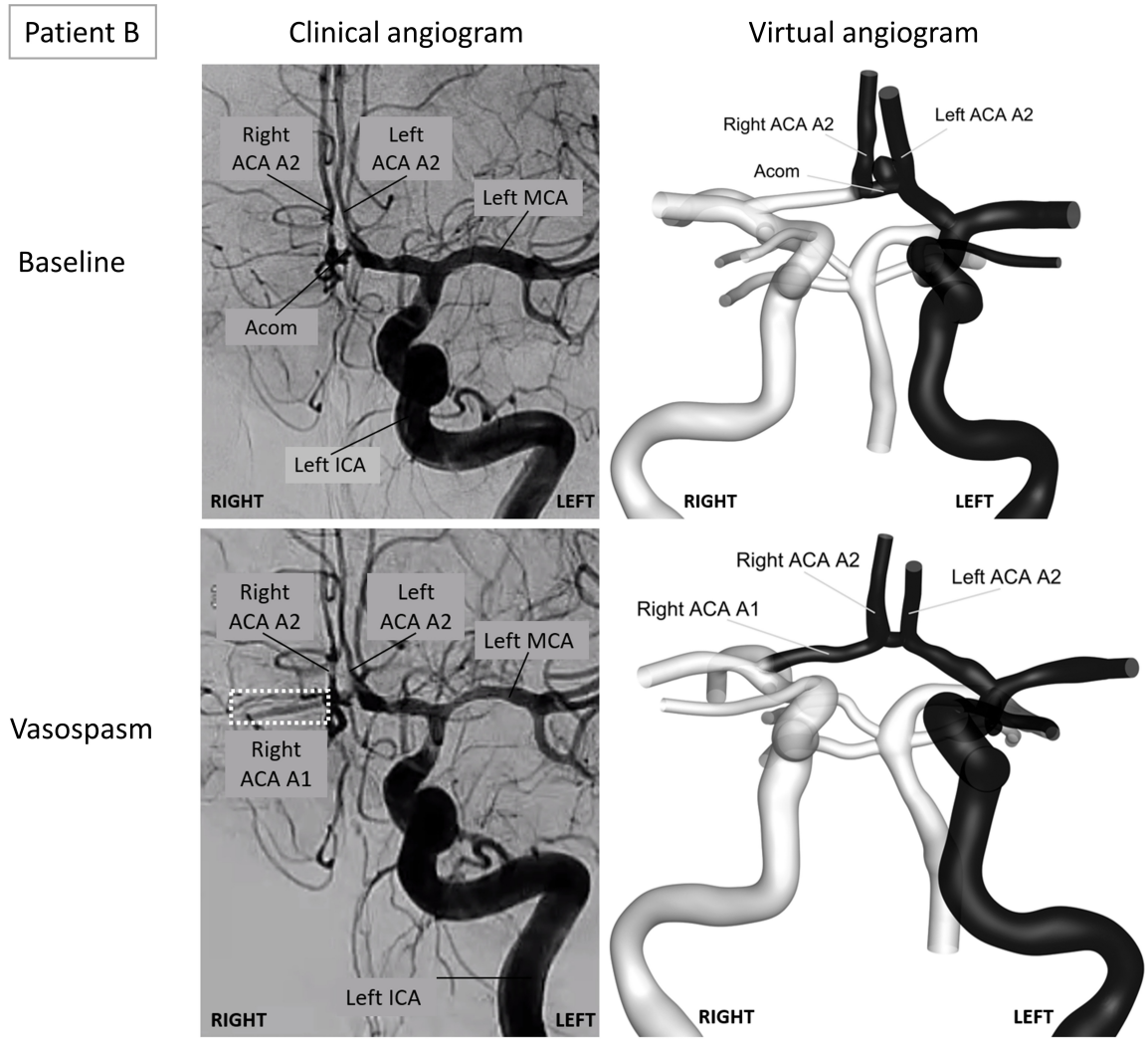

Figure 2.28: Patient B clinical (left) and virtual (right) angiograms for baseline (top) and vasospasm (bottom)

in both Pcoms, and strongly from P1 to P2 in the right PCA. In the left PCA P1 segment, the net flow rate was close to zero, resulting in bidirectional flow (Fig. 2.23). During vasospasm, the flow rates in the Acom and ACA A2 segments were almost identical to the baseline values. However, the net flow rates in both Pcoms were close to zero, indicating bidirectional flow. The flows in both PCA P1 segments were strongly from the P1 to P2 segments due to the recruitment of the BAS, eliminating the reverse flow seen in the left PCA P1 segment at baseline (Fig. 2.23). Despite the uncertainties in the input parameters, the same trends for the flow directions hold for different parameter sets and match the clinically observed flow directions (Fig. 2.23).

In patient B at both baseline and vasospasm (Fig. 2.29, bottom), the flow rates were from left to right in the Acom and antegrade in the left ACA A1, the right Pcom, and the left PCA P1. At baseline, the flow was weakly bidirectional in the left Pcom (Fig. 2.24), which resulted in a low net flow rate in this segment. During vasospasm, the strength of the flow increased in the Acom and left ACA A1 segments, resulting in bidirectional flow in the right ACA A1, and the median flow rate fell to zero. The flow in the left Pcom increased, resulting in antegrade flow. For all collateral pathways, the directions and magnitudes of flow were similar across different parameter sets, agreeing with the clinical results (Fig. 2.24).

2.3.5 Comparison of Percent Changes in Resistance and Dissipation with Angiographic Severity

Comparisons of the angiographic severity to the percent changes in resistance and dissipation are shown in Fig. 2.30. Figure 2.30 plot the percent changes in resistance and dissipation across the vessels in the CoW for the entire cohort associated with an angiographic severity of “none”, “mild”, “moderate”, or “severe”.

Boxplots for the percent change in resistance (Fig. 2.30, top) and dissipation (Fig. 2.30, bottom) show that for increasing angiographic severity, the percent changes in resistance and dissipation also increase. For an angiographic severity of “none”, the

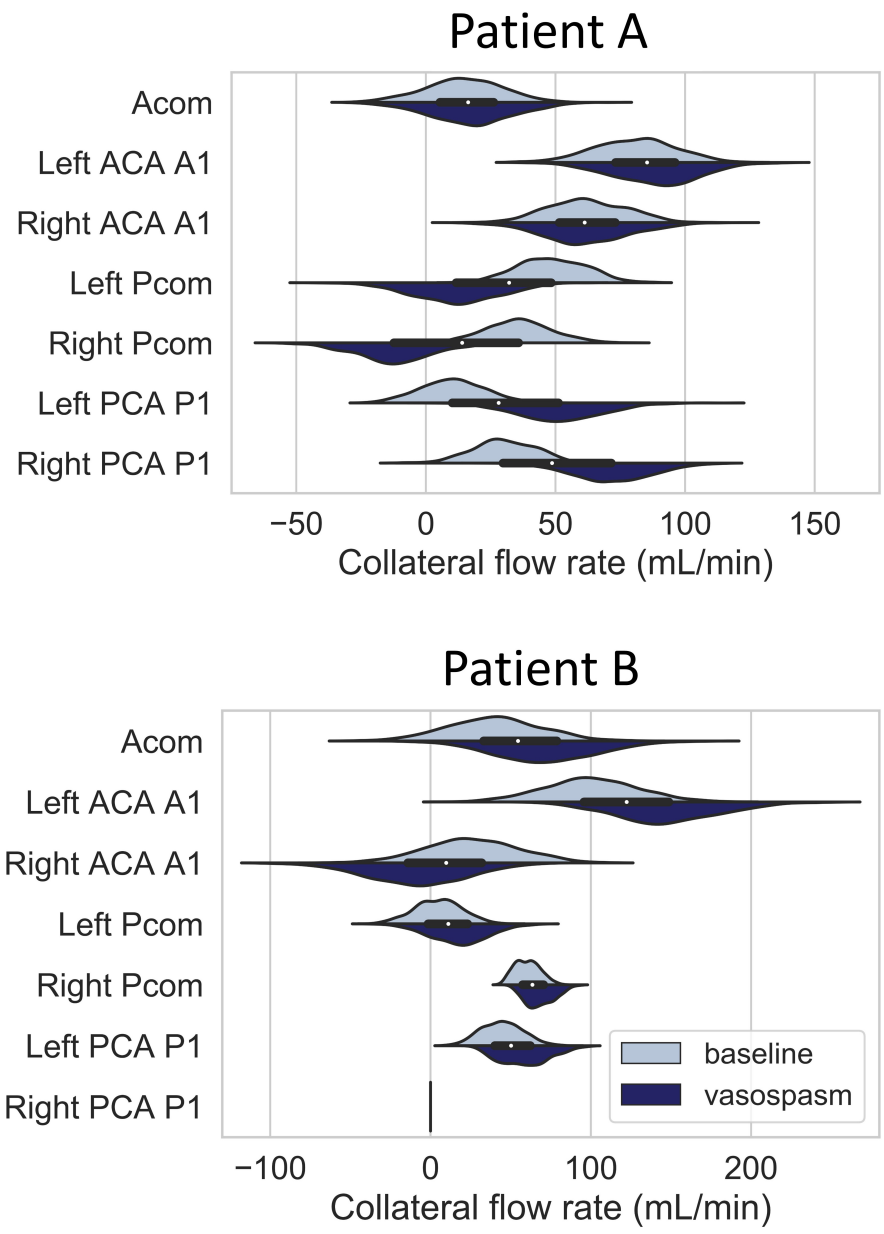

Figure 2.29: Violin plot for the sensitivity analysis that solves a linear system of equations for different parameter sets for patient A (top) and patient B (bottom) during the baseline (light shade) and vasospasm (dark shade) conditions

first and third quartiles are 21% and 210% change in resistance and 60% and 300% change in dissipation, respectively. For an angiographic severity of "severe", the first and third quartiles are 390% and 1250% change in resistance and 500% and 1420% change in dissipation, respectively. This shows higher variability in the CFD metrics for angiographically severe vasospasm than for vessels with lower angiographic severity. The degree of stenosis is the main factor used to qualitatively evaluate the vasospasm severity during the angiographic review. While some vessels may have a high degree of stenosis, this stenosis will not necessarily lead to higher percent changes in resistance and dissipation. For instance, focal vasospasm may lead to a more severe angiographic evaluation than the hemodynamics suggest. Recovery of static pressure downstream of the constriction causes the resistance to be lower compared to vessels with diffuse vasospasm. Viscous losses will be highest in the stenosed region, but the total volume of that region compared to the entire vessel is relatively low.

The number of vessels across all patients that fall within the ranges 0-250%, 250-500%, 500-750%, or above 750% change of one of the CFD metrics were counted, and the percent of those vessels with a specific angiographic severity were determined. These results are represented in the bar plots for resistance (Fig. 2.31, top) and dissipation (Fig. 2.31, bottom). For example, out of 171 vessels with 0-250% change in resistance, 86 of those vessels had an angiographic severity of "none", represented with 50% of the total vessels in that category in the bar chart. For changes in resistance above 750%, 90% of the vessels across all patients were assigned angiographically as moderate or severe (Fig. 2.31, top). For changes in dissipation above 750%, 80% of the vessels were assigned angiographically as moderate or severe (Fig. 2.31, bottom). This trend demonstrates that the CFD metrics capture the change in hemodynamics due to severe vasospasm with high fidelity. For the range of 0-250% in resistance or dissipation, there is a wider variability in the angiographic assignment of vasospasm severity. Similar to the trend identified by the boxplots, the angiographic severity may overestimate the impact of the vessel stenosis, especially with focal vasospasm,

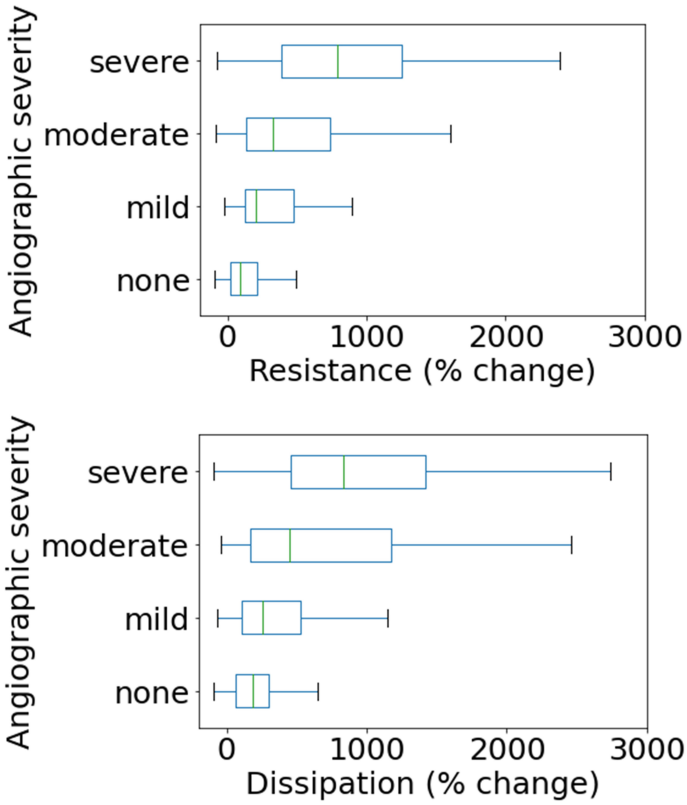

Figure 2.30: Boxplots of percent changes in resistance (top) and dissipation (bottom) associated with each angiographic severity

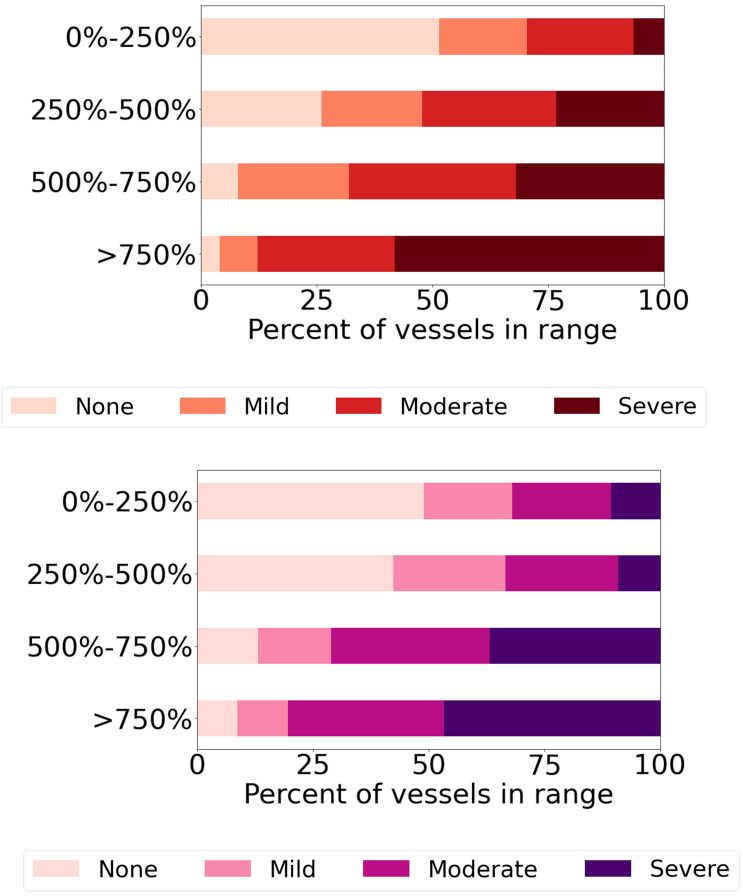

Figure 2.31: Bar charts of the percent of vessels in ranges of resistance (top) and dissipation (bottom) metrics with an associated angiographic severity

leading to a discrepancy between the CFD metrics and the angiographic assignment.

Figure 2.32 plots the percent of vessels across all patients where the CFD evaluation of severity agrees with the angiographic severity. Agreement is defined as the difference in CFD severity and angiographic assessment being within one level. For instance, if the CFD metric indicates "moderate" severity, the angiographic categorization could be "mild", "moderate", or "severe" and be considered good agreement. This definition of agreement is applied because the angiographic evaluation of severity is qualitative, and the difference between categories like "mild" and "moderate"

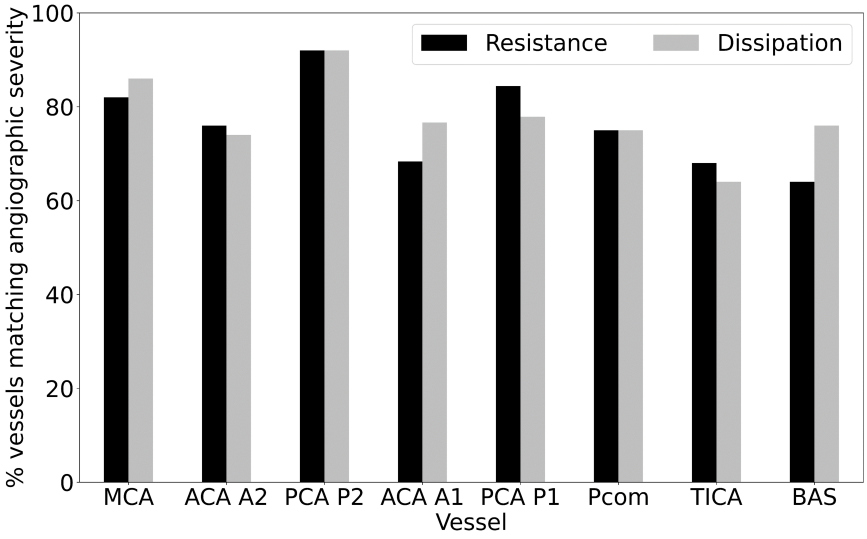

Figure 2.32: Percent of vessels across the cohort that agree with the angiographic severity based on the resistance (black) and dissipation (grey) metrics

is subjective, i.e., at the discretion of the neurosurgeon.

In the MCAs, the degree of agreement with the angiographic severity is 82% for resistance and 86% for dissipation. Because the MCA is one of the largest vessels within the CoW, the degree of uncertainty introduced by the resolution of the CTA scan is lower than in other vessels. While five patients had aneurysms in the MCA, the surgical clips used to treat the aneurysm were in the M2 segment. The diameter measurements were not obscured by artifacts in the CTA.

In the ACA A2 segments, the degree of agreement with the angiographic severity is about 75% for both CFD metrics. Twelve patients had aneurysms in the Acom, and one patient had an aneurysm in the ACA A2 segment. The aneurysms were treated with coils or clips, which can affect the diameter measurements due to artifacts in the CTA. Flow in the Acom can be relatively fast, so a jet originating from the Acom can impinge at the bifurcation between the ACA A2 segment and the Acom. The presence of this jet impingement can cause the pressure drop at the beginning of the

vessel to be underestimated, even if the vessel diameter during vasospasm is smaller than the baseline diameter. These jet dynamics affect the calculation of CFD metrics, which could explain some differences between angiographic and CFD severities in the ACA A2 segments. The ACA A2 segments are smaller than other vessels in the CoW, which makes the diameters more sensitive to the resolution of the CTA.

In the PCA P2 segments, the degree of agreement between the CFD and angiographic severity is 92%. The severity in the PCA P2 segments is more likely to be assigned as "none" or "mild" compared to the vessels in the anterior circulation. As seen in the boxplots in Fig. 2.30, there is lower variability in the CFD metrics in the "none" and "mild" categories, with most vessels falling within the 0-250% range associated with the CFD categorization of "none" and the 250-500% range associated with the CFD categorization of "mild". Therefore, close agreement between the CFD and angiographic severity is expected in the PCA P2 segments.

The ACA A1 segments show 69% agreement with the angiographic severity for resistance and about 77% agreement for dissipation. Similar to the ACA A2 segments, the diameter measurements in the ACA A1 segments can be challenging due to artifacts from coils or clips, and the evaluation of static pressure can be affected by jet impingement near the Acom.

The level of agreement in the PCA P1 segments with the angiographic severity is 85% for percent change in resistance and 78% for percent change in resistance. As is the case for the PCA P2 segments, the PCA P1 segments are more likely to be assigned as "none" or "mild" in angiographic severity than the anterior circulation, increasing the likelihood of agreement. However, the vessels are shorter in length than other vessels in the CoW, which could introduce higher error in the CFD metrics than for longer vessels.

Across the cohort, a left or right Pcom was assigned an angiographic severity in 20 instances. The CFD metrics agreed with the angiographic severity in 75% percent of these Pcoms. Due to the smaller diameter of the Pcom compared to the rest of the

CoW, it is more likely to be sensitive to CTA resolution.

In the TICAs, the resistance metric shows 68% agreement and dissipation shows 64% agreement with the angiographic severity. Focal vasospasm is common in the TICAs, which results in pressure recovery downstream of the constriction. This phenomenon causes the resistance in a vessel with focal vasospasm to be lower than a vessel with consistent narrowing. Therefore, the CFD metrics are less likely to indicate severe vasospasm in these vessels than the angiographic severity, which is based on the degree of narrowing. Three patients had left Pcom aneurysms treated with coils or clips, and CTA artifacts from aneurysm treatment may have affected the measurements of the TICA diameter.

In the BAS, the level of agreement with the angiographic severity is 64% according to the resistance and 76% according to the dissipation. This artery is often characterized by a high degree of curvature. In the presence of vasospasm, a jet can form that impinges at the location of highest curvature, which causes the pressure drop, and thus the resistance, to be underestimated. This phenomenon may explain why the degree of agreement is closer for dissipation than resistance in this particular vessel.

2.3.6 Representative Patients to Illustrate Resistance and Dissipation Metrics

Sections 2.3.7, 2.3.8, and 2.3.9 discuss in detail eight representative patients that show good agreement between the resistance and dissipation metrics. Four patients demonstrate localization of vasospasm (section 2.3.7), and two patients demonstrate balanced vasospasm (section 2.3.8). Two patients were identified to have infarct (section 2.3.9).

For a brief overview of the patients in the remainder of the cohort, the interested reader is directed to sections 2.3.11-2.3.14.

2.3.7 Collateral Flow Changes in Patients with Localized Vasospasm

Figure 2.33 presents the angiographic evaluation and CFD results from two representative patients with localized vasospasm in one zone as defined in section 2.2.18. "L" represents the left side in the vessel labels, and "R" represents the right side. The ACA A1 and A2 segments are labeled as A1 and A2, respectively, and the PCA P1 and P2 segments are labeled as P1 and P2, respectively. Patient 1 is represented on the left side of the figure, and Patient 2 is represented on the right side of the figure. The diagrams at the top represent the angiographic severity, with absence of a valve icon reflecting no vasospasm, and the increasing darkness of the valve icon representing increasing severity. The width of the grey line represents the size of the collateral pathways according to the angiographic review, with hypoplastic segments represented by thinner lines. The diagrams at the center represent the percent change in resistance, and the bottom diagrams represent the percent change in dissipation. When the Pcom is represented with a dashed line in the resistance and dissipation diagrams, this indicates that its severity of vasospasm could not be angiographically determined. A black arrow represents a change in the direction of flow in a collateral pathway as defined in section 2.1.9.

Patient 1 demonstrated a complete CoW, and the bilateral Pcoms and the right ACA A1 segments were identified as hypoplastic. Severe vasospasm in the right anterior circulation was identified by the angiographic evaluation as well as by changes in resistance and dissipation. In the Acom, there was no net flow during baseline, while flow was left to right during vasospasm; thus, the change in direction was assigned as left to right. The left ACA A1 showed a significant strengthening in the magnitude of the flow during vasospasm. Considering the changes in flow direction in these two collateral pathways, it appears that the left anterior circulation was directing flow to the right anterior circulation in severe vasospasm. The magnitude of the flow in the hypoplastic right ACA A1 segment weakened, likely due to the

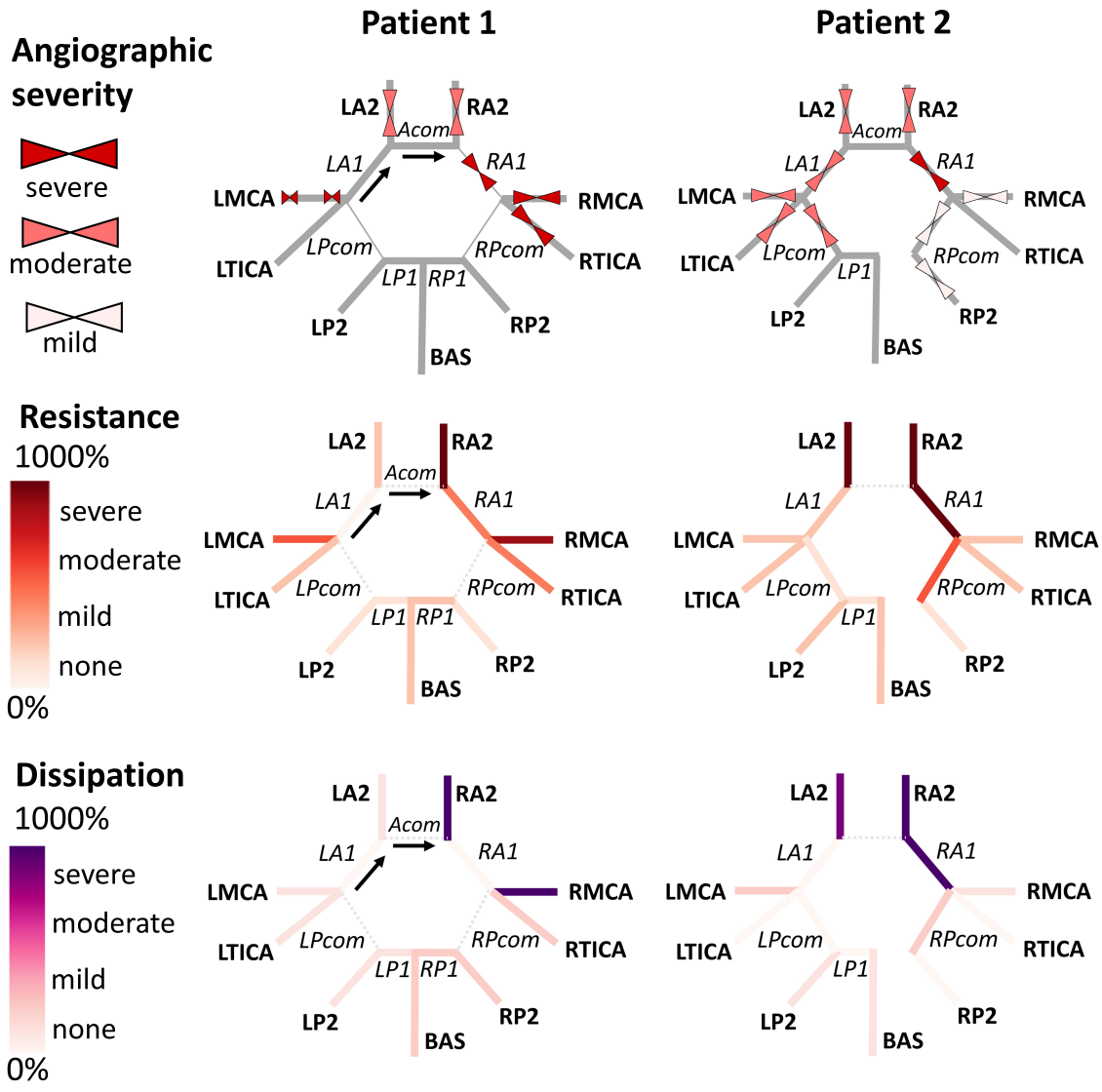

Figure 2.33: Patients 1 and 2 with vasospasm localized in one zone of the CoW with the angiographic severity (top), percent change in resistance (middle) and percent change in dissipation (bottom) in each vessel

presence of vasospasm identified as moderate by the percent change in resistance and severe in the angiographic review. Because the bilateral Pcoms are hypoplastic, this could have affected the ability of the posterior circulation to direct flow to the anterior circulation.

Patient 2 was missing the right PCA P1 segment, resulting in a fetal right PCA. All remaining collateral pathways were present and of typical sizes. While the angiographic review did not clearly identify localized vasospasm, the resistance and dissipation metrics identified localization of severe vasospasm in the right anterior circulation. Despite the patency of the left ACA A1 and Acom segments, there were no significant changes in flow direction to compensate for localized right anterior vasospasm. The flow weakened in the right ACA A1 segment, likely due to severe vasospasm identified in the angiographic review and both CFD metrics. The absence of the right PCA P1 segment isolated the posterior circulation from the right anterior circulation, preventing recruitment of the posterior circulation to supply the anterior circulation on the right side.

Figure 2.34 shows two patients with localized vasospasm in two zones of the CoW, as defined in section 2.2.18, with the same diagrammatic organization as in Fig. 2.33. Patient 3 is represented on the left side of the figure, which is the same as Patient A that was used to illustrate the computational methodology. Patient 4 is represented on the right side of the figure.

Patient 3 had a complete CoW with no hypoplastic segments. Vasospasm was localized in the left and right anterior zones identified by the angiographic severity and both CFD metrics. During baseline, the flow in the bilateral Pcoms was strongly antegrade whereas during vasospasm, it changed to strongly biphasic (Fig. 2.23). Therefore, the flow direction change was from posterior to anterior. Due to the strong antegrade flow in the left Pcom during baseline, biphasic flow was present in the left PCA P1, which changed to antegrade flow during vasospasm (Fig. 2.23). The change in direction was towards the left Pcom and left PCA P2. These changes in

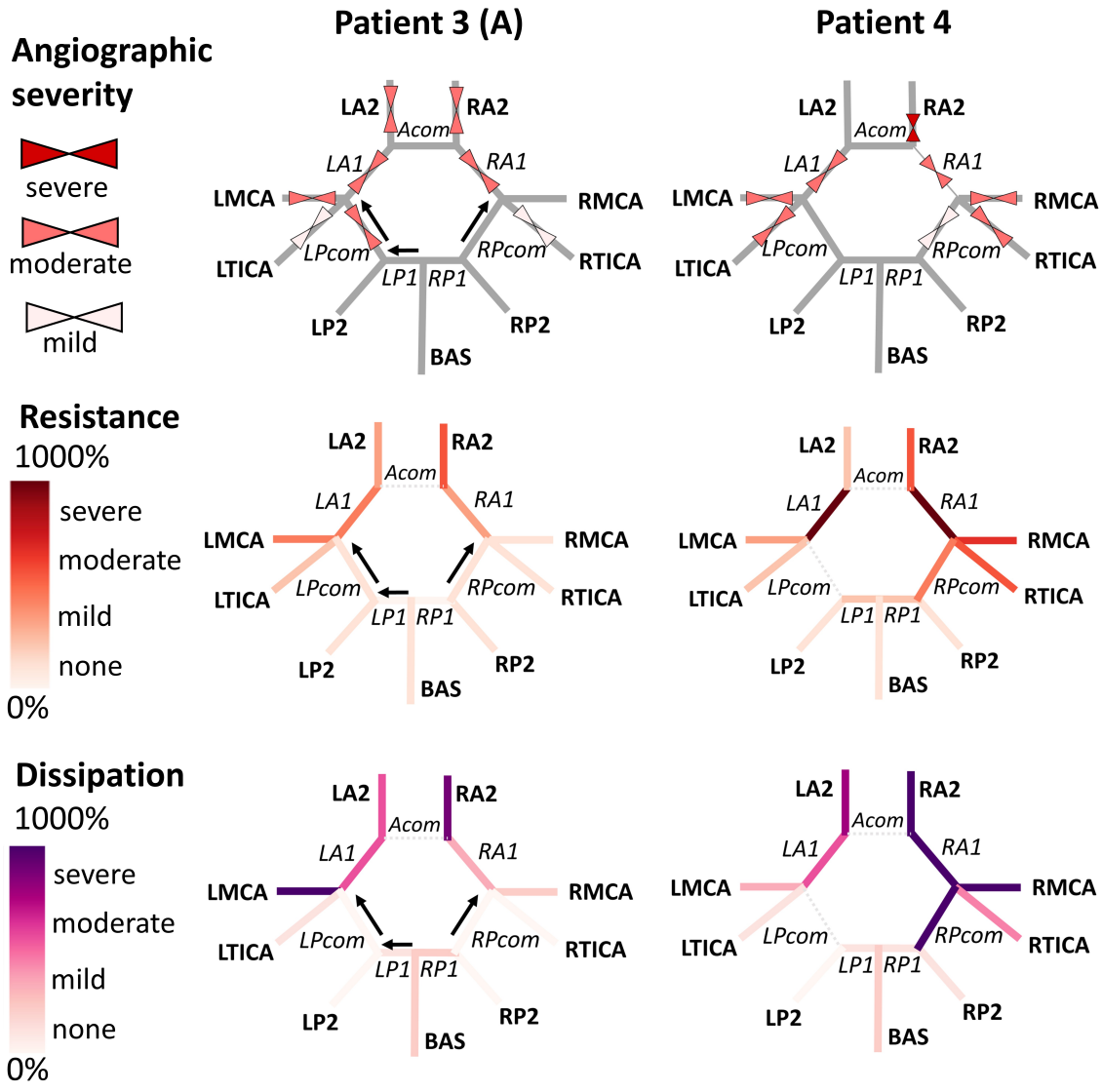

Figure 2.34: Patients 3 and 4 with vasospasm localized in two zones of the CoW with the angiographic severity (top), percent change in resistance (middle) and percent change in dissipation (bottom) in each vessel

direction in the bilateral Pcoms and left PCA P1 segment can be considered to be caused by recruitment of the posterior circulation to supply the anterior circulation in vasospasm in a patient with patent collateral pathways.

Patient 4 had a complete CoW with a hypoplastic right ACA A1 segment. The angiographic severity, resistance, and dissipation all reflected vasospasm localized in the left and right anterior zones. The CFD metrics indicated that vasospasm was more severe in the right than the left anterior circulation. There were no major changes in the flow direction in the collateral pathways. The flow weakened in magnitude in the right ACA A1, likely due to the severe vasospasm identified by the changes in resistance and dissipation. In the right Pcom, the percent change in dissipation identified severe vasospasm due to focal vasospasm, which might have decreased the likelihood of a change in direction.

2.3.8 Collateral Flow Changes in Patients with Balanced Vasospasm

Figure 2.35 shows two patients with balanced vasospasm, as defined in section 2.2.18, with the same organization as Figures 2.33 and 2.34. Patient 5 is represented on the left side of the figure, and Patient 6 is represented on the right side of the figure.

Patient 5 had a complete CoW with no hypoplastic segments. According to the angiographic severity and CFD metrics, the overall degree of vasospasm was weak. Vessels in mild to moderate vasospasm were distributed among the left anterior, right anterior, and posterior zones. Both the overall low severity of vasospasm and the absence of localized vasospasm could explain why no significant changes in flow direction were present.

Patient 6 also had a complete CoW with no hypoplastic segments. Both the angiographic severity and CFD metrics demonstrated that the vasospasm within the CoW was balanced between the three zones. In the left Pcom, the flow direction changed from biphasic during baseline to antegrade during vasospasm, resulting in a change of direction from the anterior to posterior circulation. While the vasospasm

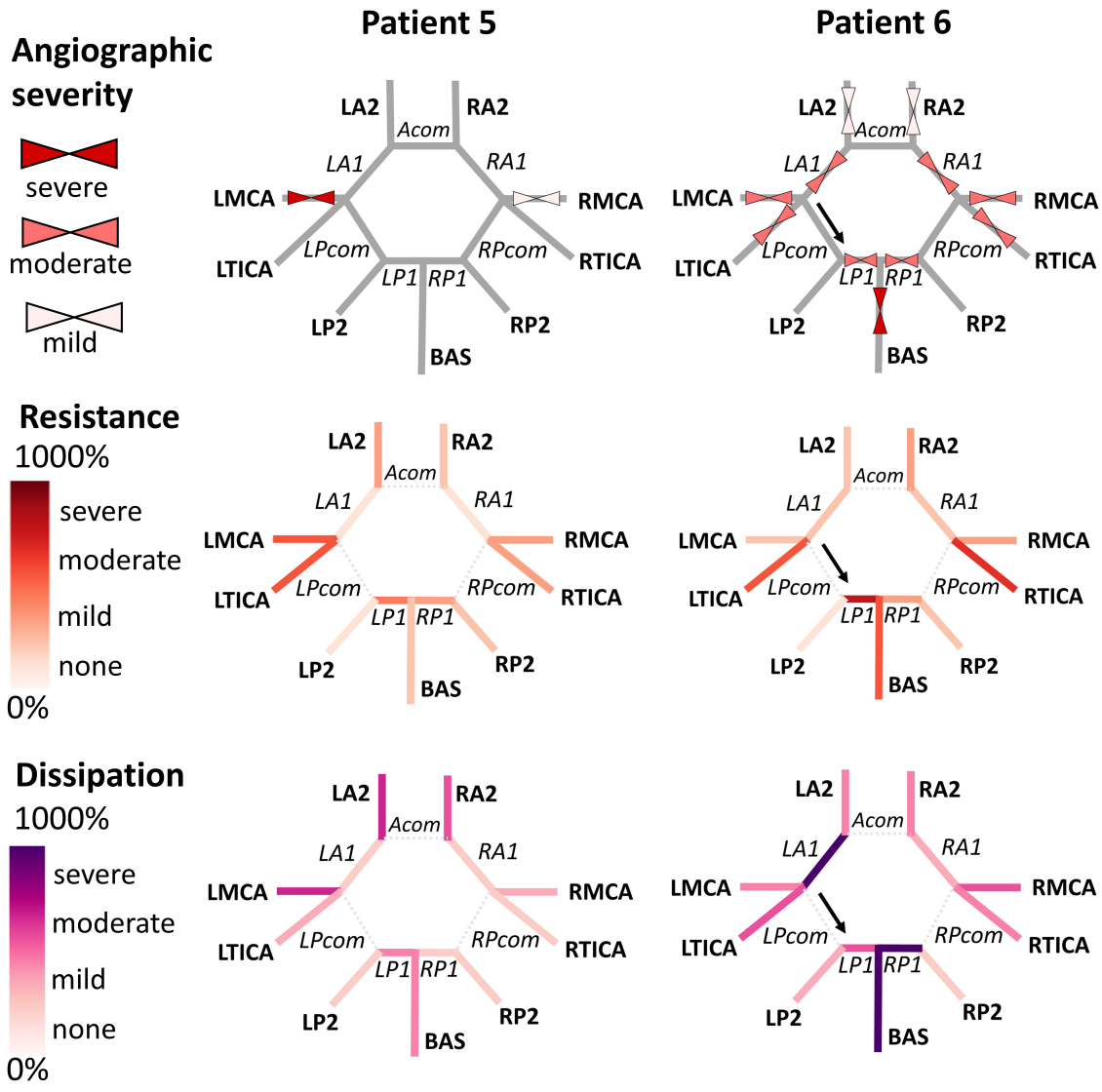

Figure 2.35: Patients 5 and 6 with vasospasm balanced across zones in the CoW with the angiographic severity (top), percent change in resistance (middle) and percent change in dissipation (bottom) in each vessel

was balanced within the CoW, both the angiography and dissipation metric identified the BAS as being in severe vasospasm compared to moderate vasospasm in the bilateral TICAs. This imbalance in vasospasm severity in the supplying vessels could explain why the left Pcom flow direction changes. The percent change in resistance in the BAS underestimated the vasospasm severity because of the effects of high vessel curvature discussed in section 2.3.5.

2.3.9 Collateral Flow Changes in Patients with Infarct Due to Vasospasm

Figure 2.36 represents the two patients who were diagnosed with infarct caused by vasospasm, discussed in section 2.2.2, with the same organization as in Figures 2.33-2.35. Patient 7 is represented on the left side of the figure, and Patient 8 is represented on the right side of the figure. The black circles represent the territories supplied by a vessel in the CoW where infarct was detected.

Patient 7 was missing the Acom and had a hypoplastic right ACA A1 segment and a hypoplastic right Pcom. The angiographic evaluation as well as the CFD metrics identified severe vasospasm across the entirety of the CoW. Vasospasm was balanced between the left and right sides as well as the anterior and posterior circulations. No major changes in the collateral flow directions were observed. The magnitude of the flow in the bilateral PCA P1 segments weakened during vasospasm, which could be a result of the severe BAS vasospasm detected by angiography and the CFD metrics. The absence of large changes in collateral flow directions could be related to the limited connectivity of the CoW between the left and right sides due to the missing Acom as well as the anterior and posterior circulations due to the hypoplastic right Pcom. The presence of balanced severe vasospasm could also affect the likelihood of flow direction changes. Multiterritorial infarct could relate to the high severity of vasospasm in all zones of the CoW along with an inability of collateral pathways to mitigate the negative effects of severe vasospasm.

Patient 8 had a complete CoW with hypoplastic left ACA A1 and left PCA P1

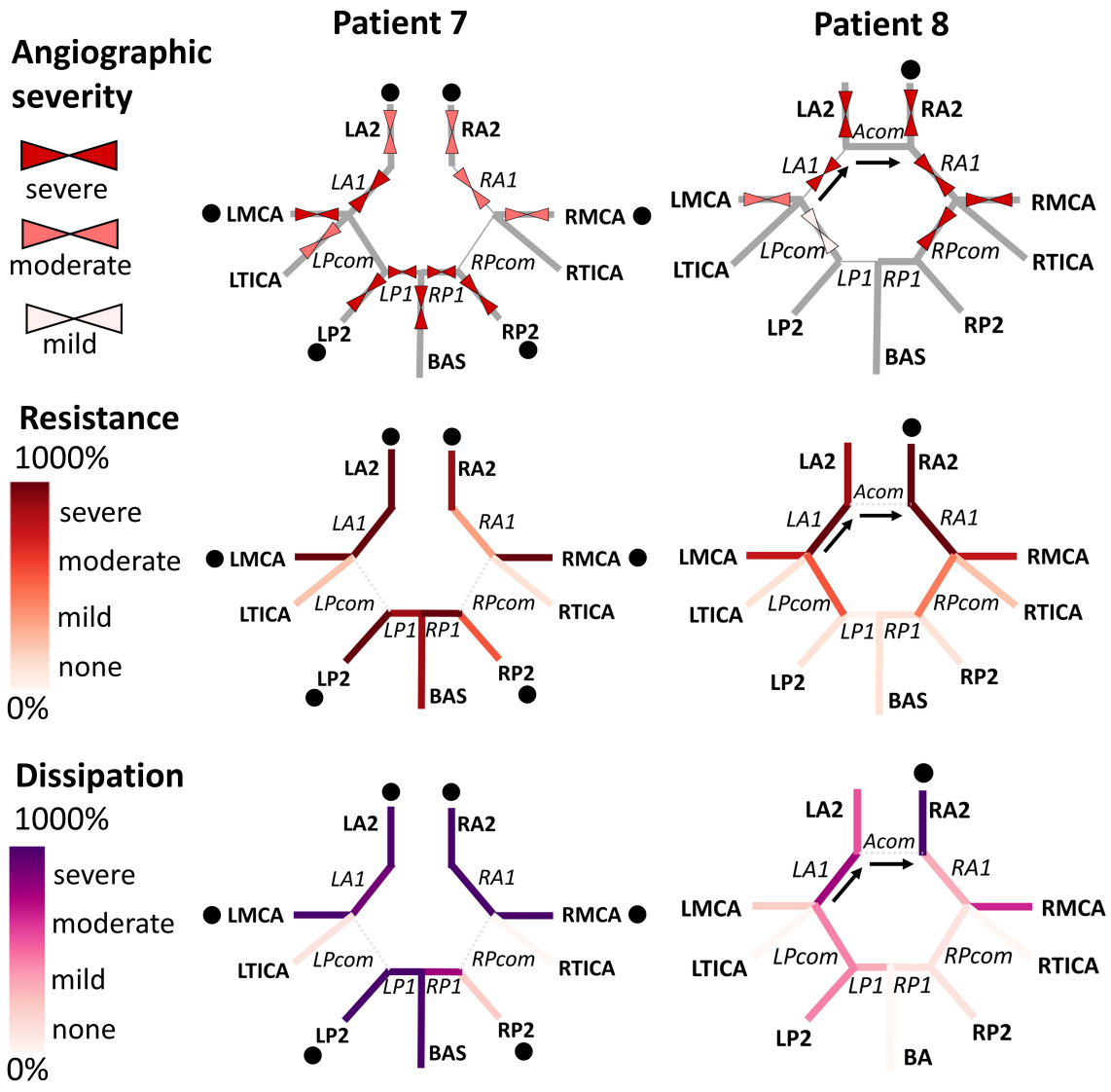

Figure 2.36: Patients 7 and 8 with infarct caused by vasospasm (black circles) with the angiographic severity (top), percent change in resistance (middle) and percent change in dissipation (bottom) in each vessel

segments. Vasospasm was localized in the left and right anterior zones, with the right side exhibiting higher severity than the left side. The flow direction in the left ACA A1 segment changed from biphasic during baseline to weakly antegrade during vasospasm, resulting in a net change of flow towards the ACA A2 segments. In the Acom, the flow direction changed from right to left during baseline to no net flow during vasospasm, resulting in a net change from left to right. This change in direction could result from severe vasospasm in the right ACA A1 limiting the amount of flow available to travel from the right side to the left side, or it could relate to flow being conserved on the right side in order to supply the right ACA A2 segment instead of being directed to the left anterior circulation. This patient had an infarct in the territory supplied by the right ACA A2 segment associated with localized vasospasm in the anterior circulation, and the hypoplastic left ACA A1 and vasospastic right ACA A1 segments limited the ability of collateral pathways to be recruited.

2.3.10 Patients from the Remainder of the Cohort

Sections 2.3.7-2.3.9 highlighted the hemodynamics in eight clear examples from the cohort of 25 patients. The remaining 17 patients from the 25 patient cohort are briefly summarized in the following sections, grouped by patients with vasospasm localized in one zone (section 2.3.11), localized in two zones (section 2.3.12), balanced across three zones (section 2.3.13), and with overall mild vasospasm (section 2.3.14).

2.3.11 Collateral Flow Changes in Patients with Localized Vasospasm in One Zone

Figure 2.37 shows two patients with vasospasm localized in one zone, as defined in section 2.2.18, with the same diagrammatic organization as in Figs. 2.33-2.36. Patient 9 is represented on the left side of the figure, and patient 10 is represented on the right side, which is the same as patient B that was used to illustrate the computational methodology.

Patient 9 had a complete CoW with bilateral hypoplastic Pcoms. Vasospasm was localized in the right anterior circulation, more clearly identified with the CFD metrics than the angiographic evaluation. Two pathways changed direction; the Acom showed a net change from left to right, and the right A1 showed a net change towards antegrade flow. The Acom may have been recruited to supply the right side with localized vasospasm, while it is unclear why the flow direction changed in the right A1. Bilateral hypoplastic Pcoms isolated the posterior circulation from anterior circulation. The resistance in the BAS was underestimated due to the effects of high curvature described in section 2.3.5.

Patient 10 was missing a right P1 segment and had a hypoplastic right A1 segment. Vasospasm was localized in the left anterior circulation. The flow in the right A1 changed from antegrade during baseline to biphasic flow during vasospasm, resulting in a net change towards the right MCA. The angiography and resistance metric identified severe spasm in the right TICA, which could result in the biphasic flow in the right A1. However, the segment was not a major collateral due to its relatively small size. The posterior circulation was isolated from the right anterior circulation due to the fetal PCA, which could limit recruitment of the posterior circulation.

Figure 2.38 shows two patients with vasospasm localized in one zone, as defined in section 2.2.18, with the same diagrammatic organization as in Figs. 2.33-2.37. Patient 11 is represented on the left side of the figure, and patient 12 is represented on the right side.

Patient 11 had a complete CoW with a hypoplastic right Pcom. Vasospasm was localized in the left anterior circulation. There is no clear explanation for why the Acom was not recruited to supply the left side in vasospasm from the right side, despite looking similar in anatomy and localization of vasospasm to Patient 1. The posterior circulation is isolated from the right anterior circulation due to a hypoplastic right Pcom, and the left Pcom is not a major collateral in this patient.

Patient 12 was missing a right A1 segment and had a hypoplastic right Pcom.

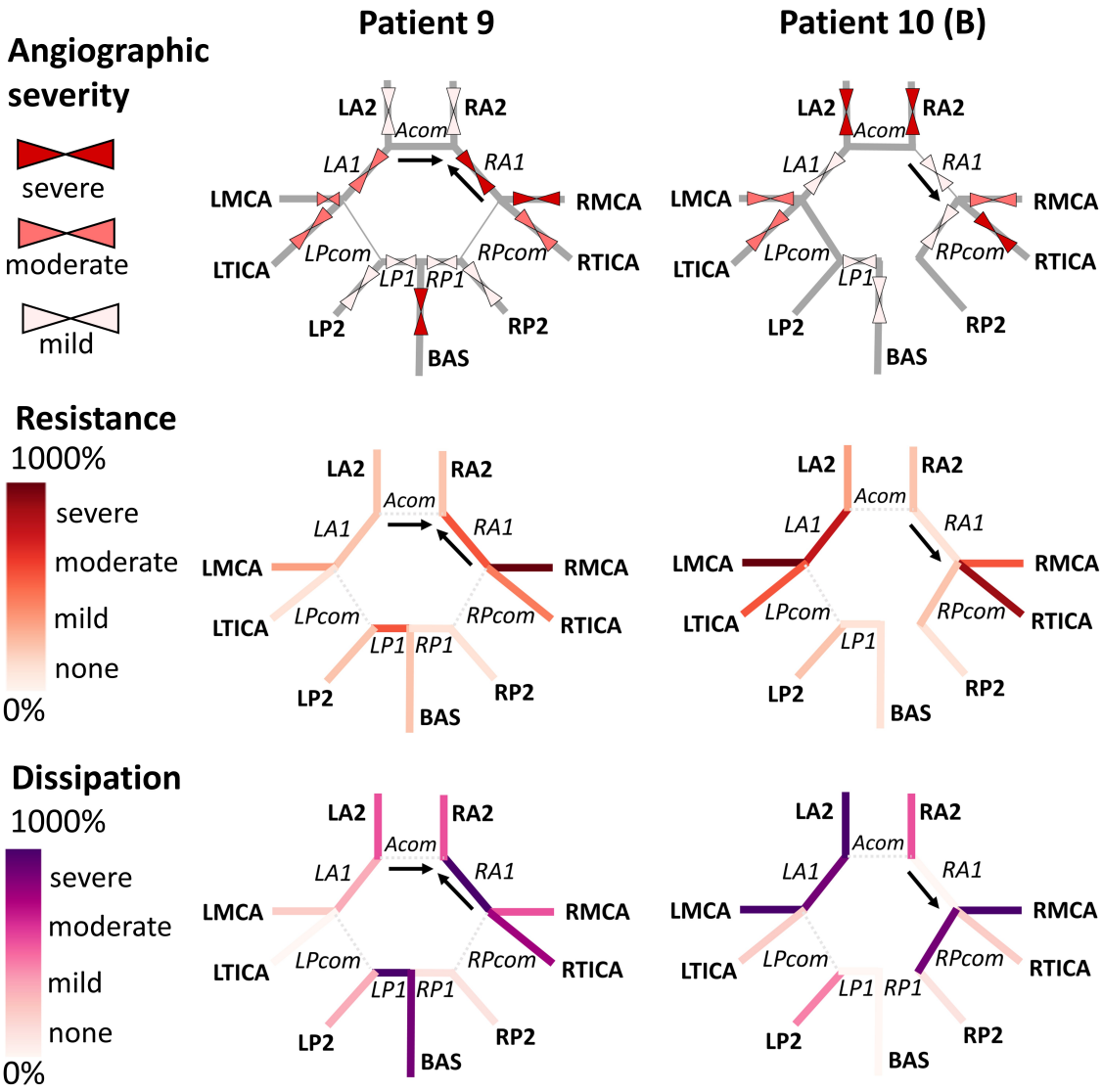

Figure 2.37: Patients 9 and 10 with vasospasm localized in one zone of the CoW with the angiographic severity (top), percent change in resistance (middle) and percent change in dissipation (bottom) in each vessel

Vasospasm was localized in left anterior circulation. The missing right A1 and hypoplastic right Pcom isolated the left side from the right side, limiting its ability to be recruited to supply the left anterior circulation with localized vasospasm.

2.3.12 Collateral Flow Changes in Patients with Localized Vasospasm in Two Zones

Figure 2.39 shows one patient with vasospasm localized in two zones, as defined in section 2.2.18, with the same diagrammatic organization as in Figs. 2.33-2.38.

Patient 13 was missing a left P1 segment. CFD identified vasospasm localized in the left and right anterior circulation, compared with angiographic severity only identifying vasospasm localized in the left anterior circulation. Flow in the left A1 changed from antegrade to biphasic, resulting in a net change of flow towards the left MCA. Flow in the right Pcom changed from antegrade to biphasic, resulting in a net change of flow towards the right MCA. Both changes in flow direction corresponded to flow in the direction of localized vasospasm. The missing left P1 segment isolated the posterior circulation from the left anterior circulation, so the posterior circulation cannot be recruited to the left side.

Figure 2.40 shows two patients with vasospasm localized in two zones, as defined in section 2.2.18, with the same diagrammatic organization as in Figs. 2.33-2.39. Patient 14 is represented on the left side of the figure, and patient 15 is represented on the right side.

Patient 14 had a complete CoW with a hypoplastic right A1 and right P1. Vasospasm was localized in the left and right anterior circulation. The flow in the left Pcom changed from biphasic to weakly antegrade, resulting in a net change towards the BAS. Severe spasm in the left Pcom, identified by both CFD metrics, could limit its ability to act as a collateral from the posterior to the anterior circulation, and the change in direction could be attributed more to a limitation in flow than to recruitment. The right circulation was isolated from the left anterior and posterior circulation due to hypoplastic right A1 and P1 segments.

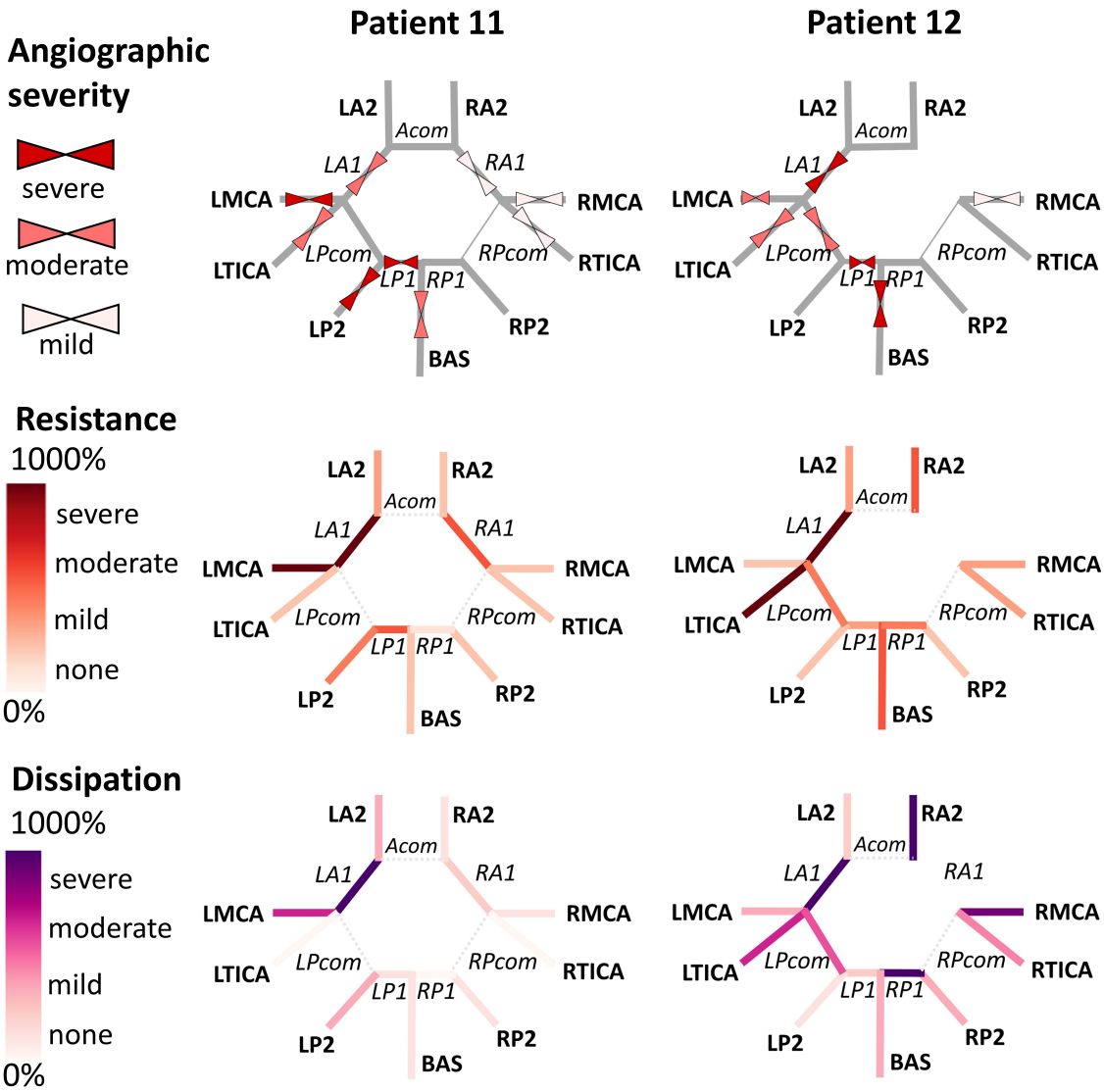

Figure 2.38: Patients 11 and 12 with vasospasm localized in one zone of the CoW with the angiographic severity (top), percent change in resistance (middle) and percent change in dissipation (bottom) in each vessel

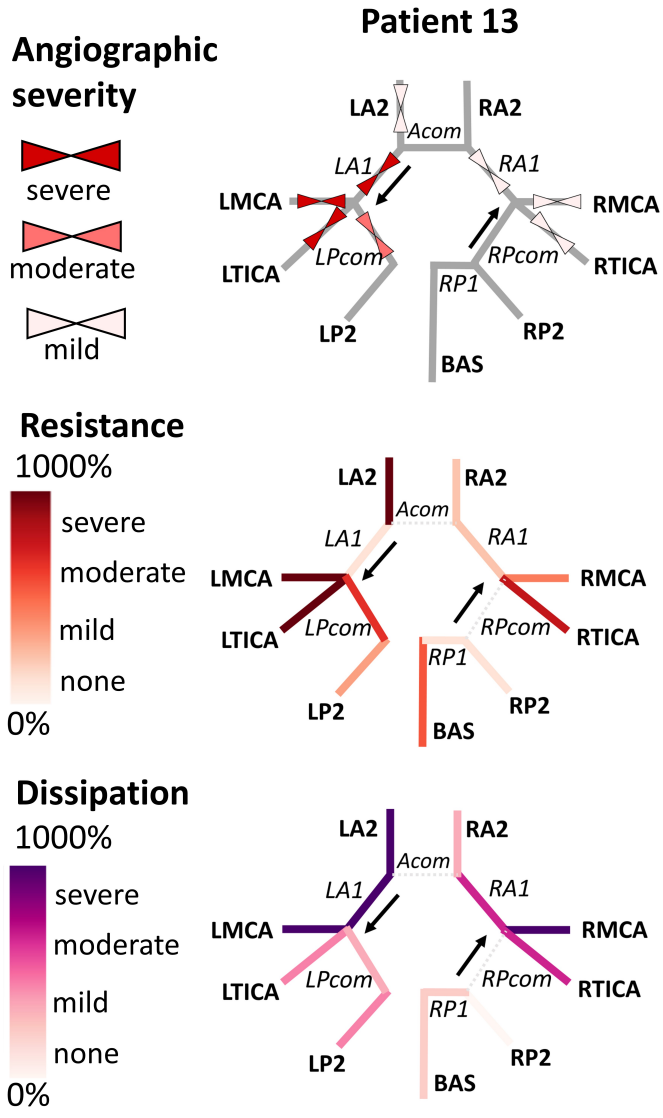

Figure 2.39: Patient 13 with vasospasm localized in two zones of the CoW with the angiographic severity (top), percent change in resistance (middle) and percent change in dissipation (bottom) in each vessel

Patient 15 had a complete CoW with a hypoplastic right Pcom. Vasospasm was localized in the anterior circulation with the right side exhibiting more severe vasospasm than the left side. The flow in the Acom changed from no net flow to left-to-right flow, which could be due to vasospasm being more severe on the right side. The posterior circulation was isolated from the right anterior circulation due to hypoplastic right Pcom.

Figure 2.41 shows two patients with vasospasm localized in two zones, as defined in section 2.2.18, with the same diagrammatic organization as in Figs. 2.33-2.40. Patient 16 is represented on the left side of the figure, and patient 17 is represented on the right side.

Patient 16 was missing a right A1 and had hypoplastic left Pcom and right P1. Vasospasm was localized to the left anterior and posterior circulations, though this effect may be overestimated by the fact that the right A1 was not present to contribute to the summation of vessel severities in the right anterior circulation. No changes in collateral flow directions were observed. The three zones were isolated from each other due to the missing or hypoplastic segments, which could limit the ability of any vessel from being recruited to supply any other zone via the collateral pathways. The resistance in the BAS was underestimated due to the effects of high curvature described in section 2.3.5, as well as due to focal stenosis.

Patient 17 had a complete CoW with a hypoplastic left P1 and right Pcom. Vasospasm was localized to the anterior circulation, more severe on the right side than on the left side. The collateral flow directions did not change. The posterior circulation was isolated from the anterior circulation via the hypoplastic left P1 and right Pcom, which might limit the ability of the posterior circulation to direct flow towards the anterior circulation in vasospasm, as already seen in patient 3.

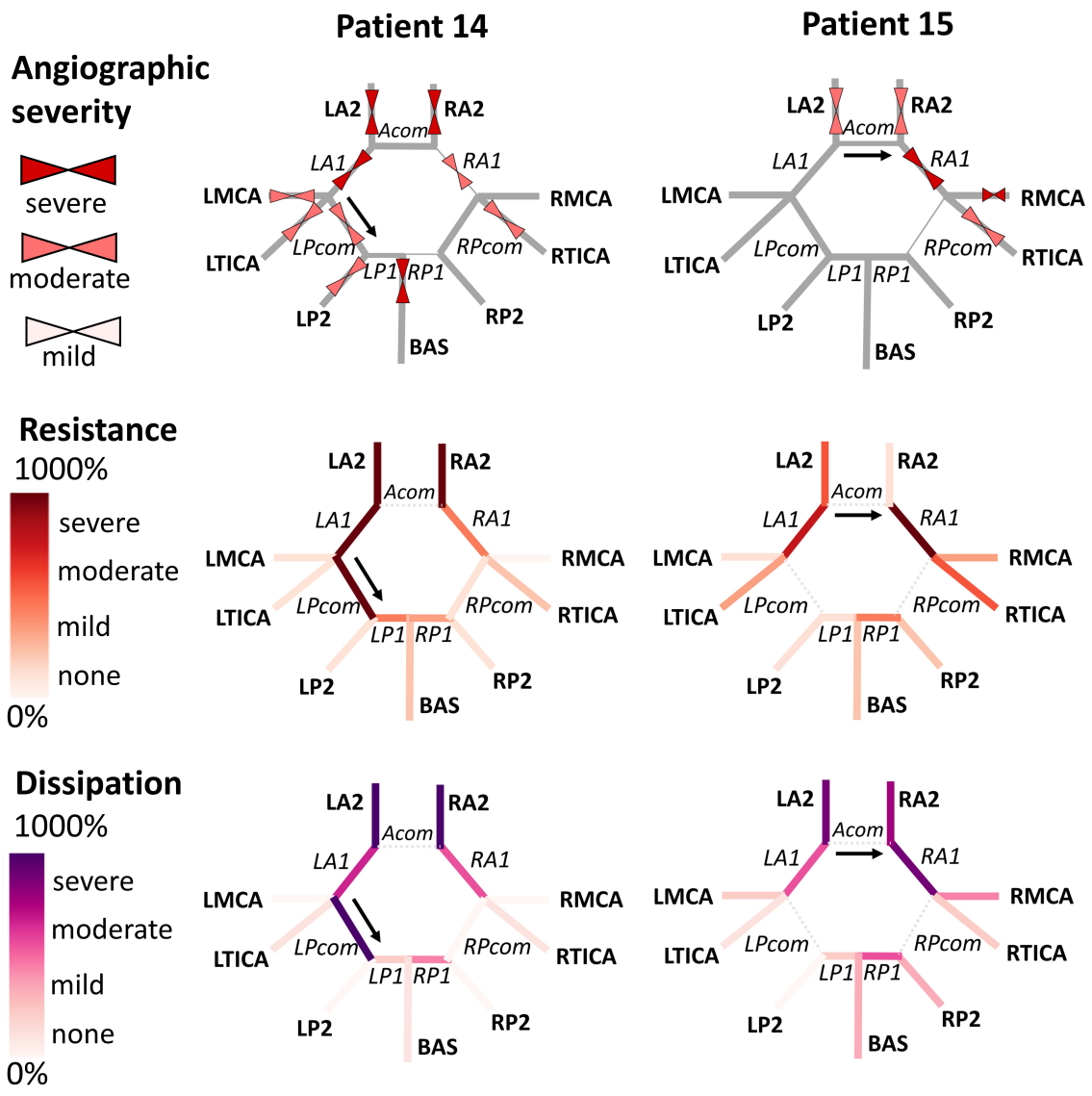

Figure 2.40: Patients 14 and 15 with vasospasm localized in two zones of the CoW with the angiographic severity (top), percent change in resistance (middle) and percent change in dissipation (bottom) in each vessel

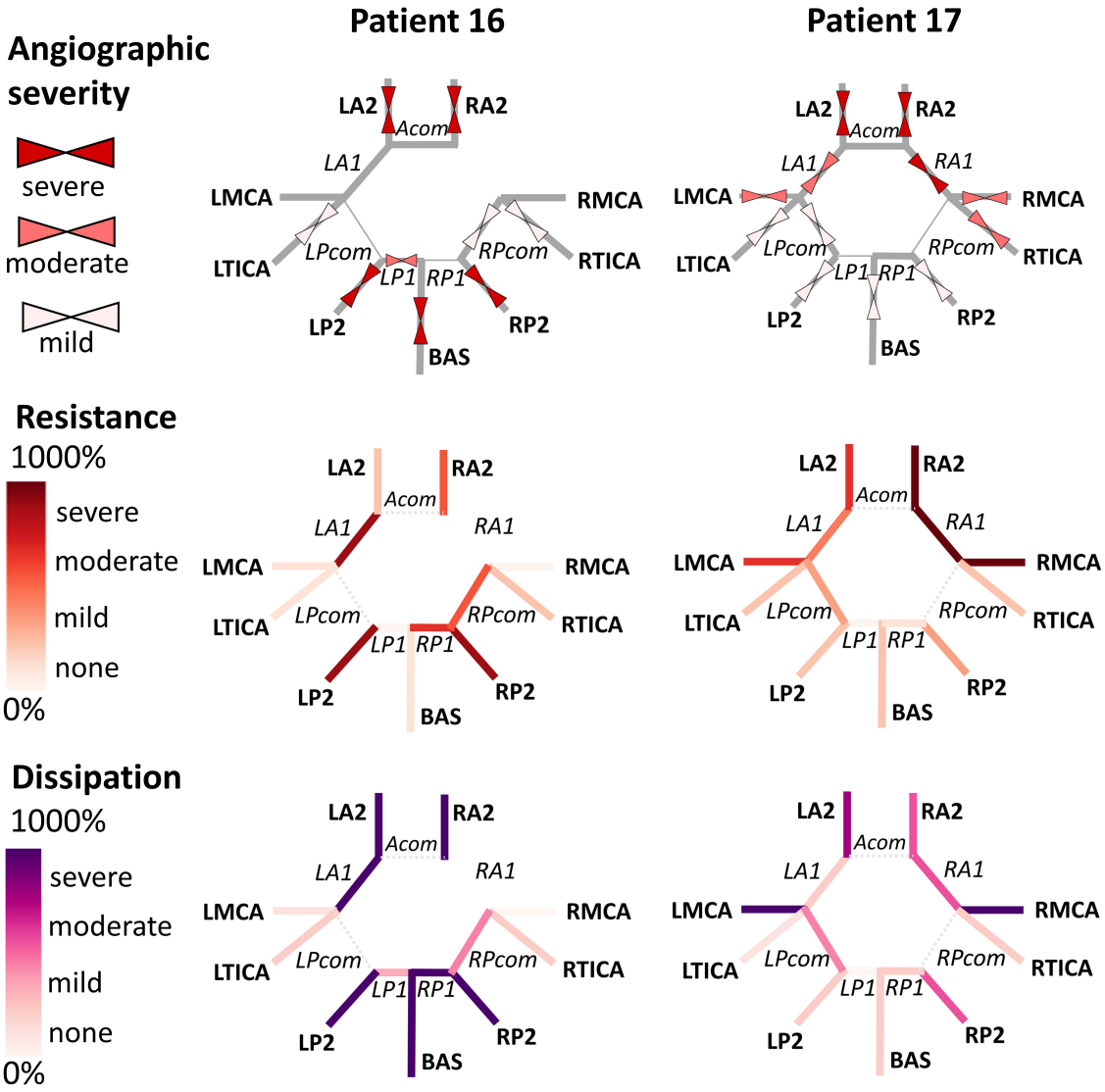

Figure 2.41: Patients 16 and 17 with vasospasm localized in two zones of the CoW with the angiographic severity (top), percent change in resistance (middle) and percent change in dissipation (bottom) in each vessel

2.3.13 Collateral Flow Changes in Patients with Balanced Vasospasm

Figure 2.42 shows two patients with vasospasm balanced across all zones, as defined in section 2.2.18, with the same diagrammatic organization as in Figs. 2.33-2.41. Patient 18 is represented on the left side of the figure, and patient 19 is represented on the right side.

Patient 18 had a complete CoW with no hypoplastic segments. Severe vasospasm was balanced between the three zones of the CoW. However, vasospasm in the BAS was more severe than the bilateral TICA, and the angiographic severity and resistance metric showed severe vasospasm in the bilateral P1 segments. The flow in the bilateral Pcoms changed from biphasic to antegrade, directing more flow to the posterior circulation potentially due to this severe basilar and bilateral P1 vasospasm. The Acom changed from strongly biphasic to weak right to left flow, with no clear mechanism to explain the change.

Patient 19 was missing a left Pcom. The CFD metrics showed moderate to severe vasospasm across all zones, but the angiography showed severe vasospasm localized in the right anterior circulation. Flow in the right A1 changed from antegrade to biphasic, and flow in the right Pcom changed from antegrade to largely retrograde. These flow direction changes are consistent with flow being directed to the right circulation in severe vasospasm, but the CFD metrics did not capture this phenomenon.

Figure 2.43 shows one patient with vasospasm balanced across all zones, as defined in section 2.2.18, with the same diagrammatic organization as in Figs. 2.33-2.42.

Patient 20 had a hypoplastic left Pcom, and severe vasospasm was balanced across the three zones and between the BAS and bilateral TICAs. Antegrade flow in the right Pcom noticeably strengthened during vasospasm, likely due to the flow limiting vasospasm observed in the DSA. However, the CFD did not replicate the significant change in the flow rate supplying the BAS.

Figure 2.44 shows two patients with vasospasm balanced across all zones, as de-

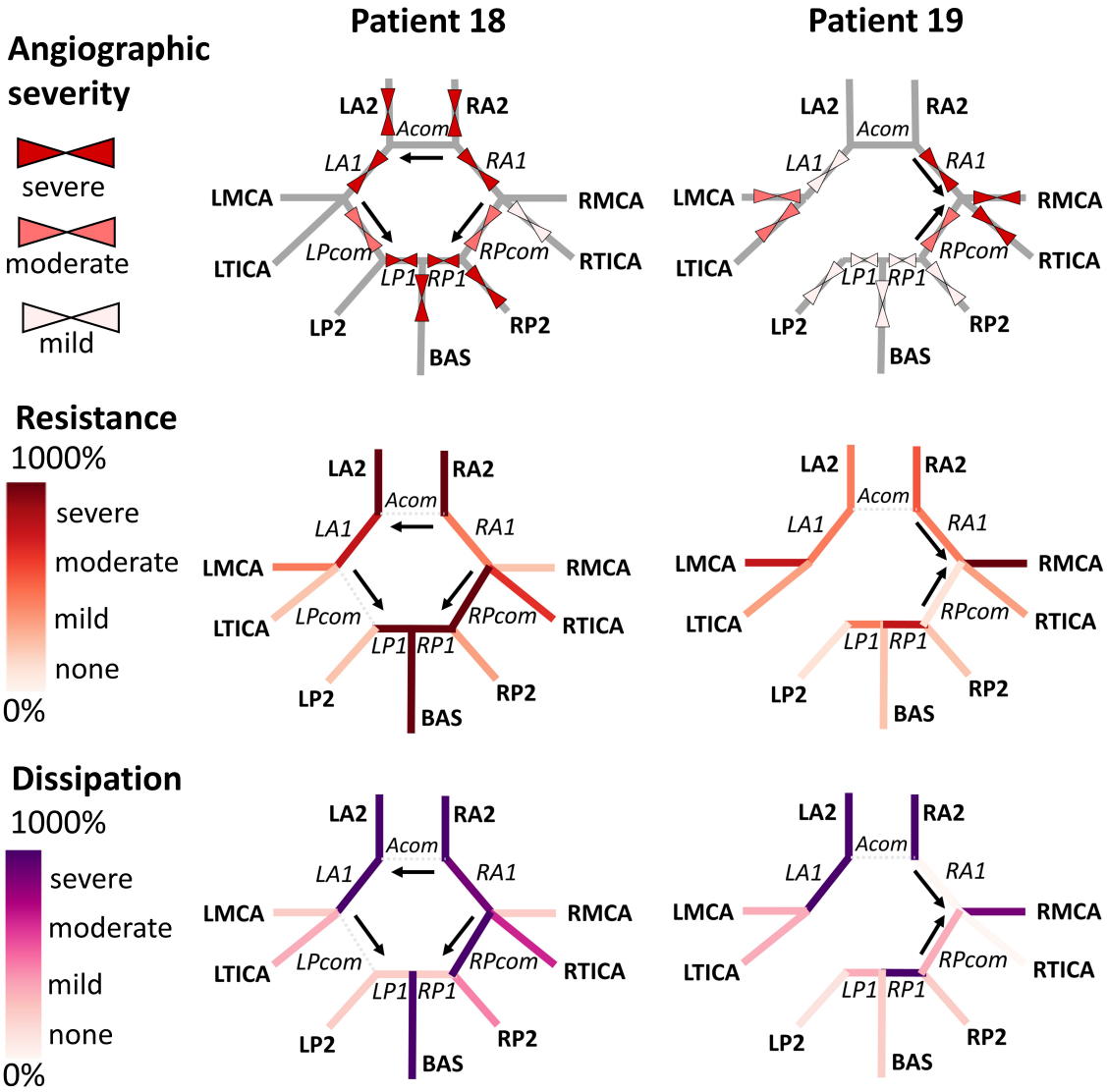

Figure 2.42: Patients 18 and 19 with vasospasm balanced across zones in the CoW with the angiographic severity (top), percent change in resistance (middle) and percent change in dissipation (bottom) in each vessel

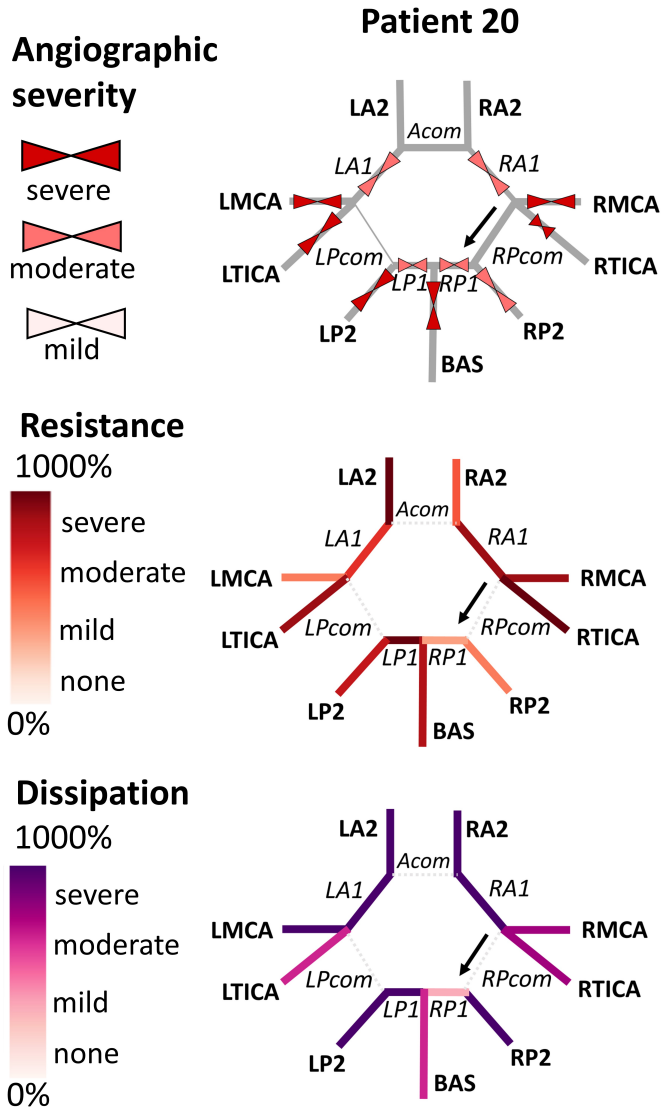

Figure 2.43: Patient 20 with vasospasm balanced across zones in the CoW with the angiographic severity (top), percent change in resistance (middle) and percent change in dissipation (bottom) in each vessel

fined in section 2.2.18, with the same diagrammatic organization as in Figs. 2.33-2.43. Patient 21 is represented on the left side of the figure, and patient 22 is represented on the right side.

Patient 21 was missing a left P1 segment, and severe vasospasm was balanced across the CoW. No changes in collateral flow direction were observed.

Patient 22 was missing a left P1 segment, and moderate to severe vasospasm was balanced across the CoW. No changes in collateral direction were observed.

2.3.14 Collateral Flow Changes in Patients with Mild Vasospasm

Figure 2.45 shows one patient with overall mild vasospasm, as defined in section 2.2.18, with the same diagrammatic organization as in Figs. 2.33-2.44.

Patient 23 was missing a right A1 segment and showed overall mild vasospasm across all vessels of the CoW. The flow in the left Pcom changed from retrograde to biphasic, but it was not a major collateral.

Figure 2.46 shows two patients with overall mild vasospasm, as defined in section 2.2.18, with the same diagrammatic organization as in Figs. 2.33-2.45. Patient 24 is represented on the left side of the figure, and patient 25 is represented on the right side.

Patient 24 had a complete CoW with a hypoplastic left Pcom and right A1, and presented with overall mild vasospasm. No changes in collateral flow direction were observed. Mild to moderate spasm was present in the left anterior circulation, but this zone was isolated from the posterior and right anterior circulation via the hypoplastic left Pcom and right A1 segments.

Patient 25 had a complete anatomical variation. No changes in collateral direction were observed. The angiographic severity was assigned as moderate in most vessels, but the CFD metrics did not show vasospasm, even moderate. However, angiography can overestimate vasospasm severity since it is assigned based on the degree of stenosis, and the DSA did not show any flow limiting vasospasm in the vessels.

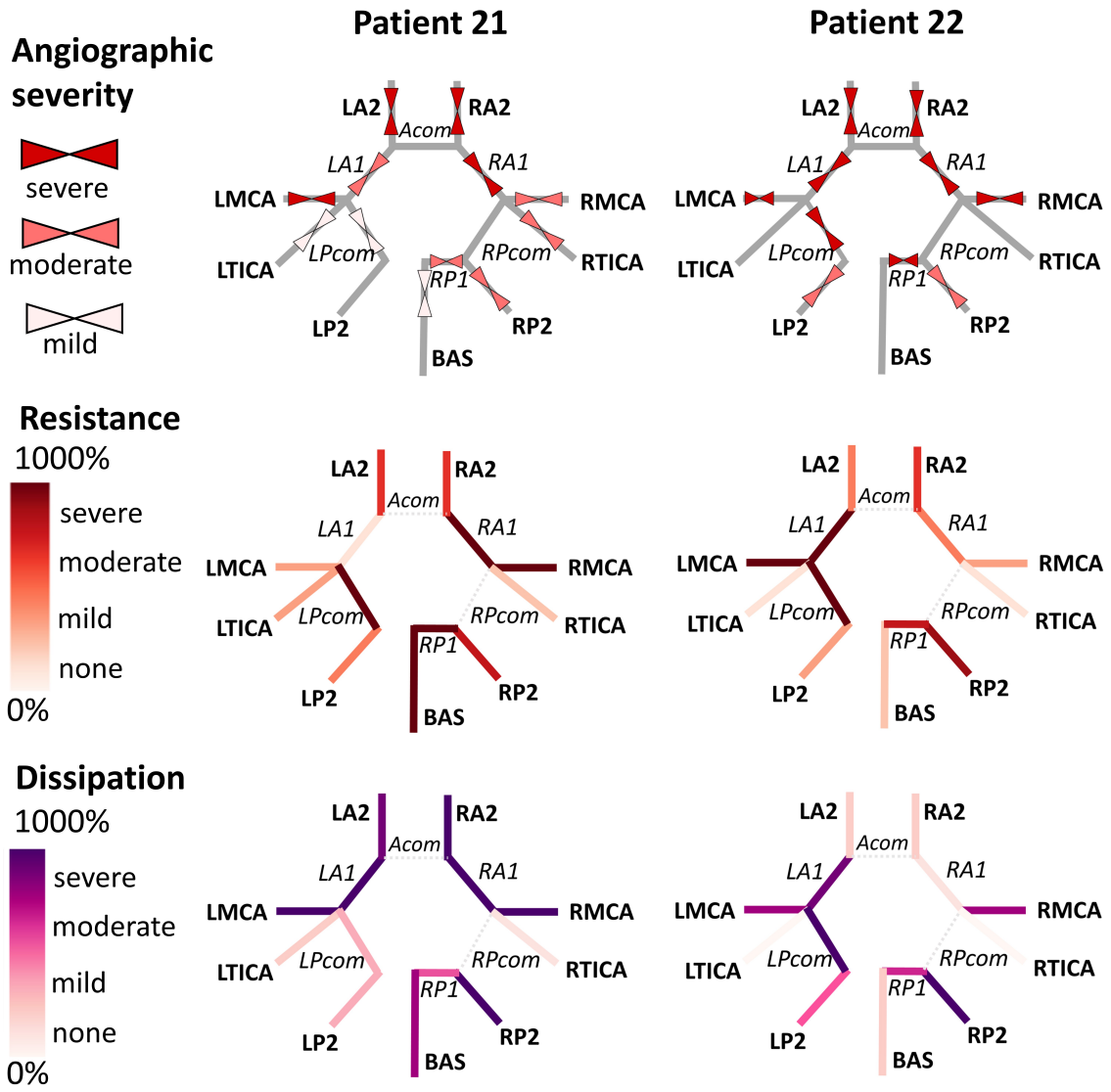

Figure 2.44: Patients 21 and 22 with vasospasm balanced across zones in the CoW with the angiographic severity (top), percent change in resistance (middle) and percent change in dissipation (bottom) in each vessel

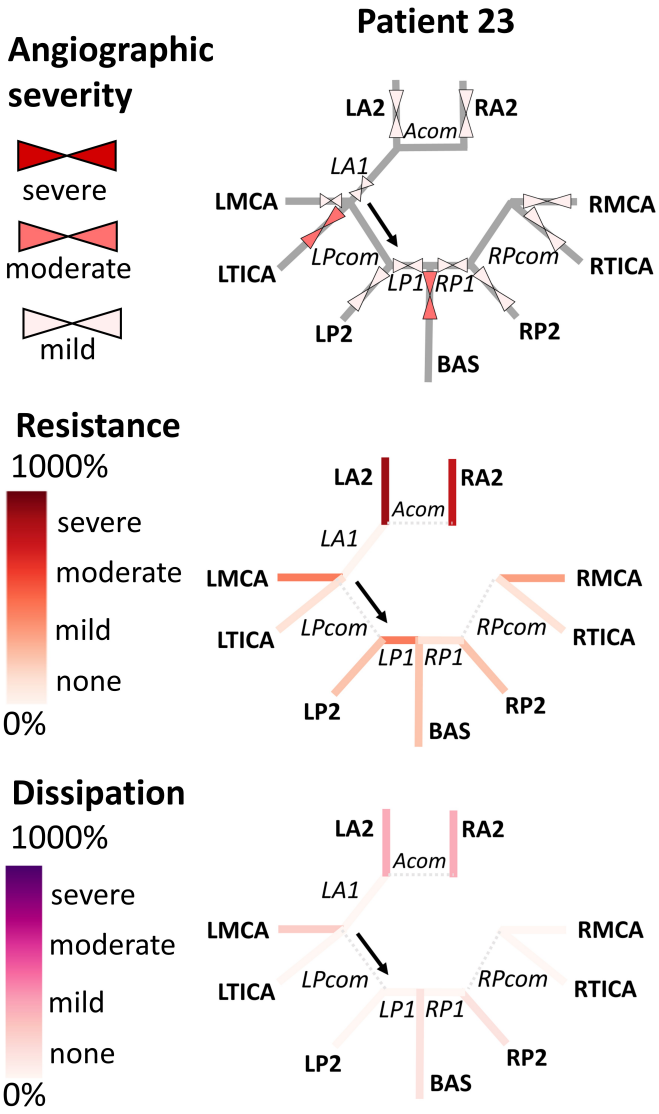

Figure 2.45: Patient 23 with mild vasospasm in the CoW with the angiographic severity (top), percent change in resistance (middle) and percent change in dissipation (bottom) in each vessel

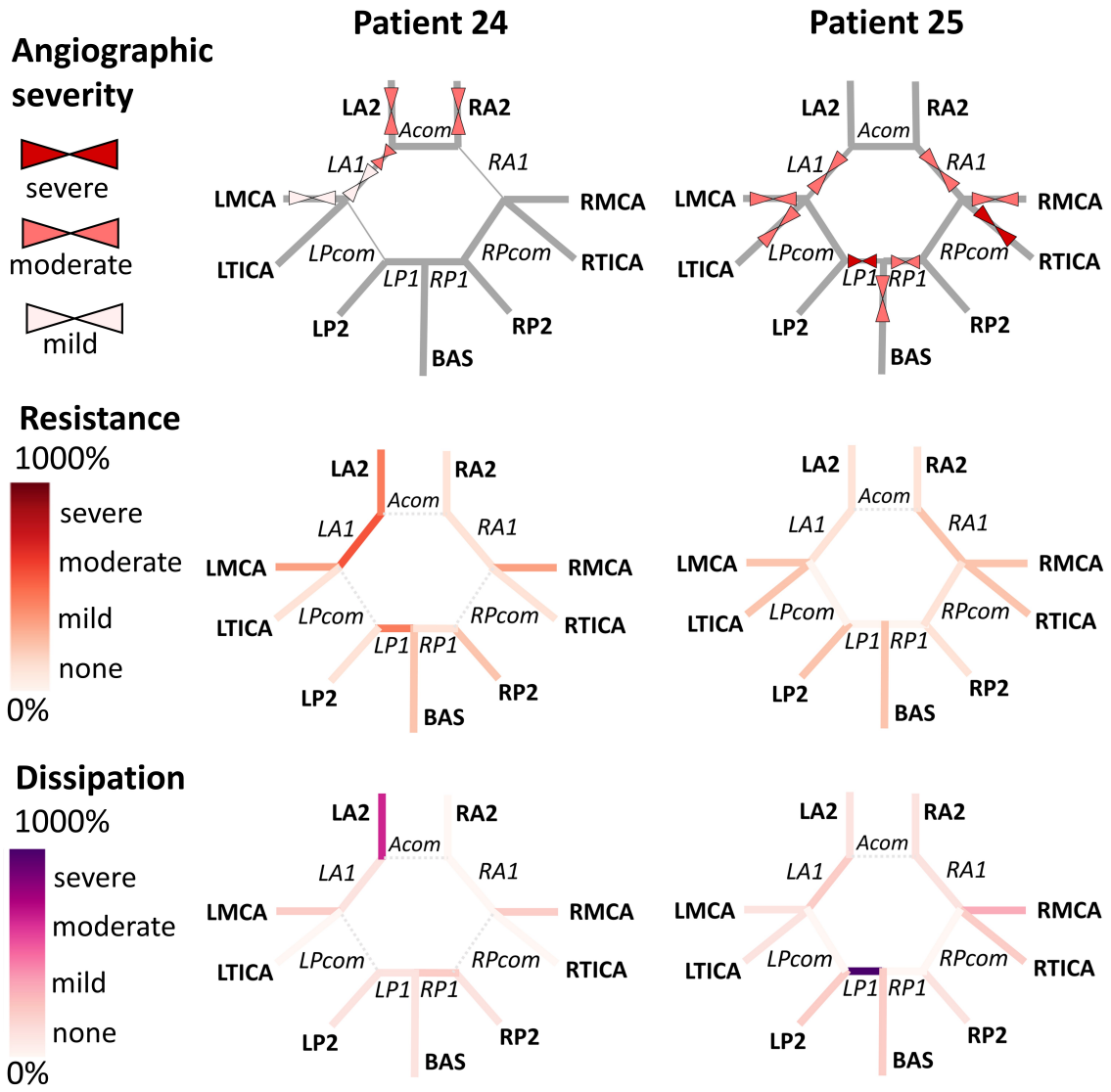

Figure 2.46: Patients 24 and 25 with mild vasospasm in the CoW with the angiographic severity (top), percent change in resistance (middle) and percent change in dissipation (bottom) in each vessel

2.4 Discussion

2.4.1 Comparison Between CFD Metrics and Angiographic Severity

Percent changes in resistance and dissipation were compared to the angiographic severity across all vessels in the cohort of 25 patients. Increasing percent changes in resistance and dissipation correlated strongly with increasing angiographic severity, as seen in Figures 2.30 and 2.31. There was much less variability in the CFD metrics for an angiographic severity of "none" than for an angiographic severity of "severe" (Fig. 2.30). Angiographic severity is determined qualitatively based on the degree of stenosis, but this stenosis may not result in significant hemodynamic changes in the CFD metrics, especially in the case of focal vasospasm. For percent changes in resistance or dissipation above 750%, 90% and 80% of vessels across all patients, respectively, had an angiographic severity of moderate or severe (Fig. 2.31); this demonstrates that the CFD simulations accurately captured severe vasospasm in those vessels.

The CFD metrics showed good agreement with the angiographic severity in each of the vessel segments analyzed (Fig. 2.32). Deviations from the angiographic assessment could be related to fundamental differences in the way that the severity is determined clinically versus computationally; angiographic severity is qualitatively based on degree of stenosis, while CFD measures changes in hemodynamics which are related to but not identical to the degree of stenosis. CFD metrics may differ from angiographic evaluations in vessels with high curvature, like the BAS, or due to impingement of jets at bifurcations, like near the Acom.

Disagreements can also originate from challenges associated with leveraging patient-specific clinical data. Smaller vessels can be more sensitive to CTA resolution. Coils or surgical clips used to treat aneurysms can result in artifacts in the CTA which can obscure some measurements of vessel diameter. The CTA, TCD, and DSA are not always collected on the same date. Early presentation of vasospasm can affect

baseline clinical data, though patients with vasospasm noted on the baseline DSA were excluded.

Fundamental challenges affect the assessment of the angiographic vasospasm severity in the DSA. The diameter of a vessel could be smaller during the baseline scan due to the anatomy of the patient's CoW. In this case, the clinician may note severe vasospasm in a segment when narrowing is observed in the vasospasm scan, but the CFD metrics will not detect large hemodynamic differences due to the similar diameters between the baseline and vasospasm anatomies. In the planar views of the DSA, vessels may overlap with each other, making it more challenging to identify the angiographic severity.

2.4.2 Clinical Studies of Collateralization in Vasospasm Patients

Previous clinical studies [6, 110, 161] have investigated the relationship between the degree of collateralization, the severity of vasospasm, and patient outcomes, as described in section 2.1.10.

The conclusions drawn from these studies are conflicting. Moftakar et al. and Topcu et al. suggest that the degree of collateralization could play a role in symptomatic vasospasm and the development of DCI, respectively, while Al-Mufti et al. did not find a relationship between degree of collateralization and patient outcome. These studies used scoring systems for the degree of collateralization that relied on observing the degree of perfusion in the downstream vasculature. Unlike many of the studies on the activation of collateral pathways during ICA occlusion and MCA stroke, these studies did not specifically examine the activation of the primary collaterals that compose the CoW.

My study complements existing clinical work by focusing on changes in the primary collateral pathways and how these changes might relate to the localization of vasospasm, overall severity, and the anatomical variation of the patient. The localization of vasospasm within the CoW has not previously been considered in these

clinical studies as a potential factor affecting patient outcomes.

2.4.3 Localization of Vasospasm

Localization of vasospasm in the left anterior, right anterior, or posterior zones was defined identifying imbalances in the contributions of each zone to the overall severity in the CoW. In patient 1 (Fig. 2.33) where vasospasm was localized in the right anterior zone, changes in flow direction in the left ACA A1 segment and in the Acom were observed. In patient 3 (Fig. 2.34), localization in both the left and right anterior zones could be related to changes in flow direction in the bilateral Pcoms and the left P1 segment. However, localization is not always associated with changes in flow direction, as shown by patient 2 (Fig. 2.33) and patient 4 (Fig. 2.34). Missing or hypoplastic segments in the CoW as well as vasospasm in collateral pathways might limit the ability of pathways to be recruited. Otite et al. found that cerebral autoregulation may be impaired after SAH [126], which may also affect the recruitment of collateral pathways.

In patient 5 (Fig. 2.35), vasospasm was balanced across the CoW and did not exhibit a change in collateral flow direction. Vasospasm was mild across the vessels in the CoW, which likely also played a role in the lack of changes in flow direction. While vasospasm was balanced within the CoW in patient 6 (Fig. 2.35), flow was directed in the left Pcom towards the BAS in severe vasospasm, while the bilateral TICAs were in moderate vasospasm. Imbalances in the supplying arteries severity may affect collateral flow direction changes in addition to localization within the CoW.

Patient 7 (Fig. 2.36) exhibited severe vasospasm balanced across the CoW. There were no significant changes in flow direction, which is likely due to the interplay of the vasospasm being balanced as well as the anatomical variation with the missing Acom and hypoplastic right Pcom.

Patient 8 (Fig. 2.36) showed localization of vasospasm in the left and right anterior zones, with the right anterior zone showing more severe vasospasm than the left

anterior zone. Despite changes in collateral flow direction in the left ACA A1 and Acom, infarct developed in a territory supplied by the left ACA A2 segment. This suggests that there could be a relationship between localization of vasospasm and infarct.

2.4.4 Severity of Vasospasm

Overall severity was determined by summing the severities determined by the CFD metrics across the major vessels of the CoW. In patient 5 (Fig. 2.35), the overall mild vasospasm could be a contributing factor to the lack of changes in collateral flow direction. In patient 7 (Fig. 2.36), most of the vessels exhibited moderate to severe vasospasm, and the patient developed multiterritorial infarct. This suggests that there could be a relationship between overall severity of vasospasm and the development of infarct. Topcu et al. found that patients with severe vasospasm were more likely to exhibit DCI [161], so this factor warrants further investigation.

2.4.5 Implications of Uncertainty of Clinical Data on CFD Results

Due to the retrospective nature of this study, the acquisition of clinical data did not always guarantee perfect agreement of the date of collection between the TCD measurements, CTA scan, and DSA. In future prospective studies, the data collection protocol should specify that all data be collected within a 24 hour period to eliminate some of the uncertainties introduced by this discrepancy.

Clinical data were acquired for the baseline condition upon admission for a subarachnoid hemorrhage and before the development of vasospasm, whereas the data used to benchmark the diameters, velocities, and flow rates were acquired in healthy patients. In the absence of stroke or vasospasm at the time of admission, the vessel calibers and brain perfusion are estimated to represent a baseline for the purpose of comparing against changes during vasospasm, compatible with measurements in a healthy patient.

Patients with aneurysms are often treated with surgical clips or coils. In the vasospasm CTA scan, these metal devices create artifacts that can obscure measurements of diameter in nearby vessels. The patients included in this cohort had identifiable patient anatomies despite these artifacts, though it remains a significant limitation of the model.

TCD measurements are collected by insonating a blood vessel with an ultrasound beam aligned as closely as possible with the centerline of the vessel. For measurements collected at high Doppler angles, the TCD reading could underestimate the velocity by a factor of $1/cos(\theta)$, where θ is the Doppler angle. The literature is not in agreement on whether velocity measurements from TCD and angle-corrected color duplex sonography are significantly different from each other [84, 101, 145]. In this study, the velocities were not angle-corrected because the uncertainty in the Doppler angle was too large, and the vessel flow rates fell within physiological ranges using the uncorrected TCD velocities, as seen in Figs. 2.25 and 2.26.

This study assumed that the maximum velocity from the TCD measurement corresponds to the centerline velocity of a symmetric Womersley profile. The velocity profiles in the major arteries could be asymmetric due to the tortuosity of the blood vessels. Therefore, some error could be introduced into the model by assuming a symmetric velocity profile. The sensitivity analysis accounts for all types of uncertainties, including the error of assuming a symmetric velocity profile. Flow extensions were added at the end of each artery where the symmetric Womersley profiles were applied as boundary conditions. These extensions ensured that the symmetric boundary conditions did not inhibit the development of asymmetric velocity profiles in the proximal locations of the CoW.

While this study does not include smaller vessels that branch from the CoW, like the anterior choroidal arteries and anterior inferior cerebellar arteries, these arteries are typically too weakly perfused to be segmented in the CTA scan. In addition, the literature indicates that these arteries are negligible in size and flow rate compared

to the SCAs and OAs [107, 119, 135] and thus have limited effect on intracranial hemodynamics [105].

During ICA occlusion or MCA stroke, retrograde flow in the OAs can help supply the CoW [44, 132]. The ophthalmic arteries are not insonated during vasospasm, i.e., the direction of flow during vasospasm is unknown. Additionally, flow reversal has not been documented in the literature in patients exhibiting vasospasm. Antegrade flow in the OAs was assumed.

Additional collateral pathways in the distal circulation such as the pial arteries can be recruited to maintain typical perfusion during ICA occlusion [19, 132] and stroke [40]. CTA scans and TCD velocity measurements, which could quantify the extent to which these collaterals are recruited during vasospasm, were not available. Therefore, the primary collateral arteries within the CoW were modeled exclusively.

This study was first-in-its-kind in assembling a cohort of 25 patients to perform CFD analysis for understanding vasospasm. However, due to the significant variability of anatomical variation and locations and severities of vasospasm, this work would benefit from a larger cohort of patients to investigate if there are statistically significant associations between factors identified in the CFD and clinical outcomes.

2.4.6 Computational Uncertainties in Patient-specific Modeling

For the sensitivity study in patient A with the complete CoW, the solution to the system of equations is not unique. The linear system of equations does not account for the differences in resistance between the collateral pathways, which could be significant in the presence of vasospasm. The resistance affects the flow distribution because it influences which pathways the blood preferentially takes. Therefore, the collateral flow rates calculated from this method deviated from the CFD flow rates. The percent differences were about 20 $\pm$ 10% for the larger flow rates and about 7 mL/min for the smaller flow rates. These percent differences in collateral flow rates fell within the uncertainties associated with the primary inlet and outlet flow rates

due to the pixelation of the CTA scans, as seen in Figs. 2.25 and 2.26. Meaningful trends during baseline and vasospasm could still be detected in the violin plots in Fig. 2.29. For the sensitivity study in the fetal PCA variation for patient B, the collateral flow rates found using the least-squares method agreed closely with the flow rates from the CFD. In some patients, the resistance between collateral pathways is considerably different due to their hypoplastic nature or severe vasospasm, in which case this sensitivity analysis based on the linear system of equations no longer applies.

The flow rates in the CoW are sensitive to changes in diameter. This can affect the calculation of resistance, which is the pressure drop normalized by the flow rate. The TCD measurements of velocity were taken without exact knowledge of the location of the sample volume in the vessel, with only the reported depth indicating an approximate location where the vessel was insonated. The measurements of diameter along the blood vessel can be variable, so challenges with matching the exact location of the TCD measurement with the corresponding diameter measurement could introduce uncertainty in the vessel flow rate. Benchmarking the diameters, velocities, and flow rates in each of the inlet and outlet vessels in the model helped ensure that the model parameters were physiologically realistic. Additionally, the directions and magnitudes of the flow in the collateral pathways from the DSA were compared to the CFD model to ensure that they were realistic for each patient.

2.5 Conclusions

This study developed novel techniques for leveraging CFD to study vasospasm in the entire CoW in a cohort of 25 patients. Patient-specific computational models were created by incorporating clinical data collected upon admission for SAH, corresponding to the baseline condition, and during vasospasm. CTA exams were segmented to create a model of the vasculature that accounted for the patient's anatomical variation, i.e., hypoplastic or missing segments, as well as narrowing due to vasospasm. TCD measurements of velocity were incorporated into the boundary conditions at

the major inlets and outlets. DSA provided information about the direction and magnitude of flow in the collateral pathways, as well as an angiographic assessment of vasospasm severity. Bayesian analysis used information about the uncertainties in the vessel diameters and velocities, as well as mass conservation, to identify optimal parameters that were applied as CFD boundary conditions. A sensitivity study demonstrated that the magnitude and direction of collateral flow rates were similar across different parameter sets, indicating that the trends in collateral flow rates seen in the CFD simulations are valid despite uncertainties in the input parameters.

High percent changes in resistance and viscous dissipation were correlated with angiographically severe vasospasm. Good agreement was demonstrated between the CFD metrics and angiographic severity in the different segments of the CoW. Localization of vasospasm was determined by calculating the contribution of each zone – left anterior, right anterior, and posterior – to the overall severity of the vasospasm in the patient's CoW. Some patients demonstrated significant changes in the direction and magnitude of the collateral flows due to localization in one or two zones, while others did not show this behavior. Changes in collateral flows are likely a result of the complex interplay between localization of vasospasm, overall severity, and the anatomical variation. Infarct due to vasospasm was confirmed in two patients, one of which showed high overall severity and one of which showed high severity localized in the anterior circulation. Future work could systematically review MRI exams post-vasospasm to detect infarct and determine if there is a relationship between the development of infarct and the overall severity or localization of vasospasm.

2.6 Future Work

This study presented a novel technique for studying the effects of vasospasm on collateral flows in a cohort of 25 patients. The patients included in the cohort represented a diverse set of anatomical variations due to hypoplastic and missing segments along with varying locations and severities of vasospasm in the vessels of the CoW. Expand-

ing the cohort to include more patients could help identify trends more clearly, across diverse cases, and perform statistical analysis.

The present study focused on understanding the relationship between the locations and severities of vasospasm and anatomical variation and the changes in flow in the collateral pathways. Understanding risk factors for infarct is of particular clinical interest. Some of the key challenges to more systematically reporting whether infarct developed in this cohort of 25 patients was the lack of consistency for type of scan and delay following vasospasm when that the scan was collected, as well as interobserver variability in the diagnosis of the presence of vasospasm and determination of the origin of infarct . Prospective studies could more systematically collect a post-vasospasm MRI to determine the presence of infarct, and procedures could be put in place to confirm the presence and origin of infarct across observers. As identified in this study, two potential factors of interest to correlate with the development of infarct could be the overall severity and the localization of vasospasm within the CoW.

One of the key challenges in this study is the limited resolution of the CTA for creating patient-specific segmentation. Other studies of cardiovascular flows have leveraged 3-dimensional DSA – a higher resolution scanning technique than CTA - to create segmentations. In the current clinical protocol for DSA collection, images from 3-dimensional DSA are not collected for all injections, typically only for the injection for measuring the aneurysm to plan treatment. Prospective studies could collect and store 3-dimensional DSA to create patient-specific segmentations.

Chapter 3

PLATELET ACTIVATION IN THE LEFT VENTRICLE IN THE PRESENCE OF A LEFT VENTRICULAR ASSIST DEVICE WITH SPEED MODULATION SYNCHRONIZED WITH THE CARDIAC CYCLE

3.1 Introduction and Background

3.1.1 Heart Failure

Heart failure affects 6 million Americans [162], with about 5% of those cases representing advanced heart failure [98]. In about 50% of heart failure patients, the ejection fraction is reduced, which can have implications for the degree of physical activity patients can engage in. The American Heart Association grades the stages of heart failure: stage A as at risk for heart failure, stage B as pre-heart failure, stage C as symptomatic heart failure, and stage D as advanced heart failure. In patients with stage C or stage D heart failure, the New York Heart Association Functional Classification further discriminates patients based on their symptoms: class I as no physical limitation, class II as slight physical limitation, stage III as marked physical limitation, and stage IV as symptoms of heart failure at rest [2].

Heart failure in the left ventricle (LV) can have different origins. Dilated cardiomyopathy is characterized by dilation of the LV and thinning of the ventricular wall, impairing contractility and resulting in reduced ejection fraction [1]. Hypertrophic cardiomyopathy originates from thickening of the ventricular wall, increasing the stiffness and reducing the amount of blood filling in and ejecting from the LV [1].

Early stages of heart failure can be treated medically with neurohormonal antagonists and other non-invasive measures [98]. However, patients with stage D heart

failure with reduced ejection fraction may not be responsive to these techniques. These patients are evaluated for cardiac transplant, and patients with significant co-morbidities are excluded from consideration [98]. As a bridge or alternative to heart transplantation, left ventricular assist devices (LVAD) were developed. Third generation LVADs are centrifugal pumps that are implanted in a failing LV to deliver typical perfusion to the body. Due to the limited supply of heart transplants – about 2500 per year compared to the 4000 patients on the transplant list [98] – LVADs are increasingly implanted in advanced heart failure patients [172] as a bridge-to-transplantation or destination therapy [82].

3.1.2 Left Ventricular Assist Device (LVAD)

The LVAD is implanted in the ventricular apex by inserting the inflow cannula in the LV to bring flow into the pump (Fig. 3.1). Blood flows through the pump and is directed to the aorta through the outflow graft.

First-generation LVADs were volume displacement pumps, consisting of unidirectional inlet and outlets valves and driven by a pulse generator [97]. This initial design was vulnerable to mechanical failure [87] due to wear on moving parts, and the large size of the device limited the pool of potential recipients [26]. Second-generation LVADs, in contrast to first-generation pumps, use axial flow rotary pumps to deliver continuous flow [97]. Rates of pump replacement decreased [153], and more patients could be served by the smaller design [26]. However, due to the high rotational speeds of the impeller, blood was subjected to unphysiological conditions, leading to hemolysis (red blood cell death) and thrombosis (aggregation of platelets, plasma proteins and red blood cells into a blot clot) [123]. In-pump thrombosis is a major complication, so clinicians manage the risk through anticoagulation therapy and speed management [97]. Third-generation pumps leverage magnetic or hydrodynamic bearings in a centrifugal pump design, which allows the impeller to be suspended in the pump [87]. Decreasing the contact between mechanical parts, and reducing the rotational

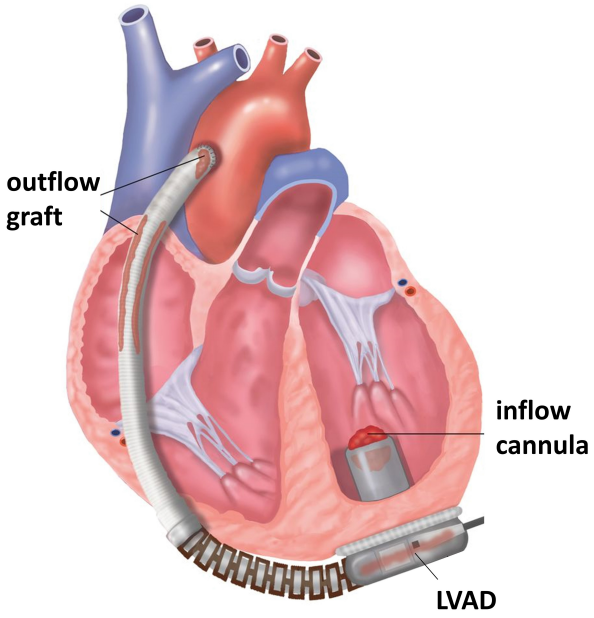

Figure 3.1: Left ventricle with a left ventricular assist device (LVAD) implanted

speed of the pump impeller increases durability and enhances pump biocompatibility [87]. While third generation pumps have significantly decreased the rate of in-pump thrombosis [106], stroke risk has not decreased significantly [88].

Centrifugal pumps are sensitive to pre-load – the pressure upstream of the pump in the left ventricle – and after-load – the pressure downstream of the pump in the aorta, i.e., the mean arterial pressure. The head is defined as the difference between the after-load and pre-load. Flow through LVADs is governed by their characteristic pressure vs flow rate curve (Fig. 3.2), where decreases in head at a given flow rate result in increases in flow rate. The pump speed is optimized for each patient via a ramp study to maximize ventricular unloading while decreasing complications like right ventricular and aortic valve insufficiency [120].

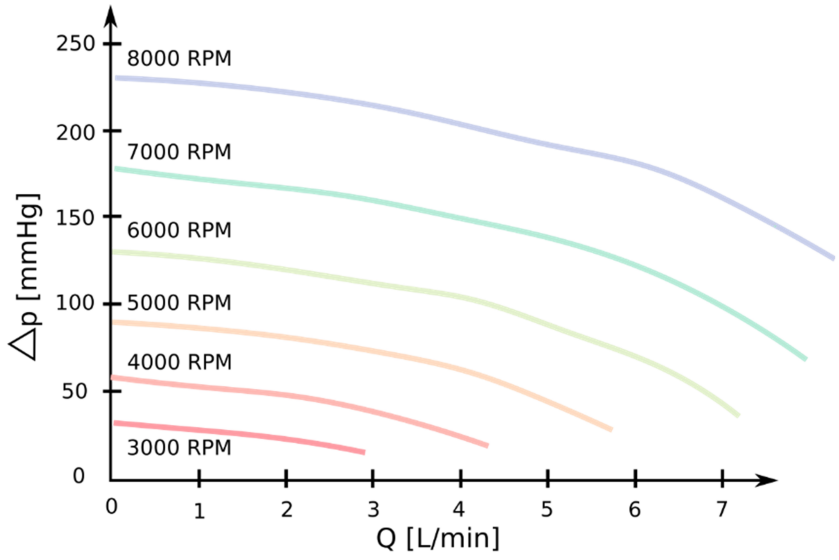

Figure 3.2: Head (mmHg) versus flow rate (L/min) curve for the HeartMate 3 at different rotational speeds (RPM)

3.1.3 LVAD Pulsatility Mode

Two third-generation pumps were approved by the FDA and widely used in clinical care: the HeartMate 3 (Abbott, St. Paul, MN) and the HVAD (Medtronic, Minneapolis, MN). The HVAD was withdrawn from the market in 2022. These designs incorporated a pulsatility mode that periodically modulates the impeller speed to promote in-pump washout and decrease the risk of thrombosis. HeartMate 3 modulates the speed every 2 seconds for 0.35 seconds, decreasing the speed by 2000 RPM and then increasing it by 2000 RPM before returning to the baseline speed [22]. HVAD used the Lavare cycle, which modulated the speed every 60 seconds, reducing the speed by 200 RPM for 2 seconds and then increasing the speed by 400 RPM for 1 second before returning to the baseline speed [85].

Previous studies investigated the effect of the speed modulation on intraventricular [30, 31, 76, 90, 103, 176] and in-pump [21, 49, 166] washout using CFD simulations [21, 49, 90, 103, 166] and particle image velocimetry (PIV) experiments [30, 31, 76,

176]. Clinical studies have examined the relationship between pump pulsatility and stroke risk [42, 88, 114, 154, 176].

Preserved native contractility is observed in some patients, enhanced by LVAD therapy through unloading of the LV. The cyclic contraction and relaxation of the left ventricle makes the pre-load on the pump time dependent, altering the flow rate. The pulsatility modes are currently programmed to occur independently of the cardiac cycle of the heart. The role of temporal synchronization of the pulsatility mode with the cardiac cycle is an active area of research [30, 76, 90, 103].

3.1.4 The Role of Altered Intraventricular Hemodynamics on Thrombosis

Thrombosis is the formation of a blood clot triggered by the aggregation of activated platelets. Platelet activation is mediated by complex chemical interactions known as the coagulation cascade [43]. Unphysiological hemodynamic conditions can lead to platelet activation, thus increasing the risk for thrombosis. Stasis is a primary risk factor for thrombus formation [94], in agreement with Virchow's triad. Experimental studies showed that elevated stresses for extended periods of time activate platelets [70, 130, 148].

In LVAD patients, thrombus formation can occur within the pump [122], the outflow graft [14], or the left ventricle (LV) [27, 48, 52, 58, 102, 152]. The presence of an LVAD significantly changes the hemodynamics in the LV. A strong jet that connects the mitral valve and the inflow cannula produces flow separation and recirculation along the LV wall [31, 125, 139], promoting stasis. Additionally, low velocities have been observed in the apical pocket around the inflow cannula [31, 164]. Vortical structures formed during diastole in healthy patients that improve intraventricular washout are interrupted by the presence of the LVAD [5]. Continuous pump flow in combination with reduced native contractility can result in permanent aortic valve closure [72, 151] or intermittent opening [41], resulting in stasis in the left ventricular outflow tract (LVOT). Thrombus formation in these regions of stasis – the apex near

the inflow cannula [48, 58] and the LVOT [27, 48, 52, 102, 152]– has been clinically observed.

Platelet activation is not only related to the degree of stasis, but also to the shear stresses experienced by the platelets as they flow in the LV. Computational studies have incorporated this risk factor for platelet activation by modeling the shear stress history, which measures the accumulated shear stress over time [8, 36, 37, 38, 39, 57, 99].

3.1.5 Study Overview

This study investigated the relationship between the temporal synchronization of the HeartMate 3 pulsatility mode with the native cardiac cycle and the intraventricular hemodynamics that influence platelet activation. Four timings of the pulsatility mode with respect to the cardiac cycle were compared to determine the optimal configuration for promoting intraventricular washout.

CFD simulations in a patient-specific LV capture the three-dimensional flow fields, and the results were compared to flow fields at two orthogonal planes from PIV experiments [30]. Lagrangian particle tracking simulated the platelet behavior in the flow, with residence time and shear stress history as metrics for potential platelet activation. Virtual angiography identified regions of stasis by injecting virtual contrast into the LV and tracking the degree of washout. Stagnation index, an Eulerian metric for stagnation, was computed and compared to PIV results.

Section 3.2 outlines the methodology for creating the CFD simulations. Sections 3.3.1-3.3.2 compare results from the CFD to the PIV experiment. Sections 3.3.3-3.3.5 present results that were uniquely discovered using the CFD methodology. Section 3.4 analyzes in more detail the presented results and limitations of the study.

3.2 Methodology

3.2.1 Computational Domain

A patient-specific LV model was created from the anatomy for a patient with dilated cardiomyopathy. A previous experimental study created a rigid silicone flow phantom of the LV geometry and inserted an LVAD cannula into the apex of the LV model [30]. A contrast tomography (CT) scan (North Star Imaging, X5000) was performed of the flow phantom to match the exact configuration of the cannula insertion between the computational model and the experiment. The images from the CT scan, with a resolution of 85 µm, were segmented to produce the computational geometry seen in Fig. 3.3. The geometry was smoothed to avoid sharp corners and small geometric features that would decrease the quality of the computational mesh. Flow extensions were added to the inflow through the mitral valve and the outflow through the LVAD cannula. The aortic valve was modeled as closed, as is common for patients with an LVAD [72, 151].

3.2.2 Mesh

A computational mesh was generated with tetrahedral elements and four prism layers near the ventricular walls. A grid independence study was performed by comparing the results from three meshes with tetrahedral base sizes of 3 mm, 1.5 mm, and 1 mm corresponding to 0.8, 1.9, and 2.8 million elements. Spheres with a radius of 2mm were created in the apex, LVOT, and shear layer, and the velocities were spatially averaged within each sphere. In the shear layer and apex, the velocity magnitudes in the mesh with a base size of 1.5 mm agreed within 5% of the mesh compared with a base size of 1 mm. In the LVOT, the velocity magnitudes in the mesh with a base size of 1.5 mm were within 0.12 mm/s of those in the mesh with a base size of 1 mm. Therefore, the results for a base size of 1.5 mm were considered converged and selected for the final analysis. A customized zone near the cannula tip with finer mesh sizing

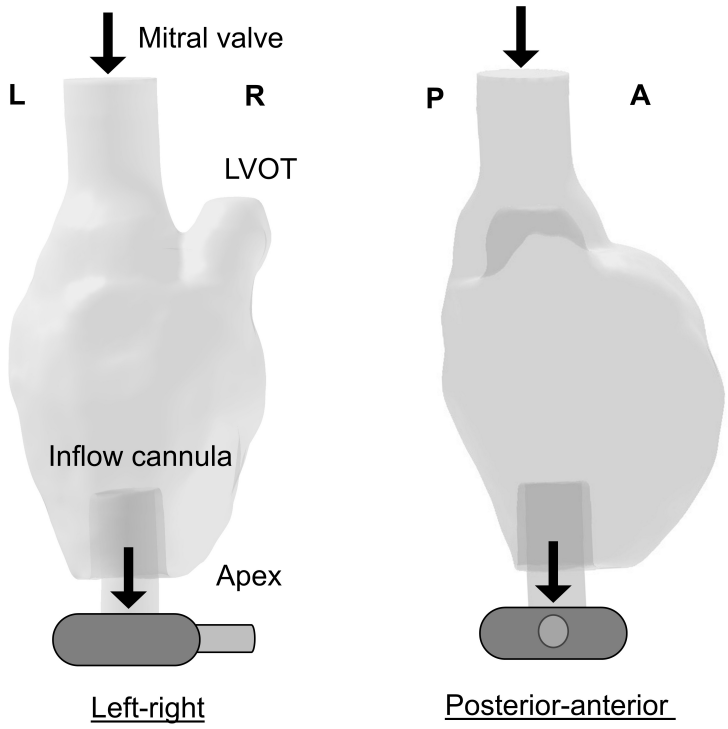

Figure 3.3: Computational domain for a patient-specific ventricle implanted with an inflow cannula with the mitral valve as the inlet and inflow cannula as the outlet in the left-right view (left) and posterior-anterior view (right)

(0.375 mm) and only one boundary layer element was used to avoid the numerical challenges arising from the Lagrangian particles interacting with the geometry of the cannula's sharp edges.

3.2.3 Boundary Conditions

In a previous PIV experiment [30], a HeartMate 3 device was connected to the rigid LV flow phantom through a silicone inflow cannula (Fig. 3.3), and an ultrasonic flow meter (Transonic, Ithaca, NY, USA) measured the time-resolved flow rate through the LV. The flow rate varied in time due to interaction of the cardiac cycle (period of 1 second) with the HeartMate 3 pulsatility mode that occurs every 2 seconds, resulting in flow rates plotted in Fig. 3.4b. The HeartMate 3 pulsatility mode was synchronized with four different times during the cardiac cycle: systole, peak systole, diastole, and peak diastole (Fig. 3.4a), corresponding to increasing intraventricular pressure (IVP), highest IVP, decreasing IVP, and lowest IVP, respectively. The time-resolved flow rate acquired from the ultrasonic flow meter for each of the four timings [30] was imposed as the outlet boundary condition of the domain at the LVAD cannula.

This study uses flow conditions for a pump speed of 5200 RPM, resulting in an average flow rate of 4.6 L/min, for the four timings in Fig. 3.4a. The flow rates measured from the PIV experiment were converted into a time-varying Poiseuille profiles prescribed at the end of the LVAD inflow cannula. The mitral valve was prescribed as a pressure inlet, and the LV walls were modeled as rigid.

3.2.4 Computational Fluid Dynamics Simulations

The Navier-Stokes equations were fully resolved without modeling [56], using the finite volume solver ANSYS Fluent 18.1 (ANSYS, Cannonsburg, PA). Blood was modeled as an incompressible, Newtonian fluid with a viscosity of 0.0038 $Pa \cdot s$ and density of 1050 kg/m^3. The residuals were set to $1x10^{-4}$ for mass conservation and $1x10^{-6}$ for the three components of velocity. The pressure-implicit with splitting of operators

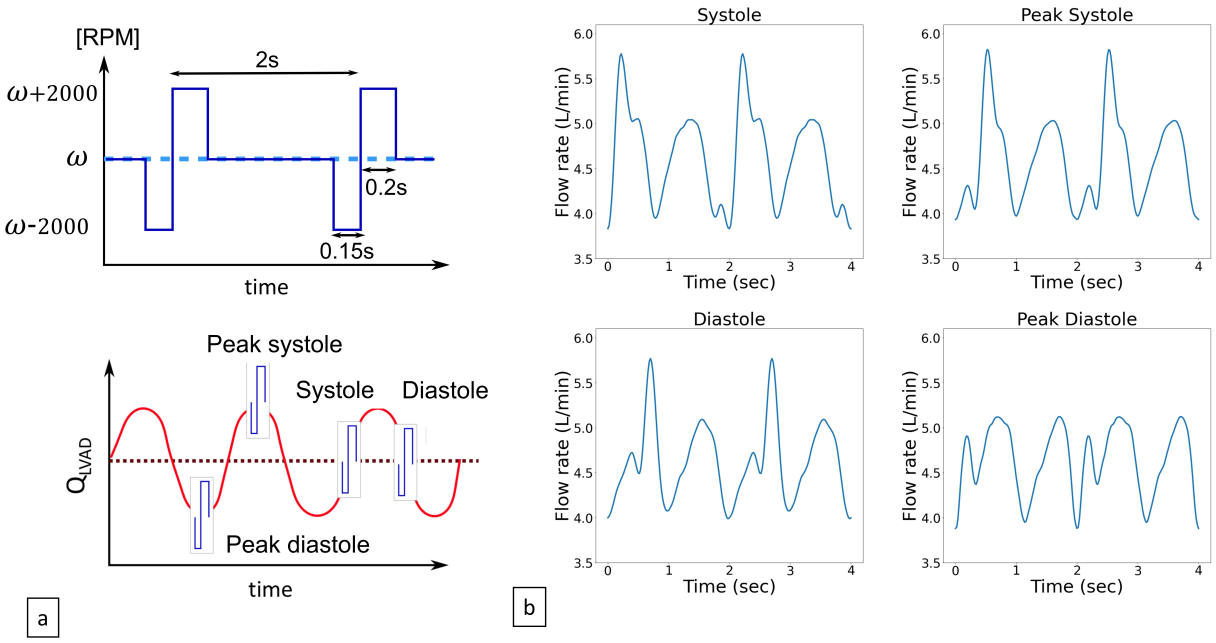

Figure 3.4: The HeartMate 3 pulsatility mode (a) modulates the pump speed every 2 seconds and is synchronized with the cardiac cycle at peak diastole, peak systole, systole, or diastole (b) resulting in different flow rate profiles over time

pressure–velocity coupling scheme, with second-order pressure and momentum spatial discretization and second-order implicit time discretization, was employed. The second order time-dependent solver used a time step of 0.1 ms and ran for 48 seconds of physical time, corresponding to 48 cardiac cycles, with the first 8 seconds excluded to eliminate transient behavior influenced by the initial condition. The simulations ran for about 15 days of wall-clock time on four nodes with 28 processor dual Intel Xeon CPUs of the Hyak Supercomputer at the University of Washington.

3.2.5 Comparison with Particle Image Velocimetry Experiments

The stereoscopic PIV experiment measured the three components of the velocity at two orthogonal planes in the LV – the left-right plane and the posterior-anterior plane (Fig. 3.3) - aligned with the center of the inflow cannula. The laser sheet for the PIV data collection had an approximate thickness of 5 mm. The CFD velocities were extracted at a plane aligned with the cannula centerline and two planes offset by 2.5 mm on either side. The velocities across these three planes were averaged together to form a more realistic comparison with the PIV. The velocities from the PIV data were extracted within a rectangular region of interest at the center of the ventricle that encloses the jet and a region off-axis of the jet, and the corresponding CFD velocities were interpolated onto a grid with the same number of data points as the PIV. Bland-Altman plots compared the differences in velocities between the PIV and CFD, and the median and 95% confidence intervals were identified.

3.2.6 Virtual Angiography

A virtual angiogram was performed by injecting virtual contrast into the mitral valve, solving the advection-diffusion equation [128, 131]. Contrast was injected over 8 seconds to fill the LV by assigning a non-zero concentration at the mitral valve. After 8 seconds of filling, the boundary condition at the mitral valve was assigned to zero concentration, representing fresh blood introduced to the LV. Washout was tracked

for 32 seconds, with old blood exiting through the LVAD inflow cannula. Areas with higher concentrations of contrast represented pockets of stagnating blood. The concentration of virtual contrast was integrated over the entire LV and normalized by the total integrated value after 8 seconds of injection to generate a non-dimensional metric for washout. An exponential function was fit to the decay of contrast concentration with time:

$$y = e^{-t/t_d} \tag{3.1}$$

where t is the instantaneous time and t_d is the exponential decay time constant.

3.2.7 Stagnation Index

Areas of high stagnation are correlated with increased risk of thrombogenicity. The stagnation index was developed by Wong et al. [170] as a spatially-varying Eulerian metric for blood residence time, defined as:

$$SI(x,y) = \sqrt{\frac{A_{LV}T}{\int_0^T |v(x,y)|^2 dt}} \tag{3.2}$$

where A_{LV}, represents the characteristic area, T represents the time period, and $|v(x,y)|$ represents the three-dimensional velocity magnitude.

The square of the velocity magnitude was integrated over a period of 8 seconds. The characteristic area was chosen as the area of the measurement plane, i.e., left-right plane or posterior-anterior plane. A high stagnation index, measured in seconds, represents an area of local stagnation that could be a risk factor for thrombosis.

3.2.8 Lagrangian Platelet Model

The motion of platelets transported in the transient flow were modeled using inertia-less tracer particles tracked over 40 cardiac cycles via Lagrangian tracking. Particles were injected through the mitral valve and tracked in the LV until they exited through

the LVAD inflow cannula. Two thousand particles were injected every 0.05 seconds over 4 seconds for a total of 160,000 particles.

The hemodynamic environment experienced by the platelets can lead to their activation [70, 94, 130, 148], which can increase the likelihood of thrombus formation. Because a high degree of stasis is a risk factor, the residence time (RT) of the platelets was quantified:

$$RT = T_i^{exit} - T_i^{entrance} \tag{3.3}$$

where $T_i^{entrance}$ is the time at which a particle with index i was injected at the mitral valve and T_i^{exit} is the time at which the particle exited the LV through the inflow cannula.

Platelets exposed to high stresses over time can become activated, so the shear stress history (SSH) of the platelets was calculated with:

$$SSH = \int_{t_0}^{t} \tau(X(t'), t')dt' \tag{3.4}$$

where τ is the instantaneous shear stress experienced at time t' by the platelet at location $X(t')$, t_0 is the time of particle injection, and t is the instantaneous time in the particle trajectory.

The time-averaged stress (SS_{ave}) is calculated with:

$$SS_{ave} = \frac{SSH}{RT} \tag{3.5}$$

The distributions of RT, SSH, and SS_{ave} are represented with boxplots, where outliers exceed the third quantile by 1.5 times the interquartile range and are identified with crosses.

The number of particles at each time during the washout phase is normalized by the total number of particles present after 4 seconds of injection (about 80,000)

to calculate the fraction of particles over time. An exponential function was fit to calculate the characteristic decay time (Eqn. 3.1).

3.3 Results

To illustrate the velocity fields (section 3.3.1), stagnation index (section 3.3.2), and virtual angiography (section 3.3.3), results from the timing of the pulsatility mode with systole are plotted. In section 3.3.4, the computational results are compared between timings of the pulsatility mode with the cardiac cycle. In section 3.3.5, the results from the Lagrangian particle tracking are presented and discussed.

3.3.1 Velocity Fields

The velocity magnitude and in-plane velocity direction (vectors) for the PIV experiments and CFD simulation at two orthogonal planes for the pulsatility mode synchronized with systole are presented in Fig. 3.5.

For both views, the PIV and CFD results show good agreement for both the direction and magnitude of the flow. A strong jet forms between the mitral valve and inflow cannula. During the speed decrease of the pulsatility mode in the left-right view (Fig. 3.5a, top), the jet remains relatively uninterrupted. During the speed increase on the pulsatility mode in the left-right view (Fig. 3.5a, bottom), both the PIV and CFD show a greater disruption of the jet. The velocities are low in the near-wall region off-axis of the jet as well as in the LVOT due to the closure of the aortic valve (Fig. 3.5a). The velocities remain relatively high in the apex, promoting washout. In the posterior-anterior view, a large counterrotating vortex forms off-axis of the jet, creating a large stagnation region (Fig. 3.5b). The center of the vortex shifts over time, as seen in the two timepoints shown in Fig. 3.5b, changing the locations of elevated off-axis velocities near the anterior wall.

Figure 3.6 plots the velocity magnitude from PIV and CFD within a rectangular comparison domain in the posterior-anterior view at four different times during the

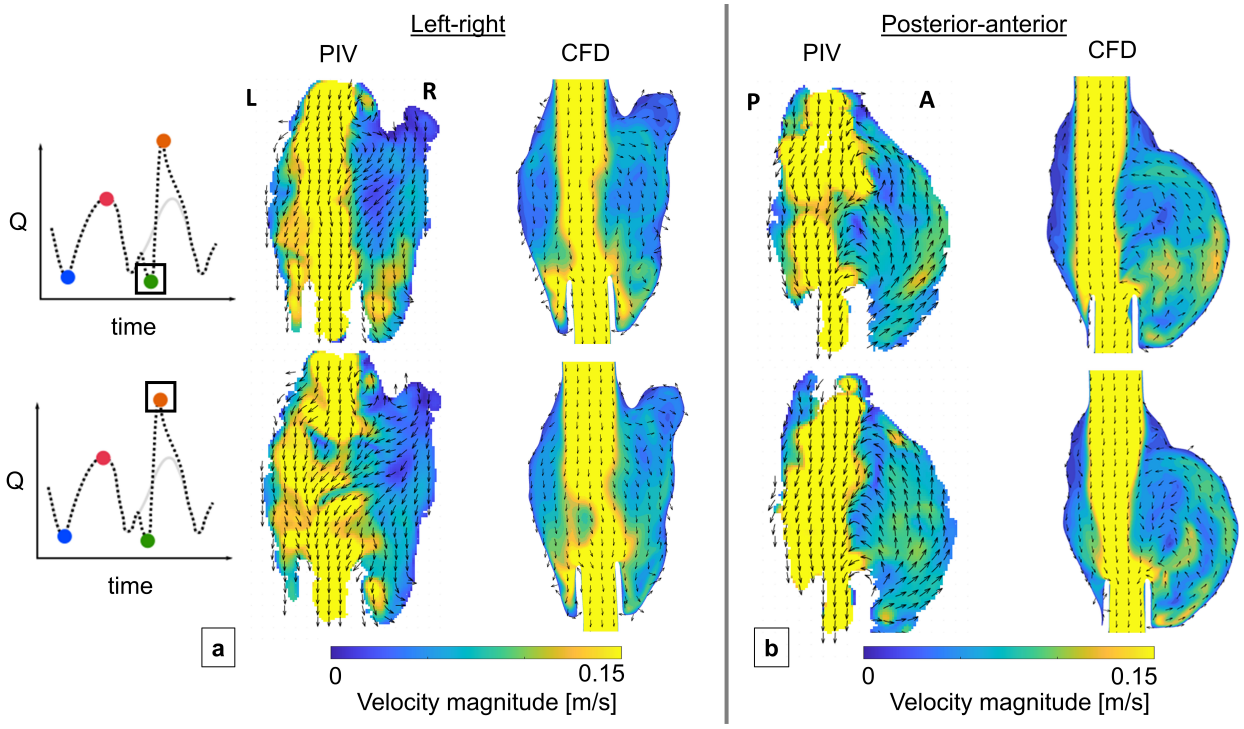

Figure 3.5: Velocity magnitude and in-plane direction for PIV experiments and CFD model at two different times for the speed modulation synchronized with systole. (a) Left-right view (b) Posterior-anterior view

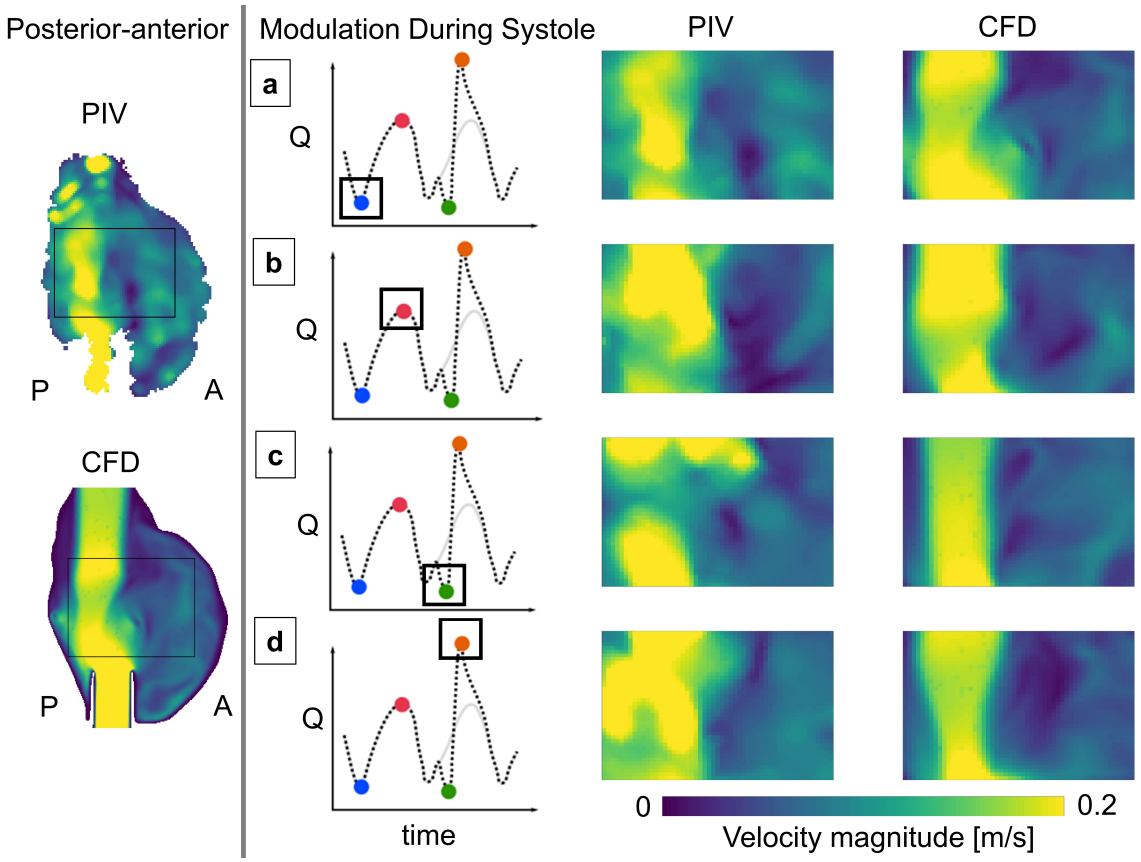

Figure 3.6: Comparison of velocity magnitude for speed modulation synchronized with systole within a rectangular subzone in the posterior-anterior view (a) at peak diastole (b) at peak systole (c) at low RPM and (d) at high RPM in the pulsatility mode

cardiac cycle for the pulsatility mode synchronized with systole. The velocity magnitudes are similar both within the jet and off-axis of the jet across the four timings. The velocities are highest in the jet, with a region of stagnation directly outside of the shear layer towards the anterior wall where the center of the counterrotating vortex appears (Fig. 3.5). At peak diastole (Fig. 3.6a), the PIV results show thinning of the jet, with the CFD showing weaker velocities centered between the upper and lower parts of the comparison domain. At peak systole (Fig. 3.6b), the velocities increase in the upper part of the comparison domain for both the PIV and CFD. At the low RPM segment of the pulsatility mode (Fig. 3.6c), the jet is significantly disrupted in the PIV results, which corresponds to a weakening in velocity magnitude and thinning of the jet in the CFD results. The disruption of the jet at the low RPM segment is propagated downstream, seen in Fig. 3.6d during the high RPM segment of the pulsatility mode.

Fig. 3.7 plots the velocity magnitude from PIV and CFD within the comparison domain in the left-right view at four different times during the cardiac cycle for the pulsatility mode synchronized with systole. A jet connects the mitral valve and the inflow cannula, with velocity magnitudes between the PIV and CFD agreeing both inside the jet and off-axis of the jet. The jet is significantly disrupted during peak diastole (Fig. 3.7a), almost completely disappearing in the PIV data and significantly weakening in the CFD. During peak systole (Fig. 3.7b), the jet noticeably strengthens in both the PIV and CFD. At the low RPM segment of the pulsatility mode (Fig. 3.7c), the jet begins to weaken, a trend that continues into the velocity profile at the the high RPM segment of the pulsatility mode (Fig. 3.7d).

In both planes (Figs. 3.6 and 3.7), the jet is significantly disrupted by changes in flow rate.

Bland-Altman plots compare the differences in velocity magnitudes between the CFD and PIV at each point within the comparison domain in Figure 3.8. In the posterior-anterior plane, the median differences are 0.003 m/s, 0.014 m/s, 0.017 m/s,

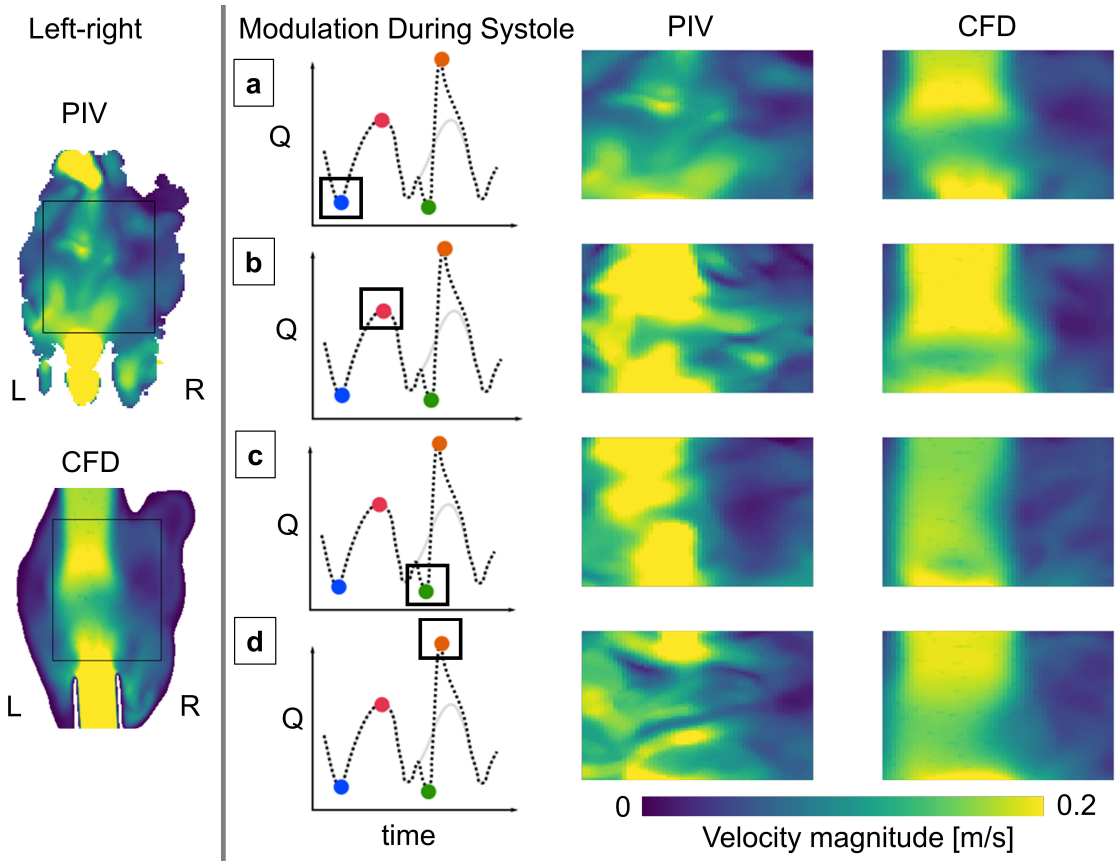

Figure 3.7: Comparison of velocity magnitude for speed modulation synchronized with systole within a rectangular subzone in the left-right view (a) at peak diastole (b) at peak systole (c) at low RPM and (d) at high RPM in the pulsatility mode

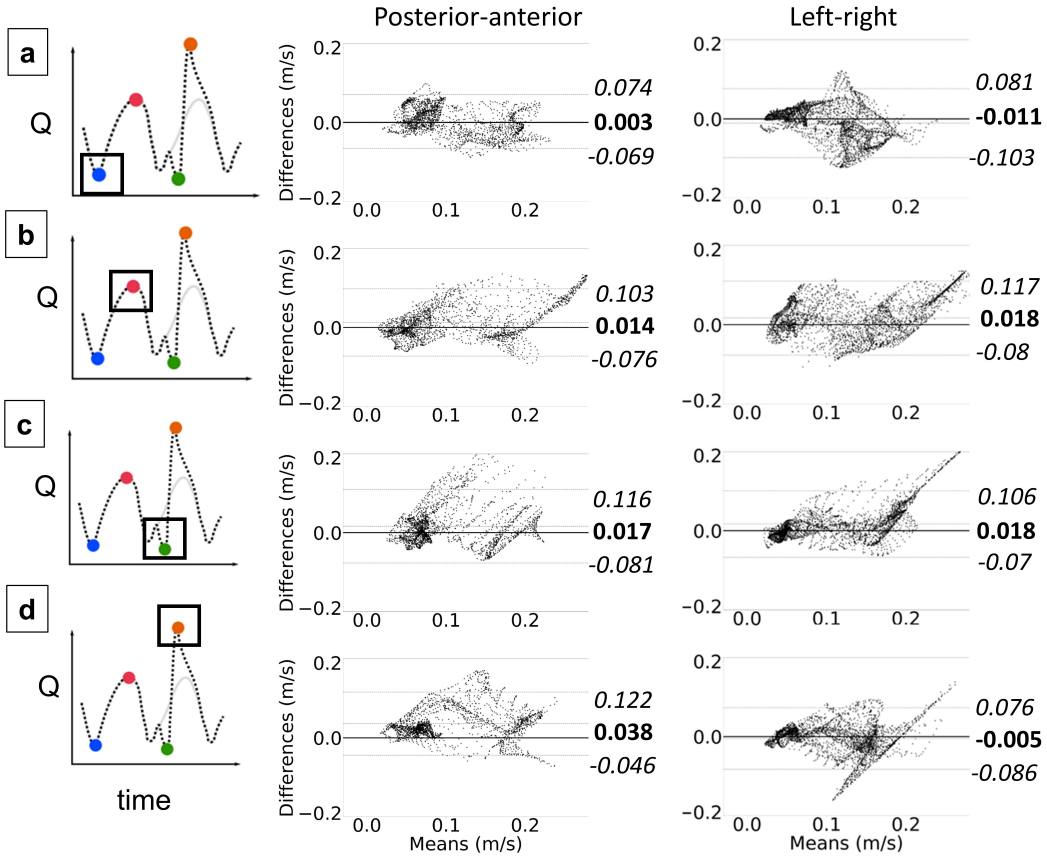

Figure 3.8: Bland-Altman plots of differences in CFD and PIV velocity magnitude for speed modulation synchronized with systole in the posterior-anterior and left-right views (a) at peak diastole (b) at peak systole (c) at low RPM and (d) at high RPM in the pulsatility mode with the median (labeled in bold face) and 95% confidence intervals (labeled with italics) identified with dashed lines

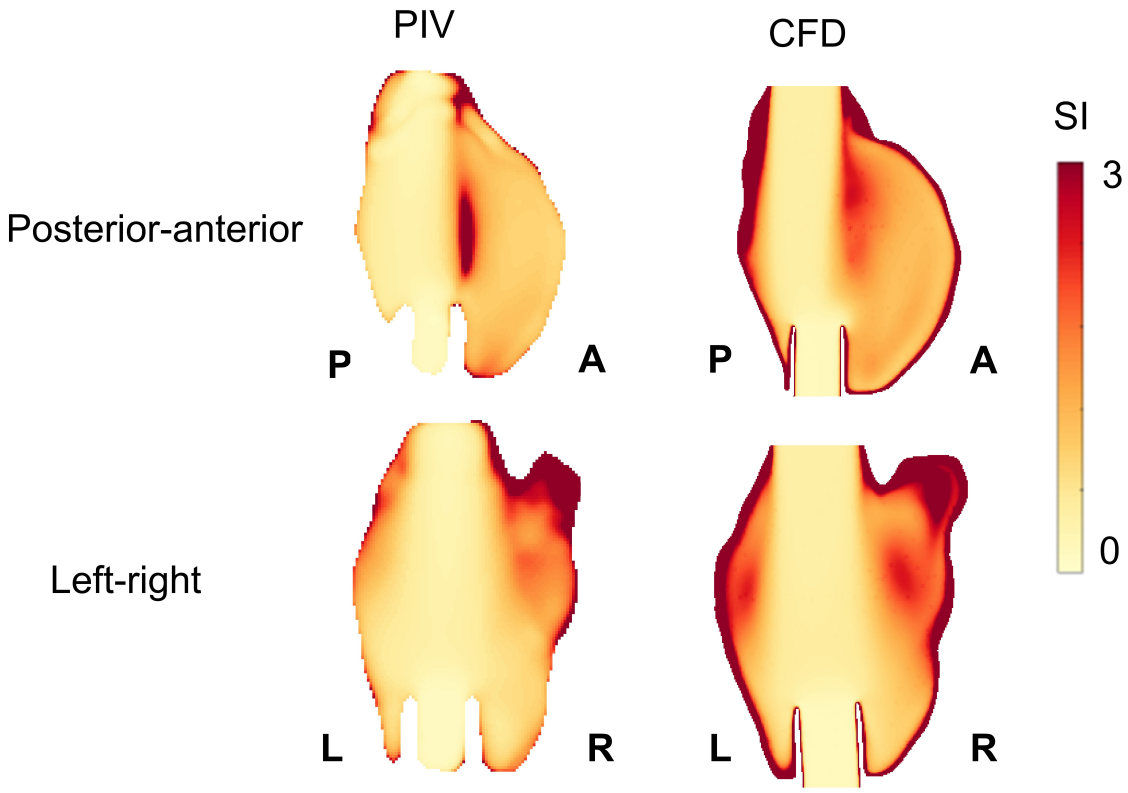

Figure 3.9: Stagnation index for the PIV experiment and CFD model in the posterior-anterior and left-right views for speed modulation synchronized with systole

and 0.038 m/s at peak diastole, peak systole, at low RPM, and at high RPM for the speed modulation, respectively. In the left-right plane, the median differences are -0.011 m/s, 0.018 m/s, 0.018 m/s, and -0.005 m/s at peak diastole, peak systole, at low RPM, and at high RPM for the speed modulation, respectively. These results show relatively low discrepancies between the CFD and PIV.

3.3.2 Stagnation Index

The SI for the PIV and CFD results in the posterior-anterior and left-right views are shown in Fig. 3.9. SI represents a time scale for washout in the Eulerian frame, with high values representing a high degree of stagnation.

The spatial variations and magnitudes of SI between the CFD and PIV results are similar for both views except very close to the walls where PIV cannot resolve the flow field accurately. The lowest values of SI occur within the jet and in the LV apex, indicating good washout. In the posterior-anterior view (Fig. 3.9, top), high values of SI occur off-axis of the jet near the posterior wall and in the separated region near the anterior wall. Within the separated region, there is a local SI maximum close to the shear layer of the jet, corresponding to the center of the recirculation vortex (Fig. 3.5b). In the left-right view (Fig. 3.9, bottom), the highest SI occurs off-axis of the jet below the mitral valve and in the LVOT due to the closed aortic valve, with SI magnitudes up to 4 seconds. The region washed out by the jet spreads to encompass the width of the LV as the flow reaches the inflow cannula, enhanced by disruption of the jet triggered by fluctuations in flow rate from the cardiac cycle and LVAD pulsatility. However, the SI remains high in the widest part of the LV.

3.3.3 Virtual Angiography

Figure 3.10a-e plot the results in the left-right view for the virtual angiography with contrast injected into the mitral valve, where darker regions represent areas of higher stagnation. Fig. 3.10f identifies three regions of interest – the near wall region, LVOT, and apex – where the concentration of the virtual contrast over time is plotted in Fig. 3.10g. Contrast is injected through the mitral valve for 8 seconds (Fig. 3.10a-b) and washed out over 16 seconds (Fig. 3.10c-e). During the first cardiac cycle of injection, a vortex ring is formed, and the contrast remains entrained in the jet vortex between the mitral valve and LVAD inflow cannula (Fig. 3.10a). After 8 seconds of contrast injection, the entire LV is filled with contrast (Fig. 3.10b). Early in the washout phase, the concentration of virtual contrast in the apex decreases (Fig. 3.10c). After 8 seconds of washout, the regions with the highest concentration of contrast lie near the left and right LV walls as well as in the LVOT (Fig. 3.10d), which were all identified as areas with high SI in Fig. 3.10. After 13 seconds of washout, contrast remains at a

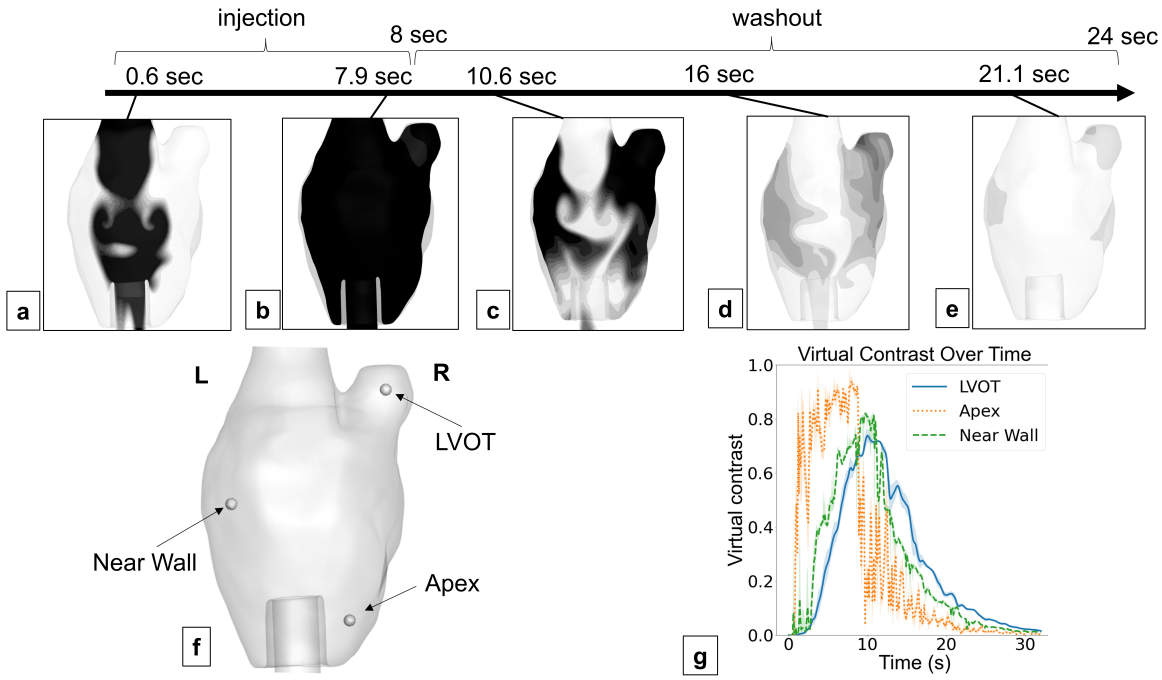

Figure 3.10: Virtual contrast injected in the CFD model for speed modulation synchronized at systole for 8 seconds followed by a period of washout. (a) 0.6 sec (b) 7.9 sec (c) 10.6 sec (d) 16 sec (e) 21.1 sec. (f) Spherical regions of interest (g) Virtual contrast over time in the LVOT, apex, and near wall region

measurable concentration only in the LVOT (Fig. 3.10e). These stagnation patterns can be quantified by examining the concentration of virtual contrast within regions of interest over time (Fig. 3.10g). The apical region fills most quickly with contrast, but the concentration quickly decreases during the washout phase. The near-wall region and LVOT see lower peak contrast concentrations than the apex; nonetheless, they have a persistent concentration of contrast that takes a longer time to washout than the apex. The areas identified as high stagnation – the LVOT and near-wall region – agree with the regions of low velocity measured in the PIV experiment [30].

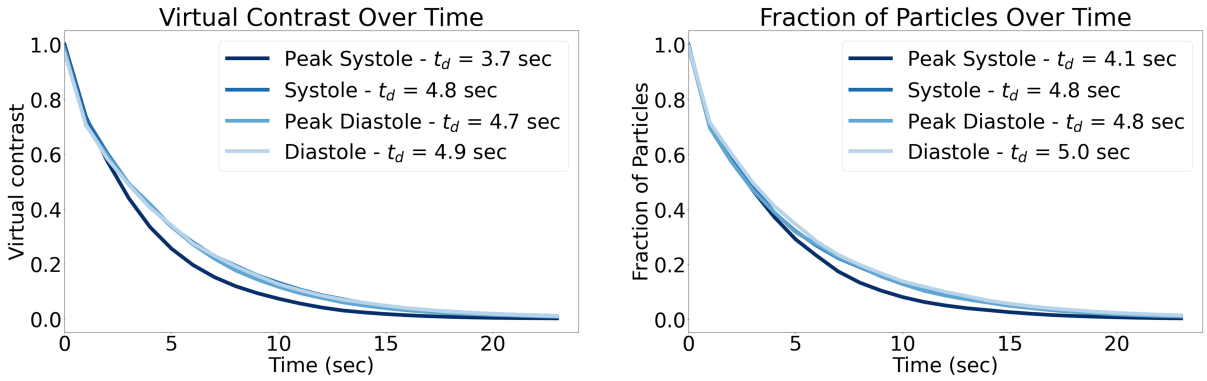

Figure 3.11: Virtual contrast integrated over the entire left ventricle versus time (left) and the fraction of particles remaining in the left ventricle versus time (right) for four temporal synchronizations with the corresponding exponential decay time t_d

3.3.4 Comparison of Temporal Synchronizations of the Pulsatility Mode

Fig. 3.11 plots the decay of virtual contrast concentration over time (left) and the fraction of particles remaining in the LV versus time (right) for the four timings of the pulsatility mode with respect to the cardiac cycle. For both the virtual contrast concentration and the fraction of particles remaining, the fastest decay occurred for the synchronization of the pulsatility mode with peak systole, representing the most favorable LV washout. When the pulsatility mode is synchronized with peak systole, the characteristic decay time is about 1 second shorter than for the other three timings – approximately 4 seconds versus approximately 5 seconds – demonstrating that there is a meaningful difference in washout characteristics depending on the temporal synchronization of the pulsatility mode.

3.3.5 Lagrangian Platelet Behavior

Figure 3.12a-b show three-dimensional particle trajectories colored by velocity magnitude of six distinct particles, three particles in each view, with residence times greater than 35 seconds. Long residence time particles stagnate in the LVOT (Fig. 3.12a)

and the counterrotating vortex formed by separated flow along the anterior wall (Fig. 3.12b). Fig. 3.12c-e show the distribution of SSH, RT, and SS_{ave}, respectively, experienced by all particles for temporal synchronization of the pulsatility mode with either peak systole or systole. Temporal synchronization with peak systole was shown in Fig. 3.12 to represent the quickest washout, with temporal synchronization during systole showing lesser degree of washout and behaving similarly to peak diastole and diastole. The distribution of SSH is comparable between the peak systole and systole timings (Fig. 3.12c), with the 95th, 98th, and 99.9th percentiles for peak systole and systole as 0.87 and 0.92 Pa·s, 1.16 and 1.21 Pa·s, and 2.22 and 2.11 Pa·s, respectively. Significantly fewer platelets spend high RT in the LV for the synchronization with peak systole than with systole (Fig. 3.12d), with the 95th, 98th, and 99.9th percentiles for peak systole and systole as 10.8 and 12.8 seconds, 14.4 and 17.6 seconds, and 25.1 and 31.2 seconds, respectively. These outliers represent the most thrombogenic platelets, which could potentially aggregate into an intraventricular thrombus. SS_{ave} experienced by the platelets is similar between both timings, with most particles experiencing less than 0.2 Pa and outliers experiencing up to 0.4 Pa (Fig. 3.12e).

3.4 Discussion

3.4.1 Comparison with Particle Image Velocimetry Experiments

The LV anatomy and mitral valve flow rate in this computational study were matched with those of a PIV experiment [30]. The CFD results show overall good agreement with the PIV results both in the direction and the magnitude of the velocities fields in the left-right and posterior-anterior views (Fig. 3.5). Key flow features were identified by both methodologies including a strong jet between the mitral valve and inflow cannula, a large counterrotating vortex due to separated flow near the anterior LV wall, relatively high velocities in the apex, and low velocities in the LVOT.

Bland-Altman comparisons demonstrated that the median differences in velocity

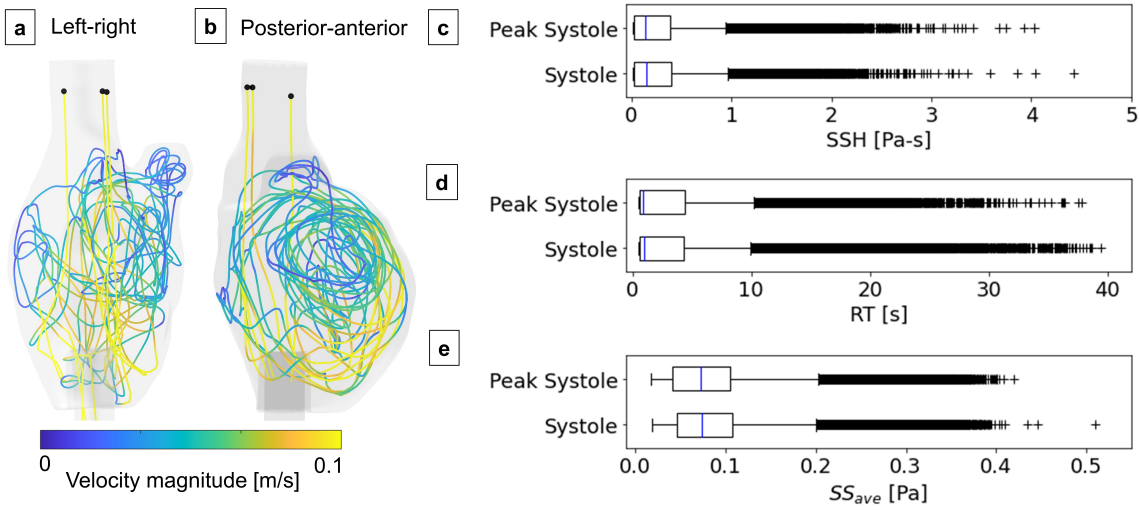

Figure 3.12: Representative particle trajectories for platelets that exceed 35 seconds of residence time in the (a) left-right view (b) posterior-anterior view. (c) Distributions of particle shear stress history, (d) residence time, and (e) time-averaged shear stress for speed modulation at peak systole and at systole

were 0.003 m/s, 0.014 m/s, 0.017 m/s, and 0.038 m/s in the posterior-anterior plane and -0.011, 0.018, 0.018, and -0.005 m/s in the left-right plane across four times during the cardiac cycle (Fig. 3.8), showing relatively low bias between the PIV and CFD results.

Some of the highest differences in velocities between the CFD and PIV occur at the boundary of the jet close to the mitral valve due to differences in the jet width. The differences in jet width near the mitral valve could be due to a difference in inlet boundary conditions. The experiment could have asymmetry in the incoming flow from the experimental flow loop while the computational model shows flow normal to the mitral valve boundary. The presence of inlet disturbances in the experiments can also influence jet behavior.

The exact location of the jet breakup may differ between the CFD and PIV, which can result in differences in spatial velocity distributions within the jet. This difference in location could be related to inherent challenges in synchronizing the

exact time points during the cardiac cycle at which the results are compared between the simulation and experiment. Jet breakup is more prominent in the experiment, possibly due to numerical diffusion in the simulation and differences in the amount of inlet disturbances entering the ventricle.

Deviations from the median value across the entirety of the comparison domain could be explained by measurement uncertainty, uncertainty in matching point-to-point values between the PIV and CFD results in the comparison domain, and experimental cycle-to-cycle variability.

Previous work with PIV experiments across three laboratories in a converging nozzle with a rapid expansion resulting in the formation of a jet indicated that interlaboratory variability in velocity profiles were about 10% for laminar and turbulent flows [63]. Interlaboratory variability could be up to 60% for transitional flow, which was reduced to about 15% when the degree of inlet disturbances was more closely matched between the experimental conditions. The LV flow in this study was transitional, so differences in inlet disturbances may be especially pertinent when comparing the PIV and CFD results. Given the inherent challenges of studying transitional flow and of matching experimental and computational results, median differences in velocities of about 20% of the mean velocity were considered to show acceptable agreement between the reported CFD and PIV results.

3.4.2 Hemodynamic Stagnation

Hemodynamic stagnation is a key risk factor for thrombus formation [94]. In this model, a high velocity jet forms between the mitral valve and inflow cannula with low velocities present off-axis of the jet. A high degree of stagnation is seen in the LVOT, represented by a high SI (Fig. 3.9), the presence of virtual contrast after multiple cycles of washout (Fig. 3.10), and long residence time platelet trajectories recirculating in that region (Fig. 3.12a). Hendabadi et al. employed Doppler echocardiography to study hemodynamic patterns in the LV of healthy patients, finding that

the SI in a typical healthy patient is about 1 second [64]. The SI in the LVOT of this anatomy without aortic valve opening was approximately 4 seconds, a large increase beyond physiologically normal levels. High degrees of stagnation were also present in the large counterrotating vortex along the anterior wall, demonstrated by high SI (Fig. 3.9) and the entrainment of platelets into the recirculating separation zone (Fig. 3.12b). Smaller off-axis vortices near the left and right LV walls showed high degrees of stagnation, represented by high SI (Fig. 3.9) and the persistent presence of virtual contrast (Fig. 3.10). The apex showed good washout both in terms of low SI (Fig. 3.9) and the fast decay of virtual contrast concentration in time (Fig. 3.11) due to the elevated velocities in this region (Fig. 3.5).

Previous in vitro [5, 125, 170], in vivo [139], and in silico [90] studies have documented similar flow features in the LV in the presence of an LVAD. Ortiz et al. found that a jet forms between the mitral valve and inflow cannula in addition to two vortices off-axis of the jet [125]. Rossini et al. similarly observed a persistent jet between the mitral valve and inflow cannula as well as high residence times off-axis of the jet due to flow separation and recirculation vortices [139]. Liao et al. simulated the ventricular flow in an LV with no aortic valve opening, finding higher residence times in the LVOT and near wall regions downstream of the mitral valve [90]. Aigner et al. compared velocity fields in an unsupported, partially supported, and fully supported LVAD patient; in the fully supported ventricle, no aortic valve opening occurred leading to lower velocities in the LVOT [5]. Wong et al. observed higher degrees of stasis in the LVOT without aortic valve opening and within the core of vortices formed off-axis of the jet [170], agreeing with high SI in the center of the vortices seen in Fig. 3.9.

Unlike two experimental studies that show stagnation in the apical pocket formed by the inflow cannula [31, 164], this study demonstrated good washout in this region. This behavior is likely impacted by patient anatomy, the transient flow rate profile through the LVAD, and the implantation characteristics of the inflow cannula.

These hemodynamic patterns could have important clinical implications for stroke. Thrombus formation has been clinically observed in the LVOT [27, 48, 52, 102, 152]. Fried et al. confirmed the presence of aortic root thrombosis in 4.8% of 436 patients with continuous-flow LVAD support [52], and Carey et al. found that 9.6% of 197 HeartMate 3 patients had aortic root thrombosis [27]. Dobarro et al. performed a clinical retrospective study of 147 HeartWare patients, finding that a closed aortic valve was an independent predictor of a combined thromboembolic event [45]. Lowering the LVAD speed can promote aortic valve opening [160], which could increase velocities in the LVOT [5] and thus decrease stasis.

3.4.3 Platelet Behavior

Lagrangian particle tracking provides insight into the hemodynamic microenvironment experienced by platelets. Most values of SI fell between 0.5 and 4 seconds, which agrees with the 25% to 75% quartiles of residence time experienced by the platelets in Lagrangian tracking (Fig. 3.12d). However, SI does not capture the behavior of outliers that would be most thrombogenic in the flow. For instance, the values of SI within the large counterrotating vortex near the anterior wall are about 1-2 seconds, whereas platelets trapped in this vortex can experience residence times over 35 seconds. Given prothrombin times of about 15 seconds [24], residence times above this threshold could have important implications for thrombus formation.

The maximum time-averaged stress experienced by the platelets is 0.4 Pa. Shankaran et al. studied platelet activation at constant shear rate in cone-plate viscometer, finding that the threshold for platelet activation is about 8 Pa [148]. This finding indicates that the typical stresses experienced by the platelets in the LV for most of their respective trajectories are relatively low compared to the activation threshold, suggesting that shear stress is not a primary risk factor for platelet activation in these intraventricular flows.

3.4.4 Optimum Temporal Synchronization

The influence of LVAD implantation on intraventricular hemodynamics is well-studied [5, 90, 125, 139, 170]. An active area of research is how LVAD speed modulation affects intraventricular hemodynamics [30, 76, 90, 103]. The present study is the first computational work to understand the role of synchronizing of the HeartMate 3 pulsatility mode with the cardiac cycle on intraventricular washout and platelet activation. An equivalent experiment addressed a similar research question [30] but was unable to identify a single optimal timing for which the synchronization of the pulsatility mode with the cardiac cycle most effectively promotes washout.

Four different timings of the HeartMate 3 pulsatility mode with respect to the cardiac cycle were studied. When the pulsatility mode is synchronized with peak systole, the virtual contrast concentration as well as the number of platelets in the LV decay most quickly over time (Fig. 3.11). This finding suggests that stagnation in the LV is reduced by synchronizing the pulsatility mode with peak systole. In the equivalent PIV experiment, Chassagne et al. found that the highest degree of stagnation in both the left-right and posterior-anterior planes occurred when the pulsatility mode was synchronized with diastole [30], which was also identified in this study as less favorable for intraventricular washout. However, the experiment could not significantly differentiate between the three remaining timings, demonstrating the benefit of virtual angiography and Lagrangian particle tracking as metrics for identifying a favorable temporal synchronization of the pulsatility mode with the cardiac cycle.

Previous studies have examined the relationship between sinusoidal speed modulation of an LVAD with respect to the cardiac cycle [90, 103]. Liao et al. found that copulsation of the speed modulation with the cardiac cycle decreased blood residence time and increased kinetic energy in the LV and apex [90]. McCormick et al. tracked Lagrangian particles in a computational model, reporting that copulsation promoted

the most intraventricular mixing of particles [103]. Khienwad et al. studied speed modulation from the Lavare cycle in the HVAD device [76], which ramps the speed down for 2 seconds and increases it for 1 second before returning to baseline. They found that the highest kinetic energy in the LV apex occurs when the speed decreases during diastole and increases during midsystole. These studies, in addition to the present study, suggest potential benefits for mixing and washout when synchronizing the pulsatility mode in time with the native cardiac cycle.

3.4.5 Limitations

The purpose of this study was to perform a comparison of temporal synchronization of the pulsatility mode at four timings with the cardiac cycle to identify the most favorable washout, with the same conditions being applied across the four timings.

This computational study was performed on a single patient anatomy. Ventricular hemodynamics can be altered based on changes in cannula orientation [39, 125] and insertion depth [38, 89], so future work should examine different cannula implantations. Smaller anatomical features like trabeculations and chordae tendinae were removed from the segmented geometry, which is a common simplification among published literature [38, 76, 90, 103].

The ventricular walls were modeled as rigid, which previous computational studies have also assumed [38, 76]. In patients with advanced heart failure, significantly reduced in vivo ventricular wall motion and reduced changes in ventricular volume are associated with weak native contractility. While changes in ventricular volume in the LV can be relatively small, changes in the intraventricular pressure, i.e., pre-load to the pump, result in different transient flow rate profiles [30] which were incorporated in this model via the boundary condition at the inflow cannula.

The mitral valve was excluded from this computational study, as is also absent in the equivalent experimental model, which has been assumed in previous studies [103, 176]. The aortic valve was modeled as closed, resulting in high stagnation in

the LVOT. Aortic valve closure is common in LVAD patients [72, 151], resulting from the LVAD fully unloading the ventricle [5].

The CFD results presented here agree closely with the PIV experiment on an equivalent LV experimental model implanted with a HeartMate 3 [30]. However, matching the exact location of the orthogonal planes in the PIV experiment with the computational results presents a challenge. Averaging CFD results across three planes centered around the cannula centerline both captures the velocity averaging that occurs with a finite thickness laser sheet and accounts for some degree of uncertainty between the laser sheet orientation compared with the computational plane orientation.

3.5 Conclusions

This study employed computational fluid dynamics simulations to study the degree of washout in the LV in the presence of the HeartMate 3 LVAD for four different temporal synchronizations of the pulsatility mode with the cardiac cycle. High residence time is a risk factor for thrombus formation, so areas of stagnation were identified from virtual angiography and SI. Lagrangian particle tracking simulated the hemodynamic environment experienced by platelets, i.e., RT and SSH.

The CFD velocity fields agree closely both in direction and magnitude with the PIV results at two orthogonal planes. A strong jet connects the mitral valve and the inflow cannula, fluctuating due to the pulsatile flow rate. Two vortices are formed off-axis of the jet in the left-right view, and a large counterrotating vortex appears in the posterior-anterior view. The SI was highest in the LVOT, in the separated regions near the wall, and within the center of the vortices formed off-axis of the jet. High residence platelets stagnated in the LVOT and the counterrotating vortex near the anterior wall, with the most thrombogenic platelets spending up to 40 seconds in the LV, which exceeds the maximum value of SI of about 4 seconds. Results from virtual angiography and Lagrangian particle tracking demonstrated that synchronizing the

pulsatility mode with peak systole can promote faster washout.

The results of this study suggest a potential benefit to optimizing the temporal synchronization of LVAD speed modulation with the cardiac cycle. The LVOT was identified as a significant region of stagnation, which could be mitigated by promoting aortic valve opening after LVAD implantation.

3.6 Future Work

The present study determined an optimal temporal synchronization between the pulsatility mode and cardiac cycle in one patient-specific ventricle with dilated cardiomyopathy. Future work should perform the same analysis on different patient-specific ventricles with different types of LV morphology and physiology. Cannula orientation and insertion depth can affect hemodynamics, so future studies would benefit from a parametric analysis of these factors in relation to intraventricular washout with the pulsatility mode. The rotational speed of the pump was fixed at 5200 RPM in this study, but there is a range of operating speeds for the HeartMate 3 that can change intraventricular flow rates. Future work should simulate flow under different pump operating conditions. The present study exclusively studied the HeartMate 3 device. This computational methodology can be extended to new devices as they enter the market, like the EvaHeart2.

Chapter 4

CONCLUSIONS OF THE DISSERTATION

Two cardiovascular pathologies – vasospasm in the CoW and intraventricular flow in the presence of an LVAD – have been explored using CFD simulations. Performing CFD analysis of cardiovascular flows provides a unique opportunity to extract metrics that are otherwise inaccessible using exclusively clinical data or experimental results. While qualitative clinical evaluations can help provide insights into a pathology, CFD provides a quantitative way to evaluate risk factors and to optimize conditions that can improve patient outcomes.

Changes in collateral flows within the CoW in the presence of vasospasm were studied across a cohort of 25 patients. Patient-specific simulations were generated by creating segmentations from CTA scans and boundary conditions from TCD measurements of blood velocity. Bayesian analysis accounted for parameter uncertainty and generated an optimized set of parameters that satisfied mass conservation. To improve the fidelity of the CFD models, the vessel diameters, velocities, and flow rates were benchmarked against literature values, and virtual angiograms were compared to clinical angiograms. Two metrics proposed to quantify vasospasm severity - percent changes in resistance and viscous dissipation – correlated closely with angiographic evaluations of severity. A complex interplay exists between the localization and overall severity of vasospasm, the anatomical variant, and changes in collateral flow rates. Future work can leverage this methodology to identify risk factors for the development of infarct.

Flow in the left ventricle in the presence of an LVAD was analyzed in order to identify risk factors for platelet activation using Eulerian metrics and Lagrangian

particle tracking. The effect of synchronizing the pulsatility mode of the HeartMate 3 device with the native cardiac cycle on intraventricular washout was investigated. Results from an equivalent PIV experiment were used to create realistic boundary conditions in the model and to validate the velocity fields and stagnation index, showing good agreement. High stagnation was observed in the LVOT, which could lead to thrombus formation. Synchronizing the pulsatility mode with peak systole during the cardiac cycle promoted intraventricular washout of virtual contrast and Lagrangian particles. Future work should expand this analysis to a cohort of patients implanted with a variety of LVADs.

These investigations addressed fundamental challenges in modeling cardiovascular fluid dynamics. Cardiovascular flows are characterized by a complex set of physics, from the non-Newtonian behavior of blood to the deformation in the left ventricle. Successful studies balance physical complexity with computational feasibility and identify appropriate assumptions that maximize the fidelity of the simulation without compromising on the essential physics. In the studies described in this thesis, simplifications have been made to find the right balance between these competing factors.

Patient-specific modeling is the gold standard for creating high fidelity models. Imaging techniques like CTA and MRI can provide 3D patient-specific geometries. Measurements of flow velocities from TCD can be leveraged to apply patient-specific boundary conditions. Medical data has inherent uncertainties that should be accounted for in the analysis; this thesis proposes a pathway for how Bayesian analysis can be used to optimize parameters given uncertainties from the medical data and performs a sensitivity analysis to variations in parameters. Benchmarking the results against clinical data is essential for validating the CFD simulations, such as comparing simulation parameters to literature values, using virtual angiography to compare to DSA, and leveraging PIV experiments to compare Eulerian metrics. Due to the variability in patient anatomies, performing a cohort study is necessary to identify

clinically relevant trends.

BIBLIOGRAPHY

[1] Cardiomyopathy - types. *https://www.nhlbi.nih.gov/health/cardiomyopathy/types*.

[2] Classes and stages of heart failure. *https://www.heart.org/en/health-topics/heart-failure/what-is-heart-failure/classes-of-heart-failure*.

[3] R. Aaslid, T. M. Markwalder, and H. Nornes. Noninvasive transcranial Doppler ultrasound recording of flow velocity in basal cerebral arteries. *Journal of Neurosurgery*, 57:769–774, 1982.

[4] Rune Aaslid. *Transcranial Doppler Examination Techniques*, volume 3, pages 39–59. Springer, Vienna, 1986.

[5] P. Aigner, M. Schweiger, K. Fraser, Y. Choi, F. Lemme, N. Cesarovic, U. Kertzscher, H. Schima, M. Hübler, and M. Granegger. Ventricular flow field visualization during mechanical circulatory support in the assisted isolated beating heart. *Annals of Biomedical Engineering*, 48:794–804, 2020.

[6] Fawaz Al-Mufti, Jens Witsch, Nathan Manning, Michael Crimmins, Krishna Amuluru, Sachin Agarwal, Soojin Park, Joshua Z. Willey, Hooman Kamel, E. Sander Connolly, Philip M. Meyers, and Jan Claassen. Severity of cerebral vasospasm associated with development of collaterals following aneurysmal subarachnoid hemorrhage. *Journal of NeuroInterventional Surgery*, 10:638–643, 7 2018.

[7] Jordi Alastruey, S. M. Moore, K. H. Parker, T. David, J. Peiró, and S. J. Sherwin. Reduced modelling of blood flow in the cerebral circulation: Coupling 1-D, 0-D and cerebral auto-regulation models. *International Journal for Numerical Methods in Fluids*, 56:1061–1067, 2008.

[8] Alberto Aliseda, Venkat Keshav Chivukula, Patrick McGah, Anthony R. Prisco, Jennifer A. Beckman, Guilherme J.M. Garcia, Nahush A. Mokadam, and Claudius Mahr. LVAD outflow graft angle and thrombosis risk. *ASAIO journal*, 63:14, 1 2017.

[9] Martin Sandve Alnæs, Jørgen Isaksen, Kent André Mardal, Bertil Romner, Michael K. Morgan, and Tor Ingebrigtsen. Computation of hemodynamics in the circle of Willis. *Stroke*, 38:2500–2505, 2007.

[10] Khalid Ambarki, Per Hallberg, Gauti Jóhannesson, Christina Lindén, Laleh Zarrinkoob, Anders Wåhlin, Richard Birgander, Jan Malm, and Anders Eklund. Blood flow of ophthalmic artery in healthy individuals determined by phase-contrast magnetic resonance imaging. *Investigative Ophthalmology and Visual Science*, 54:2738–2745, 4 2013.

[11] Sepideh Amin-Hanjani, Xinjian Du, Dilip K. Pandey, Keith R. Thulborn, and Fady T. Charbel. Effect of age and vascular anatomy on blood flow in major cerebral vessels. *Journal of Cerebral Blood Flow and Metabolism*, 35:312–318, 2015.

[12] Tomer Anor, Leopold Grinberg, Hyoungsu Baek, Joseph R. Madsen, Mahesh V. Jayaraman, and George E. Karniadakis. Modeling of blood flow in arterial trees. *Wiley Interdisciplinary Reviews: Systems Biology and Medicine*, 2:612–623, 9 2010.

[13] O. Y. Bang, J. L. Saver, J. R. Alger, S. Starkman, B. Ovbiagele, and D. S. Liebeskind. Determinants of the distribution and severity of hypoperfusion in patients with ischemic stroke. *Neurology*, 71:1804–1811, 11 2008.

[14] Yaron D. Barac, Adam Nevo, Jacob N. Schroder, Carmelo A. Milano, and Mani A. Daneshmand. LVAD outflow graft role in pump thrombosis. *ASAIO Journal*, 66:128–131, 2 2020.

[15] M.L. Barr and J.A. Kiernan. *The Human Nervous System: an Anatomical Viewpoint*. Lippincott Co., 1993.

[16] Stewart M. Benton, Christian Tesche, Carlo N. De Cecco, Taylor M. Duguay, U. Joseph Schoepf, and Richard R. Bayer. Noninvasive derivation of fractional flow reserve from coronary computed tomographic angiography: A review. *Journal of Thoracic Imaging*, 33:88–96, 2018.

[17] Philipp Berg, Daniel Stucht, G Abor Janiga, Oliver Beuing, Oliver Speck, and Dominique Thevenin. Cerebral blood flow in a healthy Circle of Willis and two intracranial aneurysms: Computational fluid dynamics versus four-dimensional phase-contrast magnetic resonance imaging. *Journal of Biomedical Engineering*, 136:041003–1–9, 2014.

[18] Philippe Bijlenga, Christian Ebeling, Max Jaegersberg, Paul Summers, Alister Rogers, Alan Waterworth, Jimison Iavindrasana, Juan Macho, Vitor Mendes Pereira, Peter Bukovics, Elio Vivas, Miriam C.J.M. Sturkenboom, Jessica Wright, Christoph M. Friedrich, Alejandro Frangi, James Byrne, Karl Schaller,

and Daniel Rufenacht. Risk of rupture of small anterior communicating artery aneurysms is similar to posterior circulation aneurysms. *Stroke*, 44:3018–3026, 11 2013.

[19] R. H.C. Bisschops, C. J.M. Klijn, L. J. Kappelle, A. C. van Huffelen, and J. van der Grond. Collateral flow and ischemic brain lesions in patients with unilateral carotid artery occlusion. *Neurology*, 60:1435–1441, 5 2003.

[20] Mirko Bonfanti, Stavroula Balabani, John P. Greenwood, Sapna Puppala, Shervanthi Homer-Vanniasinkam, and Vanessa Diáz-Zuccarini. Computational tools for clinical support: A multi-scale compliant model for haemodynamic simulations in an aortic dissection based on multi-modal imaging data. *Journal of the Royal Society Interface*, 14, 2017.

[21] Andrea Boraschi, Silvia Bozzi, Bente Thamsen, Marcus Granegger, Lena Wiegmann, Federico Pappalardo, Marvin J. Slepian, Vartan Kurtcuoglu, Alberto Redaelli, Diane De Zélicourt, and Filippo Consolo. Thrombotic risk of rotor speed modulation regimes of contemporary centrifugal continuous-flow left ventricular assist devices. *ASAIO Journal*, 67:737–745, 7 2021.

[22] Kevin Bourque, Christopher Cotter, Charles Dague, Daniel Harjes, Onur Dur, Julien Duhamel, Kaitlyn Spink, Kelly Walsh, and Edward Burke. Design rationale and preclinical evaluation of the HeartMate 3 left ventricular assist system for hemocompatibility. *ASAIO Journal*, 62:375–383, 8 2016.

[23] Luigi Bozzao, Luigi Maria Fantozzi, Stefano Bastianello, Alessandro Bozzao, and Cesare Fieschi. Early collateral blood supply and late parenchymal brain damage in patients with middle cerebral artery occlusion. *Stroke*, 20:735–740, 1989.

[24] Brian A. Bruckner, Daniel J. DiBardino, Qian Ning, Alfred Adeboygeun, Karim Mahmoud, Jamie Valdes, John Eze, Paul M. Allison, Denton A. Cooley, Igor D. Gregoric, and Oscar H. Frazier. High incidence of thromboembolic events in left ventricular assist device patients treated with recombinant activated factor VII. *The Journal of Heart and Lung Transplantation*, 28:785–790, 8 2009.

[25] Pieter C. Buijs, Monique J. Krabbe-Hartkamp, Chris J.G. Bakker, Eduard E. De Lange, Lino M.P. Ramos, Monique M.B. Breteler, and Willem P.T.M. Mali. Effect of age on cerebral blood flow: Measurement with ungated two-dimensional phase-contrast MR angiography in 250 adults. *Radiology*, 209:667–674, 12 1998.

[26] A. W. Cai, S. Islam, S. R. Hankins, W. Fischer, and H. J. Eisen. Mechanical circulatory support in the treatment of advanced heart failure. *American Journal of Transplantation*, 17:3020–3032, 12 2017.

[27] Matthew R. Carey, Dylan Marshall, Kevin Clerkin, Ronald Laracuente, Joseph Sanchez, Sneha S. Jain, Jayant K. Raikhelkar, Jay S. Leb, Yuji Kaku, Melana Yuzefpolskaya, Yoshifumi Naka, Paolo C. Colombo, Gabriel T. Sayer, Koji Takeda, Nir Uriel, Veli K. Topkara, and Justin A. Fried. Aortic root thrombosis in patients with HeartMate 3 left ventricular assist device support. *The Journal of Heart and Lung Transplantation*, 9 2023.

[28] J. R. Cebral, F. Mut, J. Weir, and C. Putman. Quantitative characterization of the hemodynamic environment in ruptured and unruptured brain aneurysms. *American Journal of Neuroradiology*, 32:145–151, 2011.

[29] Juan R Cebral, Marcelo A Castro, Orlando Soto, Rainald Löhner, and Noam Alperin. Blood-flow models of the circle of Willis from magnetic resonance data. *Journal of Engineering Mathematics*, 47:369–386, 2003.

[30] Fanette Chassagne, Jennifer A. Beckman, Song Li, Claudius Mahr, and Alberto Aliseda. In vitro investigation of the effect of the timing of left ventricular assist device speed modulation on intraventricular flow patterns. *ASAIO Journal*, 69:533–543, 6 2023.

[31] Fanette Chassagne, Marissa Miramontes, Venkat Keshav Chivukula, Song Li, Jennifer A. Beckman, Claudius Mahr, and Alberto Aliseda. In vitro investigation of the effect of left ventricular assist device speed and pulsatility mode on intraventricular hemodynamics. *Annals of Biomedical Engineering*, 49:1318–1332, 5 2021.

[32] W. W. Chen, H. Gao, X. Y. Luo, and N. A. Hill. Study of cardiovascular function using a coupled left ventricle and systemic circulation model. *Journal of Biomechanics*, 49:2445–2454, 2016.

[33] Z. Cheng, C. Juli, N. B. Wood, R. G.J. Gibbs, and X. Y. Xu. Predicting flow in aortic dissection: Comparison of computational model with PC-MRI velocity measurements. *Medical Engineering and Physics*, 36:1176–1184, 2014.

[34] J. M Chillon and G. L. Baumbach. *Primer on Cerebrovascular Diseases*. Academic Press, 4 1997.

[35] Prashant Chittiboina, Bharat Guthikonda, Christian Wollblad, and Steven A Conrad. A computational simulation of the effect of hemodilution on oxygen transport in middle cerebral artery vasospasm. *Journal of Cerebral Blood Flow and Metabolism*, 31:2209–2217, 2011.

[36] Wei Che Chiu, Yared Alemu, Allison J. Mclarty, Shmuel Einav, Marvin J. Slepian, and Danny Bluestein. Ventricular assist device implantation configurations impact overall mechanical circulatory support system thrombogenic potential. *ASAIO Journal*, 63:285, 6 2017.

[37] Wei Che Chiu, Gaurav Girdhar, Michalis Xenos, Yared Alemu, Shmuel Einav, Marvin Slepian, and Danny Bluestein. Thromboresistance comparison of the Heartmate II ventricular assist device with the device thrombogenicity emulation-optimized HeartAssist 5 VAD. *Journal of Biomechanical Engineering*, 136, 2 2014.

[38] Venkat Keshav Chivukula, Jennifer A. Beckman, Song Li, S. Carolina Masri, Wayne C. Levy, Shin Lin, Richard K. Cheng, Stephen D. Farris, Gregory Wood, Todd F. Dardas, James N. Kirkpatrick, Kevin Koomalsingh, Daniel Zimpfer, G. Burkhard MacKensen, Fanette Chassagne, Claudius Mahr, and Alberto Aliseda. Left ventricular assist device inflow cannula insertion depth influences thrombosis risk. *ASAIO Journal*, pages 766–773, 2020.

[39] Venkat Keshav Chivukula, Jennifer A. Beckman, Anthony R. Prisco, Todd Dardas, Shin Lin, Jason W. Smith, Nahush A. Mokadam, Alberto Aliseda, and Claudius Mahr. Left ventricular assist device inflow cannula angle and thrombosis risk. *Circulation: Heart Failure*, 11, 4 2018.

[40] Gregory A Christoforidis, Yousef Mohammad, Dimitris Kehagias, Bindu Avutu, and Andrew P Slivka. Angiographic assessment of pial collaterals as a prognostic indicator following intra-arterial thrombolysis for acute ischemic stroke. *American Journal of Neuroradiology*, 26:1789–1797, 2005.

[41] Rachel Clifford, Desiree Robson, Christoph Gross, Francesco Moscato, Heinrich Schima, Paul Jansz, Peter S. Macdonald, and Christopher S. Hayward. Beat-to-beat detection of aortic valve opening in HeartWare left ventricular assist device patients. *Artificial Organs*, 43:458–466, 10 2019.

[42] Paolo C. Colombo, Mandeep R. Mehra, Daniel J. Goldstein, Jerry D. Estep, Christopher Salerno, Ulrich P. Jorde, Jennifer A. Cowger, Joseph C. Cleveland, Nir Uriel, Gabriel Sayer, Eric R. Skipper, Francis X. Downey, Masahiro Ono, Robert Hooker, Anelechi C. Anyanwu, Michael M. Givertz, Claudius Mahr,

Ia Topuria, Sami I. Somo, Daniel L. Crandall, and Douglas A. Horstmanshof. Comprehensive analysis of stroke in the long-term cohort of the MOMENTUM 3 study. *Circulation*, 139:155–168, 1 2019.

[43] Earl W. Davie, Kazuo Fujikawa, and Walter Kisiel. The coagulation cascade: initiation, maintenance, and regulation. *Biochemistry*, 30:10363–10370, 10 1991.

[44] Andrew M. Demchuk, Ioannis Christou, Theodore H. Wein, Robert A. Felberg, Marc Malkoff, James C. Grotta, and Andrei V. Alexandrov. Specific transcranial Doppler flow findings related to the presence and site of arterial occlusion. *Stroke*, 31:140–146, 2000.

[45] David Dobarro, Marian Urban, Karen Booth, Neil Wrightson, Javier Castrodeza, Jerome Jungschleger, Nicola Robinson-Smith, Andrew Woods, Gareth Parry, Stephan Schueler, and Guy A Macgowan. Impact of aortic valve closure on adverse events and outcomes with the heartware ventricular assist device. *The Journal of Heart and Lung Transplantation*, 36:42–49, 2016.

[46] Dennis D. Doblar, Nataliya V. Plyushcheva, William Jordan, and Holt McDowell. Predicting the effect of carotid artery occlusion during carotid endarterectomy. *Stroke*, 29:2038–2042, 1998.

[47] EN El-Barhoun, SR Gledhill, and AG Pitman. Circle of Willis artery diameters on MR angiography: An Australian reference database. *Journal of Medical Imaging and Radiation Oncology*, 53:248–260, 6 2009.

[48] Jerry D. Estep, Raymond F. Stainback, Stephen H. Little, Guillermo Torre, and William A. Zoghbi. The role of echocardiography and other imaging modalities in patients with left ventricular assist devices, 10 2010.

[49] Peng Fang, Jianjun Du, Andrea Boraschi, Silvia Bozzi, Alberto Redaelli, Marianne Schmid Daners, Vartan Kurtcuoglu, Filippo Consolo, and Diane de Zélicourt. Insights into the low rate of in-pump thrombosis with the HeartMate 3: Does the artificial pulse improve washout? *Frontiers in Cardiovascular Medicine*, 9:775780, 3 2022.

[50] J. Max Findlay, Joshua Nisar, and Tim Darsaut. Cerebral vasospasm: A review. *Canadian Journal of Neurological Sciences*, 43:15–32, 2016.

[51] Matthew D. Ford, Noam Alperin, Sung Hoon Lee, David W. Holdworth, and David Steinman. Characterization of volumetric flow rate waveforms in the normal internal carotid and vertebral arteries. *Physiological Measurement*, 26:477–488, 2005.

[52] Justin Fried, Arthur R. Garan, Sophia Shames, Amirali Masoumi, Melana Yuzefpolskaya, Koji Takeda, Hiroo Takayama, Nir Uriel, Yoshifumi Naka, Paolo C. Colombo, and Veli K. Topkara. Aortic root thrombosis in patients supported with continuous-flow left ventricular assist devices. *The Journal of Heart and Lung Transplantation*, 37:1425–1432, 12 2018.

[53] Trygve O. Gabrielsen and Torgny Greitz. Normal size of the internal carotid, middle cerebral and anterior cerebral arteries. *Acta Radiologica*, 10:1–10, 8 1970.

[54] Franziska Gaidzik, Sahani Pathiraja, Sylvia Saalfeld, Daniel Stucht, Oliver Speck, Dominique Thévenin, and Gábor Janiga. Hemodynamic data assimilation in a subject-specific Circle of Willis geometry. *Clinical Neuroradiology*, 31:643–651, 9 2021.

[55] Efstratios Georgakarakos, Christos V. Ioannou, Yannis Papaharilaou, Theodoros Kostas, and Asterios N. Katsamouris. Computational evaluation of aortic aneurysm rupture risk: What have we learned so far? *Journal of Endovascular Therapy*, 18:214–225, 2011.

[56] Mojgan Ghodrati, Thananya Khienwad, Alexander Maurer, Francesco Moscato, Francesco Zonta, Heinrich Schima, and Philipp Aigner. Validation of numerically simulated ventricular flow patterns during left ventricular assist device support. *International Journal of Artificial Organs*, 44:30–38, 1 2021.

[57] G Girdhar, M Xenos, Y Alemu, W-C Chiu, and B E Lynch. Device thrombogenicity emulation: A novel method for optimizing mechanical circulatory support device thromboresistance. *PLoS ONE*, 7:32463, 2012.

[58] Carolyn H. Glass, Alexander Christakis, Gregory A. Fishbein, Jaclyn C. Watkins, Kyle C. Strickland, Richard N. Mitchell, and Robert F. Padera. Thrombus on the inflow cannula of the HeartWare HVAD: an update. *Cardiovascular Pathology*, 38:14–20, 1 2019.

[59] Francisco B. Gomes, Manuel Dujovny, Felix Umansky, S. Kim Berman, Fernando G. Diaz, James I. Ausman, Haresh G. Mirchandani, and William J. Ray. Microanatomy of the anterior cerebral artery. *Surgical Neurology*, 26:129–141, 8 1986.

[60] L. Grinberg, E. Cheever, T. Anor, J. R. Madsen, and G. E. Karniadakis. Modeling blood flow circulation in intracranial arterial networks: A comparative 3D/1D simulation study. *Annals of Biomedical Engineering*, 39:297–309, 2011.

[61] Leopold Grinberg and George Em Karniadakis. Outflow boundary conditions for arterial networks with multiple outlets. *Annals of Biomedical Engineering*, 36:1496–1514, 2008.

[62] P. Grolimund and R. W. Seiler. Age dependence of the flow velocity in the basal cerebral arteries-a transcranial Doppler ultrasound study. *Ultrasound in Medicine and Biology*, 14:191–198, 1988.

[63] Prasanna Hariharan, Matthew Giarra, Varun Reddy, Steven W. Day, Keefe B. Manning, Steven Deutsch, Sandy F.C. Stewart, Matthew R. Myers, Michael R. Berman, Greg W. Burgreen, Eric G. Paterson, and Richard A. Malinauskas. Multilaboratory particle image velocimetry analysis of the FDA benchmark nozzle model to support validation of computational fluid dynamics simulations. *Journal of Biomechanical Engineering*, 133, 2 2011.

[64] Sahar Hendabadi, Javier Bermejo, Yolanda Benito, Raquel Yotti, Francisco Fernández-Avilés, Juan C. Del Álamo, and Shawn C. Shadden. Topology of blood transport in the human left ventricle by novel processing of Doppler echocardiography. *Annals of Biomedical Engineering*, 41:2603–2616, 12 2013.

[65] Jeroen Hendrikse, Monique J. Hartkamp, Berend Hillen, Willem P.T.M. Mali, and Jeroen Van Der Grond. Collateral ability of the Circle of Willis in patients with unilateral internal carotid artery occlusion. *Stroke*, 32:2768–2773, 12 2001.

[66] Jeroen Hendrikse, A. Fleur Van Raamt, Yolanda Van Der Graaf, Willem P.T.M. Mali, and Jeroen Van Der Grond. Distribution of cerebral blood flow in the circle of Willis. *Radiology*, 235:184–189, 4 2005.

[67] M. Hennerici, W. Rautenberg, G. Sitzer, and A. Schwartz. Transcranial Doppler ultrasound for the assessment of intracranial arterial flow velocity—Part 1. examination technique and normal values. *Surgical Neurology*, 27:439–448, 5 1987.

[68] Madelene Holmgren, Petter Holmlund, Karen Helene Støverud, Laleh Zarrinkoob, Anders Wåhlin, Jan Malm, and Anders Eklund. Prediction of cerebral perfusion pressure during carotid surgery – a computational fluid dynamics approach. *Clinical Biomechanics*, 100:1–8, 2022.

[69] Madelene Holmgren, Karen Helene Støverud, Laleh Zarrinkoob, Anders Wåhlin, Jan Malm, and Anders Eklund. Middle cerebral artery pressure laterality in patients with symptomatic ICA stenosis. *PLoS ONE*, 16:1–15, 2021.

[70] T.C. Hung, R.M. Hochmith, J.H. Jorst, and S.P. Sutera. Shear induced aggregation and lysis of platelets. *Transactions - American Society for Artificial Internal Organs*, 22:285–290, 1976.

[71] Asad Ikram, Muhammad Ali Javaid, Santiago Ortega-Gutierrez, Magdy Selim, Sarah Kelangi, Syed Muhammad, Hamza Anwar, Michel T Torbey, and Afshin A Divani. Delayed cerebral ischemia after subarachnoid hemorrhage. *Journal of Stroke and Cerebrovascular Diseases*, 30:1–9, 2021.

[72] Ranjit John, Katie Mantz, Peter Eckman, Alan Rose, and Karen May-Newman. Aortic valve pathophysiology during left ventricular assist device support. *The Journal of Heart and Lung Transplantation*, 29:1321–1329, 12 2010.

[73] Liang Der Jou, Deok Hee Lee, and Michel E. Mawad. Cross-flow at the anterior communicating artery and its implication in cerebral aneurysm formation. *Journal of Biomechanics*, 43:2189–2195, 2010.

[74] Sylvia Kamath. Observations on the length and diameter of vessels forming the circle of willis. *Journal of Anatomy*, 133:419–423, 1981.

[75] Ayse Karatas, Gokmen Coban, Celal Cinar, Ismail Oran, and Aysun Uz. Assessment of the circle of Willis with cranial tomography angiography. *Medical Science Monitor*, 21:2647–2652, 2015.

[76] Thananya Khienwad, Alexander Maurer, Mojgan Ghodrati, Thomas Schlöglhofer, Francesco Moscato, Martin Stoiber, Heinrich Schima, and Philipp Aigner. Effect of timings of the Lavare cycle on the ventricular washout in an in vitro flow visualization setup. *ASAIO Journal*, 67:517–528, 5 2021.

[77] Changsung Sean Kim. Numerical simulation of auto-regulation and collateral circulation in the human brain. *Journal of Mechanical Science and Technology*, 21:525–535, 2007.

[78] Changsung Sean Kim, Cetin Kiris, Dochan Kwak, and Tim David. Numerical simulation of local blood flow in the carotid and cerebral arteries under altered gravity. *Journal of Biomechanical Engineering*, 128:194–202, 4 2006.

[79] Jane J. Kim, Nancy J. Fischbein, Ying Lu, Daniel Pham, and William P. Dillon. Regional angiographic grading system for collateral flow: Correlation with cerebral infarction in patients with middle cerebral artery occlusion. *Stroke*, 35:1340–1344, 6 2004.

[80] J.T. King. Epidemiology of aneurysmal subarachnoid hemorrhage. *Neuroimaging Clinics of North America*, 7:659–668, 11 1997.

[81] Christof Klotzsch, Octavian Popescu, and Peter Berlit. Assessment of the posterior communicating artery by transcranial color-coded duplex sonography. *Stroke*, 27:486–489, 1996.

[82] Robert L. Kormos, Jennifer Cowger, Francis Pagani, Jeffrey J. Teuteberg, Daniel J. Goldstein, Jeffrey P. Jacobs, Robert S. Higgins, Lynne W. Stevenson, Josef Stehlik, Pavan Atluri, Kathleen L. Grady, and James K. Kirklin. The Society of Thoracic Surgeons Intermacs database annual report: Evolving indications, outcomes, and scientific partnerships. *Journal of Heart and Lung Transplantation*, 38:114–126, 2019.

[83] Monique J. Krabbe-Hartkamp, Jeroen Van Der Grond, Frank Erik De Leeuw, Jan Cees De Groot, Ale Algra, Berend Hillen, Monique M.B. Breteler, and Willem P.T.M. Mali. Circle of Willis: Morphologic variation on three-dimensional time-of- flight MR angiograms. *Radiology*, 207:103–112, 4 1998.

[84] Jaroslaw Krejza, W. Rudzinski, M. A. Pawlak, M. Tomaszewski, R. Ichord, J. Kwiatkowski, D. Gor, and E. R. Melhem. Angle-corrected imaging transcranial Doppler sonography versus imaging and nonimaging transcranial Doppler sonography in children with sickle cell disease. *American Journal of Neuroradiology*, 28:1613–1618, 2007.

[85] Jeffrey A. Larose, Daniel Tamez, Michael Ashenuga, and Carlos Reyes. Design concepts and principle of operation of the HeartWare ventricular assist system. *ASAIO Journal*, 56:285–289, 7 2010.

[86] Sang Wook Lee and David A. Steinman. On the relative importance of rheology for image-based CFD models of the carotid bifurcation. *Journal of Biomechanical Engineering*, 129:273–278, 2007.

[87] Avi Levine and Alan Gass. Third-generation LVADs: Has anything changed? *Cardiology in Review*, 27:293–301, 11 2019.

[88] Song Li, Jennifer A. Beckman, Richard Cheng, Chinwe Ibeh, Claire J. Creutzfeldt, Jason Bjelkengren, Joni Herrington, April Stempien-Otero, Shin Lin, Wayne C. Levy, Daniel Fishbein, Kevin J. Koomalsingh, Daniel Zimpfer, Mark S. Slaughter, Alberto Aliseda, David Tirschwell, and Claudius Mahr. Comparison of neurologic event rates among HeartMate II, HeartMate 3, and HVAD. *ASAIO Journal*, 66:620–624, 2 2020.

[89] Sam Liao, Michael Neidlin, Zhiyong Li, Benjamin Simpson, and Shaun D Gregory. Ventricular flow dynamics with varying LVAD inflow cannula lengths: In-silico evaluation in a multiscale model. *Journal of Biomechanics*, 72:106–115, 2018.

[90] Sam Liao, Eric L. Wu, Michael Neidlin, Zhiyong Li, Benjamin Simpson, and Shaun D. Gregory. The influence of rotary blood pump speed modulation on the risk of intraventricular thrombosis. *Artificial Organs*, 42:943–953, 10 2018.

[91] Karl-Fredrik Lindegaard, Søren Jacob Bakke, Peter Grolimund, Rune Aaslid, Peter Huber, and Helge Nornes. Assessment of intracranial hemodynamics in carotid artery disease by transcranial Doppler ultrasound. *Journal of Neurosurgery*, 63:890–898, 12 1985.

[92] Jia Liu, Zhengzheng Yan, Yuehua Pu, Wen-Shin Shiu, Jianhuang Wu, Rongliang Chen, Xinyi Leng, Haiqiang Qin, Xin Liu, Baixue Jia, Ligang Song, Yilong Wang, Zhongrong Miao, Yongjun Wang, Liping Liu, and Xiao-Chuan Cai. Functional assessment of cerebral artery stenosis: A pilot study based on computational fluid dynamics. *Journal of Cerebral Blood Flow and Metabolism*, 37:2567–2576, 2017.

[93] Quan Long, Luca Luppi, Carola S. König, Vittorio Rinaldo, and Saroj K. Das. Study of the collateral capacity of the circle of Willis of patients with severe carotid artery stenosis by 3D computational modeling. *Journal of Biomechanics*, 41:2735–2742, 8 2008.

[94] Gordon D.O. Lowe. Virchow's triad revisited: Abnormal flow. *Pathophysiology of Haemostasis and Thrombosis*, 33:455–457, 12 2003.

[95] Mohamed Abdelaziz Maaly and Ahmed Abdelazim Ismail. Three dimensional magnetic resonance angiography of the circle of Willis: Anatomical variations in general Egyptian population. *Egyptian Journal of Radiology and Nuclear Medicine*, 42:405–412, 12 2011.

[96] Matthew E. MacDonald and Richard Frayne. Phase contrast MR imaging measurements of blood flow in healthy human cerebral vessel segments. *Physiological Measurement*, 36:1517–1527, 2015.

[97] Grainne Malone, Gerges Abdelsayed, Fianait Bligh, Fatma Al Qattan, Saifullah Syed, Prateepan Varatharajullu, Augustin Msellati, Daniela Mwipatayi, Maimoona Azhar, Andrew Malone, Saulat H. Fatimi, Claire Conway, and Aamir

Hameed. Advancements in left ventricular assist devices to prevent pump thrombosis and blood coagulopathy. *Journal of Anatomy*, 242:29–49, 1 2023.

[98] Donna Mancini and Paolo C. Colombo. Left ventricular assist devices: A rapidly evolving alternative to transplant, 6 2015.

[99] Gil Marom, Wei Che Chiu, Jessica R. Crosby, Katrina J. DeCook, Saurabh Prabhakar, Marc Horner, Marvin J. Slepian, and Danny Bluestein. Numerical model of full-cardiac cycle hemodynamics in a total artificial heart and the effect of its size on platelet activation. *Journal of Cardiovascular Translational Research*, 7:788–796, 11 2014.

[100] Ian Marshall, Shunzhi Zhao, Panorea Papathanasopoulou, Peter Hoskins, and X. Yun Xu. MRI and CFD studies of pulsatile flow in healthy and stenosed carotid bifurcation models. *Journal of Biomechanics*, 37:679–687, 2004.

[101] P. J. Martin, D. H. Evans, and A. R. Naylor. Transcranial color-coded sonography of the basal cerebral circulation; reference data from 115 volunteers. *Stroke*, 25:390–396, 1994.

[102] Karen May-Newman, York Kin Wong, Robert Adamson, Peter Hoagland, Vi Vu, and Walter Dembitsky. Thromboembolism is linked to intraventricular flow stasis in a patient supported with a left ventricle assist device. *ASAIO Journal*, 59:452–455, 7 2013.

[103] Matthew Mccormick, David Nordsletten, Pablo Lamata, and Nicolas P Smith. Computational analysis of the importance of flow synchrony for cardiac ventricular assist devices. *Computers in Biology and Medicine*, 49:83–94, 2014.

[104] Patrick M. McGah, Daniel F. Leotta, Kirk W. Beach, James J. Riley, and Alberto Aliseda. A longitudinal study of remodeling in a revised peripheral artery bypass graft using 3D ultrasound imaging and computational hemodynamics. *Journal of Biomechanical Engineering*, 133:1–10, 2011.

[105] Patrick M. McGah, Michael R. Levitt, Michael C. Barbour, Ryan P. Morton, John D. Nerva, Pierre D. Mourad, Basavaraj V. Ghodke, Danial K. Hallam, Laligam N. Sekhar, Louis J. Kim, and Alberto Aliseda. Accuracy of computational cerebral aneurysm hemodynamics using patient-specific endovascular measurements. *Annals of Biomedical Engineering*, 42:503–514, 3 2014.

[106] Mandeep R. Mehra, Daniel J. Goldstein, Nir Uriel, Joseph C. Cleveland, Melana Yuzefpolskaya, Christopher Salerno, Mary N. Walsh, Carmelo A. Milano, Chetan B. Patel, Gregory A. Ewald, Akinobu Itoh, David Dean, Arun Krishnamoorthy, William G. Cotts, Antone J. Tatooles, Ulrich P. Jorde, Brian A. Bruckner, Jerry D. Estep, Valluvan Jeevanandam, Gabriel Sayer, Douglas Horstmanshof, James W. Long, Sanjeev Gulati, Eric R. Skipper, John B. O'Connell, Gerald Heatley, Poornima Sood, and Yoshifumi Naka. Two-year outcomes with a magnetically levitated cardiac pump in heart failure. *New England Journal of Medicine*, 378:1386–1395, 4 2018.

[107] Adamantios Michalinos, Sofia Zogana, Evangelos Kotsiomitis, Antonios Mazarakis, and Theodore Troupis. Anatomy of the ophthalmic artery: A review concerning its modern surgical and clinical applications. *Anatomy Research International*, 2015:1–8, 2015.

[108] Rajat Mittal, Jung Hee Seo, Vijay Vedula, Young J. Choi, Hang Liu, H. Howie Huang, Saurabh Jain, Laurent Younes, Theodore Abraham, and Richard T. George. Computational modeling of cardiac hemodynamics: Current status and future outlook. *Journal of Computational Physics*, 305:1065–1082, 2016.

[109] A. M. Moerman, S. Korteland, K. Dilba, K. van Gaalen, D. H.J. Poot, A. van Der Lugt, H. J.M. Verhagen, J. J. Wentzel, A. F.W. van Der Steen, F. J.H. Gijsen, and K. Van der Heiden. The correlation between wall shear stress and plaque composition in advanced human carotid atherosclerosis. *Frontiers in Bioengineering and Biotechnology*, 9, 2022.

[110] Parham Moftakhar, Daniel L. Cooke, Heather J. Fullerton, Nerissa U. Ko, Matthew R. Amans, Jared A. Narvid, Christopher F. Dowd, Randall T. Higashida, Van V. Halbach, and Steven W. Hetts. Extent of collateralization predicting symptomatic cerebral vasospasm among pediatric patients: correlations among angiography, transcranial Doppler ultrasonography, and clinical findings. *Journal of Neurosurgery Pediatrics*, 15:282–290, 3 2015.

[111] S. Moore, T. David, J. G. Chase, J. Arnold, and J. Fink. 3D models of blood flow in the cerebral vasculature. *Journal of Biomechanics*, 39:1454–1463, 1 2006.

[112] Paul D. Morris, Desmond Ryan, Allison C. Morton, Richard Lycett, Patricia V. Lawford, D. Rodney Hose, and Julian P. Gunn. Virtual fractional flow reserve from coronary angiography: Modeling the significance of coronary lesions. *JACC: Cardiovascular Interventions*, 6:149–157, 2013.

[113] Keri R. Moyle, Luca Antiga, and David A. Steinman. Inlet conditions for image-based CFD models of the carotid bifurcation: Is it reasonable to assume fully developed flow? *Journal of Biomechanical Engineering*, 128:371–379, 2006.

[114] Marcus Mueller, Christoph Hoermandinger, Gregor Richter, Johanna Mulzer, Dmytro Tsyganenko, Thomas Krabatsch, Christoph Starck, Julia Stein, Felix Schoenrath, Volkmar Falk, and Evgenij Potapov. Retrospective 1-year outcome follow-up in 200 patients supported with HeartMate 3 and HeartWare left ventricular assist devices in a single centre. *European Journal of Cardio-Thoracic Surgery*, 57:1160–1165, 2020.

[115] Debanjan Mukherjee, Neel D. Jani, Jared Narvid, and Shawn C. Shadden. The role of Circle of Willis anatomy variations in cardio-embolic stroke: A patient-specific simulation based study. *Annals of Biomedical Engineering*, 46:1128–1145, 8 2018.

[116] M Muller, M Hermes, H Bruckmann, and K Schimrigk. Transcranial Doppler ultrasound in the evaluation of collateral blood flow in patients with internal carotid artery occlusion: correlation with cerebral angiography. *American Journal of Neuroradiology*, 16, 1995.

[117] H. R. Müller, Chr Brunhölzl, E. W. Radü, and M. Buser. Sex and side differences of cerebral arterial caliber. *Neuroradiology*, 33:212–216, 5 1991.

[118] Martin Müller and Klaus Schimrigk. A comparative assessment of cerebral haemodynamics in the basilar artery and carotid territory by transcranial Doppler sonography in normal subjects. *Ultrasound in Medicine and Biology*, 20:677–687, 1 1994.

[119] Shiro Nagasawa, Masahiro Kawanishi, Yuichi Tada, Shinji Kawabata, and Tomio Ohta. Intra-operative measurement of cortical arterial flow volumes in posterior circulation using Doppler sonography. *Neurological Research*, 22:194–196, 2000.

[120] Nikhil Narang, Gabriel Sayer, and Nir Uriel. *Hemodynamic Optimization of the LVAD Patient*, pages 849–857. Wiley, 9 2023.

[121] Edgar Nathal, F. Lóopez-González, and C. Rios. Angiographic scale for evaluation of cerebral vasospasm. *Acta Neurochirurgica, Supplementum*, pages 225–228, 2008.

[122] Ivan Netuka and Mandeep R. Mehra. Ischemic stroke and subsequent thrombosis within a HeartMate 3 left ventricular assist system: A cautionary tale. *Journal of Heart and Lung Transplantation*, 37:170–172, 1 2018.

[123] Ann B. Nguyen, Nir Uriel, and Sirtaz Adatya. New challenges in the treatment of patients with left ventricular support: LVAD thrombosis. *Current Heart Failure Reports*, 13:302–309, 12 2016.

[124] Mette S. Olufsen. A one-dimensional fluid dynamic model of the systemic arteries. *Studies in Health Technology and Informatics*, 71:79–98, 2000.

[125] Sean Ortiz, Vi Vu, Ricardo Montes, and Karen May-Newman. Left ventricular flow dynamics with the HeartMate3 left ventricular assist device: Effect of inflow cannula position and speed modulation. *ASAIO Journal*, 67:1301–1311, 12 2021.

[126] Fadar Otite, Susanne Mink, Can Ozan Tan, Ajit Puri, Amir A. Zamani, Aujan Mehregan, Sherry Chou, Susannah Orzell, Sushmita Purkayastha, Rose Du, and Farzaneh A. Sorond. Impaired cerebral autoregulation is associated with vasospasm and delayed cerebral ischemia in subarachnoid hemorrhage. *Stroke*, 45:677–682, 2014.

[127] Romana Perinajová, Pim van Ooij, and Saša Kenjereš. On the identification of hypoxic regions in subject-specific cerebral vasculature by combined CFD/MRI. *Royal Society Open Science*, 10, 1 2023.

[128] Anthony R. Prisco, Alberto Aliseda, Jennifer A. Beckman, Nahush A. Mokadam, Claudius Mahr, and Guilherme J.M. Garcia. Impact of LVAD implantation site on ventricular blood stagnation. *ASAIO Journal*, 63:392–400, 2017.

[129] E W Radu and G H Du Boulay. Paradoxical dilatation of the large cerebral arteries in hypocapnia in man. *Journal of Neurosurgery*, 36:634–639, 1972.

[130] J.M. Ramstack, L. Zuckerman, and L.F. Mockros. Shear-induced activation of platelets. *Journal of Biomechanics*, 12:113–125, 1 1979.

[131] V L Rayz, L Boussel, L Ge, J R Leach, A J Martin, M T Lawton, C Mcculloch, and D Saloner. Flow residence time and regions of intraluminal thrombus deposition in intracranial aneurysms. *Annals of Biomedical Engineering*, 38:3058–3069, 2010.

[132] M. Reinhard, T. Müller, B. Guschlbauer, J. Timmer, and Andreas Hetzel. Dynamic cerebral autoregulation and collateral flow patterns in patients with severe carotid stenosis or occlusion. *Ultrasound in Medicine and Biology*, 29:1105–1113, 8 2003.

[133] Yuan Ren, Qiang Chen, and Zhi-Yong Li. A 3D numerical study of the collateral capacity of the circle of Willis with anatomical variation in the posterior circulation. *BioMedical Engineering Online*, 14:1–12, 2015.

[134] Cindy Richter, Robert Werdehausen, Jennifer Jentzsch, Dirk Lindner, Thilo Gerhards, Torsten Hantel, Khaled Gaber, Stefan Schob, Dorothee Saur, Ulf Quäschling, Karl Titus Hoffmann, Svitlana Ziganshyna, and Dirk Halama. The supratrochlear artery sign—a new piece in the puzzle of cerebral vasospasm. *Diagnostics*, 12:2185, 9 2022.

[135] B Albert Ring and Margaret M Waddington. Intraluminal diameters of the intracranial arteries. *Vascular Surgery*, 1:137–151, 1967.

[136] E. B. Ringelstein, B. Kahlscheuer, E. Niggemeyer, and S. M. Otis. Transcranial Doppler sonography: Anatomical landmarks and normal velocity values. *Ultrasound in Medicine and Biology*, 16:745–761, 1 1990.

[137] Erich Bernd Ringelstein, Cornelius Weiller, Matthias Weckesser, and Susanne Weckesser. Cerebral vasomotor reactivity is significantly reduced in low-flow as compared to thromboembolic infarctions: The key role of the circle of Willis. *Journal of the Neurological Sciences*, 121:103–109, 1 1994.

[138] Joe Sam Robinson, M. Sami Walid, Sinjae Hyun, Robert O'Connell, Chris Menard, and Brandi Bohleber. Computational modeling of HHH therapy and impact of blood pressure and hematocrit. *World Neurosurgery*, 74:294–296, 2010.

[139] Lorenzo Rossini, Oscar O. Braun, Michela Brambatti, Yolanda Benito, Adam Mizeracki, Marissa Miramontes, Cathleen Nguyen, Pablo Martinez-Legazpi, Shone Almeida, Megan Kraushaar, Vi Vu, Karen May-Newman, Javier Bermejo, Eric D. Adler, Andrew M. Kahn, and Juan C. Del Alamo. Intraventricular flow patterns in patients treated with left ventricular assist devices. *ASAIO Journal*, 67:74–83, 1 2021.

[140] D. R. Rutgers, C. J. M. Klijn, L. J. Kappelle, A. C. van Huffelen, and J. van der Grond. A longitudinal study of collateral flow patterns in the Circle of Willis and

the ophthalmic artery in patients with a symptomatic internal carotid artery occlusion. *Stroke*, 31:1913–1920, 2000.

[141] Jaiyoung Ryu, Nerissa Ko, Xiao Hu, and Shawn C Shadden. Numerical investigation of vasospasm detection by extracranial blood velocity ratios. *Cerebrovascular Diseases*, 43:214–222, 2017.

[142] Sethuraman Sankaran and Alison L. Marsden. A stochastic collocation method for uncertainty quantification and propagation in cardiovascular simulations. *Journal of Biomechanical Engineering*, 133, 2011.

[143] Jonas Schollenberger, Nicholas H. Osborne, Luis Hernandez-Garcia, and C. Alberto Figueroa. A combined computational fluid dynamics and arterial spin labeling MRI modeling strategy to quantify patient-specific cerebral hemodynamics in cerebrovascular occlusive disease. *Frontiers in Bioengineering and Biotechnology*, 9, 8 2021.

[144] Don F. Schomer, Michael P. Marks, Gary K. Steinberg, Iain M. Johnstone, Derek B. Boothroyd, Michael R. Ross, Norbert J. Pelc, and Dieter R. Enzmann. The anatomy of the posterior communicating artery as a risk factor for ischemic cerebral infarction. *The New England Journal of Medicine*, 330:1565–1570, 1 1994.

[145] M. Schoning, R. Buchholz, and J. Walter. Comparative study of transcranial color duplex sonography and transcranial doppler sonography in adults. *Journal of Neurosurgery*, 78:776–784, 1993.

[146] B. D. Seeley and D. F. Young. Effect of geometry on pressure losses across models of arterial stenoses. *Journal of Biomechanics*, 9:439–448, 1976.

[147] Santhosh Seshadhri, Gábor Janiga, Oliver Beuing, Martin Skalej, and Dominique Thévenin. Impact of stents and flow diverters on hemodynamics in idealized aneurysm models. *Journal of Biomechanical Engineering*, 133, 2011.

[148] Harish Shankaran, Paschalis Alexandridis, and Sriram Neelamegham. Aspects of hydrodynamic shear regulating shear-induced platelet activation and self-association of von Willebrand factor in suspension. *Blood*, 101:2637–2645, 4 2003.

[149] Sunil A. Sheth, Nerses Sanossian, Qing Hao, Sidney Starkman, Latisha K. Ali, Doojin Kim, Nestor R. Gonzalez, Satoshi Tateshima, Reza Jahan, Gary R.

Duckwiler, Jeffrey L. Saver, Fernando Vinuela, and David S. Liebeskind. Collateral flow as causative of good outcomes in endovascular stroke therapy. *Journal of NeuroInterventional Surgery*, 0:1–6, 1 2014.

[150] Masato Shiba, Fujimaro Ishida, and Kazuhiro Furukawa. Computational fluid dynamics for predicting delayed cerebral ischemia after subarachnoid hemorrhage. *Journal of Neurological Disorders and Stroke*, 5:1–4, 2017.

[151] Jaqueline G. Da Rocha E Silva, Anna L. Meyer, Sandra Eifert, Jens Garbade, Friedrich W. Mohr, and Martin Strueber. Influence of aortic valve opening in patients with aortic insufficiency after left ventricular assist device implantation. *European Journal of Cardio-Thoracic Surgery*, 49:784–787, 2016.

[152] Mark S Slaughter, Francis D Pagani, Joseph G Rogers, Leslie W Miller, Benjamin Sun, Stuart D Russell, Randall C Starling, Leway Chen, Andrew J Boyle, Suzanne Chillcott, Robert M Adamson, Margaret S Blood, Margarita T Camacho, Katherine A Idrissi, Michael Petty, Michael Sobieski, Susan Wright, Timothy J Myers, and David J Farrar. Clinical management of continuous-flow left ventricular assist devices in advanced heart failure. *The Journal of Heart and Lung Transplantation*, 29:S1–S39, 2010.

[153] Mark S. Slaughter, Joseph G. Rogers, Carmelo A. Milano, Stuart D. Russell, John V. Conte, David Feldman, Benjamin Sun, Antone J. Tatooles, Reynolds M. Delgado, James W. Long, Thomas C. Wozniak, Waqas Ghumman, David J. Farrar, and O. Howard Frazier. Advanced heart failure treated with continuous-flow left ventricular assist device. *New England Journal of Medicine*, 361:2241–2251, 12 2009.

[154] Erik N. Sorensen, Lynn M. Dees, David J. Kaczorowski, and Erika D. Feller. The Heartware Lavare cycle: A cautionary tale. *ASAIO Journal*, 66:E114–E116, 9 2020.

[155] Marco Antonio Stefani, Felipe Luis Schneider, Antonio Carlos, Huf Marrone, and Antonio Generoso Severino. Influence of the gender on cerebral vascular diameters observed during the magnetic resonance angiographic examination of willis circle. *Brazilian Archives of Biology and Technology*, 56:45–52, 2013.

[156] Ilija D Sutalo, Anh V Bui, Shakil Ahmed, Kurt Liffman, and Richard Manasseh. Modeling of flow through the Circle of Willis and cerebral vasculature to assess the effects of changes in the peripheral small cerebral vasculature on the inflows. *Engineering Applications of Computational Fluid Mechanics*, 8:609–622, 2014.

[157] Lawrence Talbot and Stanley A Berger. Fluid-mechanical aspects of the human circulation. *American Scientist*, 62:671–682, 1974.

[158] H Tanaka, N Fujita, T Enoki, K Matsumoto, Y Watanabe, K Murase, and H Nakamura. Relationship between variations in the Circle of Willis and flow rates in internal carotid and basilar arteries determined by means of magnetic resonance imaging with semiautomated lumen segmentation: Reference data from 125 healthy volunteers. *American Journal of Neuroradiology*, 27:1770–1775, 2006.

[159] Charles A Taylor and Mary T Draney. Experimental and computational methods in cardiovascular fluid mechanics. *Annual Review Fluid Mechanics*, 36:197–231, 2003.

[160] Sam Tolpen, Jochem Janmaat, Claudine Reider, Faouzi Kallel, David Farrar, and Karen May-Newman. Programmed speed reduction enables aortic valve opening and increased pulsatility in the LVAD-assisted heart. *ASAIO Journal*, 61:540–547, 10 2015.

[161] Abdullah Topcu, Ayca Ozkul, Ali Yilmaz, Ho Jun Yi, Dong Seong Shin, and BumTae Kim. The impact of collateral status on cerebral vasospasm and delayed cerebral ischemia in subarachnoid hemorrhage. *Journal of Cerebrovascular and Endovascular Neurosurgery*, 5 2023.

[162] Connie W. Tsao, Aaron W. Aday, Zaid I. Almarzooq, Alvaro Alonso, Andrea Z. Beaton, Marcio S. Bittencourt, Amelia K. Boehme, Alfred E. Buxton, April P. Carson, Yvonne Commodore-Mensah, Mitchell S.V. Elkind, Kelly R. Evenson, Chete Eze-Nliam, Jane F. Ferguson, Giuliano Generoso, Jennifer E. Ho, Rizwan Kalani, Sadiya S. Khan, Brett M. Kissela, Kristen L. Knutson, Deborah A. Levine, Tené T. Lewis, Junxiu Liu, Matthew Shane Loop, Jun Ma, Michael E. Mussolino, Sankar D. Navaneethan, Amanda Marma Perak, Remy Poudel, Mary Rezk-Hanna, Gregory A. Roth, Emily B. Schroeder, Svati H. Shah, Evan L. Thacker, Lisa B. VanWagner, Salim S. Virani, Jenifer H. Voecks, Nae-Yuh Wang, Kristine Yaffe, and Seth S. Martin. Heart disease and stroke statistics—2022 update: A report from the American Heart Association. *Circulation*, 145, 2 2022.

[163] K. J. van Everdinge, G. H. Visser, C. J. M. Klijn, L. J. Kappelle, and J. van Der Grond. Role of collateral flow on cerebral hemodynamics in patients with unilateral internal carotid artery occlusion. *Annals of Neurology*, 44:167–176, 8 1998.

[164] Francesco Viola, Elizabeth Jermyn, James Warnock, Giorgio Querzoli, and Roberto Verzicco. Left ventricular hemodynamics with an implanted assist device: An in vitro fluid dynamics study. *Annals of Biomedical Engineering*, 47:1799–1814, 8 2019.

[165] Nicolaas Westerhof, Frederik Bosman, Cornelis J. De Vries, and Abraham Noordergraaf. Analog studies of the human systemic arterial tree. *Journal of Biomechanics*, 2:121–143, 1969.

[166] Lena Wiegmann, Bente Thamsen, Diane de Zélicourt, Marcus Granegger, Stefan Boës, Marianne Schmid Daners, Mirko Meboldt, and Vartan Kurtcuoglu. Fluid dynamics in the HeartMate 3: Influence of the artificial pulse feature and residual cardiac pulsation. *Artificial Organs*, 43:363–376, 2019.

[167] Eelco F.M. Wijdicks, David F. Kallmes, Edward M. Manno, Jimmy R. Fulgham, and David G. Piepgras. Subarachnoid hemorrhage: Neurointensive care and aneurysm repair. *Mayo Clinic Proceedings*, 80:550–559, 4 2005.

[168] J.L. Wilterdink, E. Feldmann, K.L. Furie, M. Bragoni, and J.G. Benavides. Transcranial Doppler ultrasound battery reliably identifies severe internal carotid artery stenosis. *Stroke*, 28:133–136, 1997.

[169] J. R. Womersley. Method for the calculation of velocity, rate of flow and viscous drag in arteries when the pressure gradient is known. *The Journal of Physiology*, 127:553–563, 1955.

[170] K. Wong, G. Samaroo, I. Ling, W. Dembitsky, R. Adamson, J. C. del Álamo, and K. May-Newman. Intraventricular flow patterns and stasis in the LVAD-assisted heart. *Journal of Biomechanics*, 47:1485–1494, 4 2014.

[171] Anders Wåhlin, Khalid Ambarki, Jón Hauksson, Richard Birgander, Jan Malm, and Anders Eklund. Phase contrast MRI quantification of pulsatile volumes of brain arteries, veins, and cerebrospinal fluids compartments: Repeatability and physiological interactions. *Journal of Magnetic Resonance Imaging*, 35, 5 2012.

[172] Clyde W. Yancy, Mariell Jessup, Biykem Bozkurt, Javed Butler, Donald E. Casey, Mark H. Drazner, Gregg C. Fonarow, Stephen A. Geraci, Tamara Horwich, James L. Januzzi, Maryl R. Johnson, Edward K. Kasper, Wayne C. Levy, Frederick A. Masoudi, Patrick E. McBride, John J.V. McMurray, Judith E. Mitchell, Pamela N. Peterson, Barbara Riegel, Flora Sam, Lynne W. Stevenson, W. H.Wilson Tang, Emily J. Tsai, and Bruce L. Wilkoff. 2013 ACCF/AHA guideline for the management of heart failure: Executive summary: A report of

the American College of Cardiology Foundation/American Heart Association task force on practice guidelines. *Circulation*, 128:1810–1852, 10 2013.

[173] Hossein Zareie, Debbie A. Quain, Mark Parsons, Kerry J. Inder, Patrick McElduff, Ferdinand Miteff, Neil J. Spratt, and Christopher Levi. The influence of anterior cerebral artery flow diversion measured by transcranial Doppler on acute infarct volume and clinical outcome in anterior circulation stroke:. *International Journal of Stroke*, 8:228–234, 5 2012.

[174] Laleh Zarrinkoob, Khalid Ambarki, Anders Wåhlin, Richard Birgander, Anders Eklund, and Jan Malm. Blood flow distribution in cerebral arteries. *Journal of Cerebral Blood Flow and Metabolism*, 35:648–654, 2015.

[175] Meide Zhao, S. Amin-Hanjani, S. Ruland, A. P. Curcio, L. Ostergren, and F. T. Charbel. Regional cerebral blood flow using quantitative MR angiography. *American Journal of Neuroradiology*, 28:1470–1473, 9 2007.

[176] Daniel Zimpfer, Martin Strueber, Philipp Aigner, Jan D. Schmitto, Arnt E. Fiane, Robert Larbalestier, Steven Tsui, Paul Jansz, Andre Simon, Stephan Schueler, Francesco Moscato, and Heinrich Schima. Evaluation of the HeartWare ventricular assist device Lavare cycle in a particle image velocimetry model and in clinical practice. *European Journal of Cardio-thoracic Surgery*, 50:839–848, 11 2016.

[177] Dorothea I. Zuleger, Dimos Poulikakos, Anton Valavanis, and Spyros S. Kollias. Combining magnetic resonance measurements with numerical simulations - extracting blood flow physiology information relevant to the investigation of intracranial aneurysms in the circle of Willis. *International Journal of Heat and Fluid Flow*, 31:1032–1039, 2010.